Biophysical mechanisms responsible for ultrasound neuromodulation in bilayer lipid membranes

Enabling the research that uncovers the mysterious interactions between ultrasound and neurons.

Niels Burghoorn

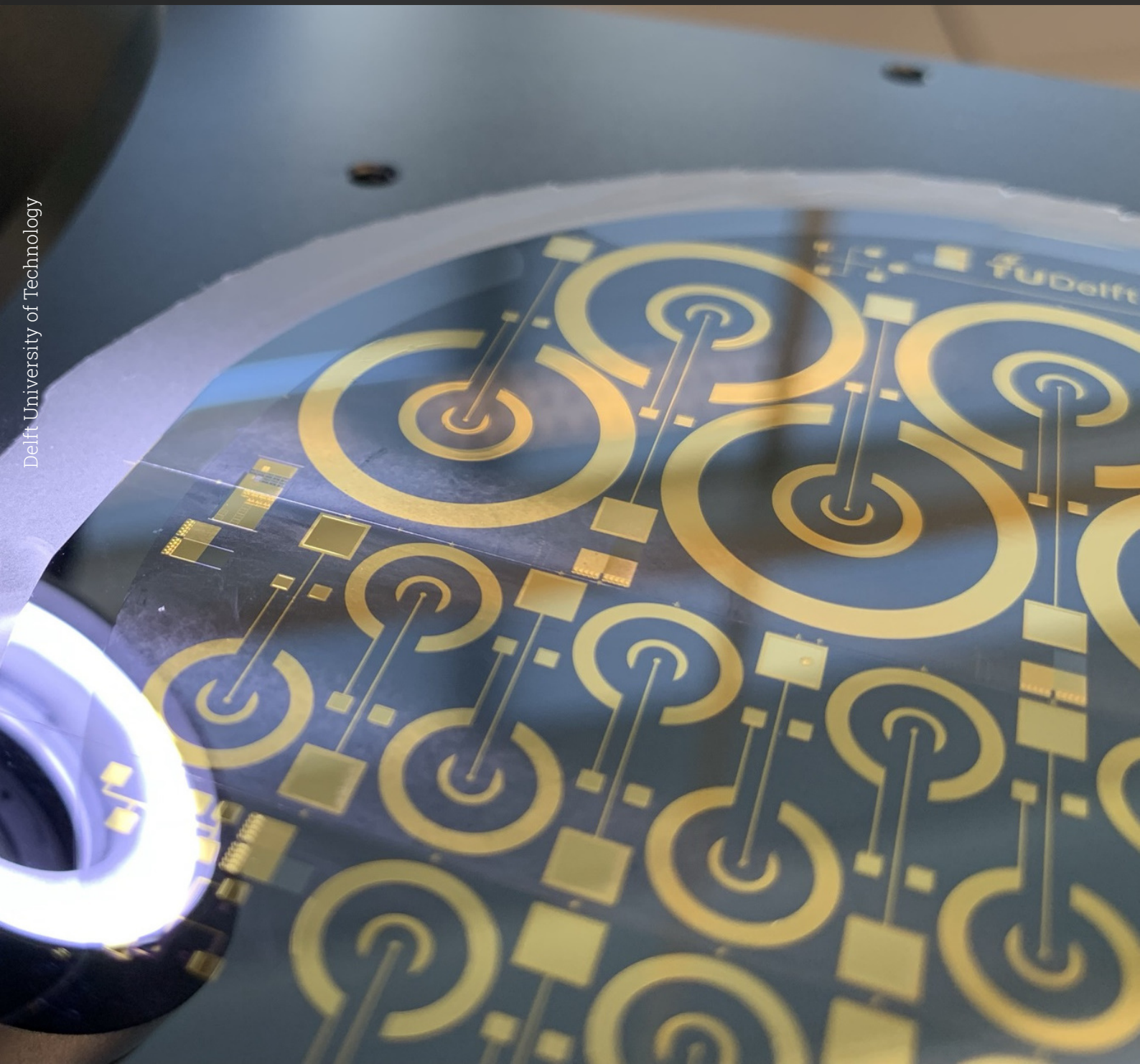

Delft University of Technology

Biophysical mechanisms responsible for ultrasound neuromodulation in bilayer lipid membranes

Enabling the research that uncovers the mysterious interactions between ultrasound and neurons.

by

Niels Burghoorn

Student Number 4659252

Student Number:	4659252
Thesis committee:	Dr. A. Accardo
	Dr. T.M.L. Costa (chair)
	Dr. S. Vollebregt
	Ir. G. Wardhana
Project Duration:	December 2021 - October 2022

TU Delft

Preface

Firstly, I would like to thank my beloved EVA... which is, of course, the software package developed during my internship (Experiment Visual Acoustics). Although she is not a finished product, she has helped me a great deal to generate nice plots.

Of course, I would like to thank my family. My facetime sessions with my "little" brother Gijs have been incredibly fun and equally ridiculous and nerdy. I hope we will live closer together in the future to come. My parents have always triggered my ambitions or steered me towards them, enabling me to reach higher. They have also provided me with their genetic restlessness that I am now grateful for during my work. My older sister Marieke has inspired me to meticulously choose my words and her facetime calls were always a welcome distraction.

I would like to thank all the MSc and PhD students in the Bioelectronics department, they have made my time here quite enjoyable. It is to be a time I will always cherish in the years to come, mainly because of these people.

I want to thank Andreas Hartel for helping me and sharing an afternoon with me in a room where some guys were laser-cutting something without an air filter creating a terrible smell. He taught me a lot about the biological part of my thesis sits in the daunting shadow of his work.

Also, I would like to show my appreciation to Prof Frans Widdershoven, who made time for me on several occasions to talk about the mysteries of electrochemistry and electroplating. His unbounded knowledge of physical phenomena always seemed to have a story connected to them, which was of just as much value as the information itself.

Then I would like to thank Dr Tiago Costa for the great environment and atmosphere he created. I always enjoyed the group meetings he facilitated and outside of our ping pong matches, I always felt like my work was respected. I recently found the slack channel where he publishes "literary wisdom" with a series of welcome philosophical distractions. He is a professor with a vision, but still gave me a lot of room for doing exploratory research fueled by pure curiosity. I would love to someday be like he is today.

Gandhi Wardhana was my day-to-day supervisor from whom I have not only learned everything in the clean room, but also a lot about setting priorities. His intuïtion and dead-on observations have been crucial when I was stuck. Although it should not be taken out of context, a strong quote by Gandhi was made: "Doubt is death". This helped me to do things instead of endlessly thinking about what would be the best next step. It also continued progress in face of the uncertainty of experimental research, which was solved by gathering evidence until the doubt actually died. He always has some good advice at a moment's notice. His inexhaustible interest in everything and easily exhaustible stamina also make him a great research partner and friend, but a lousy ping-pong opponent ;).

Lastly, my girlfriend, who is incidentally also named Eva. She is the reason I went home at the end of the day. Therefore she is also the reason this work is not more elaborate, but honestly, without her, it wouldn't have existed at all. She has been the one that has helped me when I was without inspiration and showed me how to organise my schedule, my work, and my life. She does not know how good of a person she is, and maybe it is for the best because she would be overwhelmed. I do not thank her enough, for her willingness to put up with my nerdy crap. Still, I do too with hers, and I love all of it.

Now I would like to stop this sentimental train of thought and get back to the work at hand: emotionless science. Ultrasound, cleanrooms, cellular membranes, and damned electrochemistry. Let us see why a single person would ever need to combine these things. I hope I can convey my interest in these topics to you. If not, just have look at all the figures, they are awesome.

Abstract

Medical technology has seen great progress over the last centuries, developing increasingly more specialised therapy to benefit human health. The rise of the pharmaceutical industry and the research it drives are contributors to this success. However, in humanity's attempt to tackle more and more complex health issues, the conventional methods used require adaptation. This is also true in the case of neurological disorders and diseases, which stem from the body's nervous system. While the nervous system possesses high responsiveness to chemical devices, these same devices can often not target specific locations at the required time. Therefore, solely depending on chemical delivery stagnates progress in overcoming the ailments' negative effects on both health and quality of life. It is here that an argument is made for therapeutic delivery through another modality. Manufacturing such technology creates complex engineering challenges and demands close cooperation between engineers and clinicians.

In this thesis, fundamental research is done to aid the investigation of efficient acoustic delivery with focused ultrasound. It is part of an ongoing effort to make therapy for neurological disorders and diseases less invasive and more effective. The modality of ultrasonic waves promises great potential in this respect, being able to image and modulate neural activity.

The work presented here shows the development of a research platform to effectively study the biophysical mechanisms that are responsible for ultrasonic neuromodulation. Using microfabrication techniques and 3D printing the basic elements of the platform could be manufactured. During electrodeposition, silver layers were grown to construct the Ag/AgCl electrode and insight was gained into the process. Electrophysiological measurements show the platform's capability to measure bilayer lipid membranes, which were manually prepared and suspended.

Contents

List of Figures

List of Tables

Nomenclature

Abbreviation	Definition
2D	2 dimensional
3D	3 dimensional
Au	gold
Ag	silver
AgCl	silver chloride
$AgNO_3$	silver nitrate
BLM	bilayer lipid membranes or black lipid membranes
CA	chronoamperometry
CAD	computer-aided design, design software
CE	Counter electrode, part of electrochemical setup
CMOS	complementary metal-oxide-semiconductor, semiconductor device technology
CPE	constant phase element
CV	cyclic voltrammetry
DC	direct current
DI	deionised water
DPhPC	1,2-diphytanoyl-*sn*-glycero-3-phosphocholine
EIS	electrochemical impedance spectroscopy
EMI	electromagnetic interference
$FeCl_3$	Iron(III) chloride
GDSII	Graphic Design System II, file format
HCl	hydrochloric acid
IPA	Isopropanol alcohol, liquid chemical
KCl	Potassium chloride
NH_3	aqueous ammonia
Nlof	negative photoresist, used for lift-off
O	oxidizing agent
O_2	oxygen gas
PA	pulse average, acoustic intensity metric
PLA	Polylactic acid, thermoplastic material
PGMEA	Propylene glycol methyl ether acetate, SU-8 developer
PTFE	polytetrafluoretheen, teflon, fluoropolymer material
PP	polypropylene, thermoplastic material
Pt	Platinum
PZT	Lead zirconate titanate, bulk piezoelectric material
R	reducing agent
REF	Reference electrode, part of electrochemical setup
SNR	signal-to-noise ratio
SPTP	spatial peak temporal peak, acoustic intensity metric
SPTA	spatial peak temporal average, acoustic intensity metric
SCPI	standard commands for programmable instruments, programming language
SEM	scanning electron microscopy
SU-8	negative photoresist, photoactive epoxy, used for high aspect ratio structures
STL	Standard Tessellation Language, file type for 3 dimensional objects
US	ultrasound
USNM	ultrasound neuromodulation
WE	Working electrode, part of electrochemical setup

Symbol	Definition	Unit
c	Acoustic speed, sound speed	[m/s]
C	Concentration	[M]
E_{cell}	Cell potential	[V]
E^0	Standard potential	[V]
$E^{0\prime}$	Formal standard potential	[V]
F	Faraday's constant, sound speed	[C/mol]
I	Current	[A]
I_{SPTP}	Acoustic intensity	[W/cm^2]
I_{SPTA}	Acoustic intensity	[W/cm^2]
n	Moles of electrons	
P_{SPTP}	Pressure	[Pa]
R	Resistance	[Ω]
R'	Acoustic reflection coefficient	
T	Tempature	[K]
T'	Acoustic transmission coefficient	
V	Voltage	[V]
Z	Acoustic impedance	[Rayls]
ρ	Density	[kg/m^3]

1 Introduction

Humans have a nervous system, of which our brain and spinal cord form the central nervous system (CNS). This system is responsible for the handling of complex information and is consequently subject to many fields of research. The information is processed through cascades of neural activity originating from the sensory organs. Additionally, it is known that the cortex itself exhibits activational patterns that seem to be related to intrinsic activity even in the absence of sensory input[1]. Because of the sheer amount of connections within neural tissue, a well-founded understanding of the functioning neural networks is still in its infancy. This hinders the ability to treat neurological disorders that originate from the malfunctioning of these networks. It is clear that the scientific fields of cognitive and systems neuroscience as well as neurophysiology, still have much to offer in uncovering these mysteries.

Technology can produce a window through which scientists can take a peek at the complex mechanisms at play in each of the respective fields. Although there are great advancements in the simulation of neural complexity *in-situ*[2], it can only complement empirical observation that is required for understanding the CNS. Tools such as fMRI and EEG can be used to record neural activity in real time. Still, to uncover clear causal relationships between activational patterns and their result, a neural recording must be paired with artificial excitation of neural tissue. The need for manipulation of neural activity led to the field of neuromodulation. Employing multi-modal neuroimaging[3] alongside stimulatory technology tremendously increases the potential to treat neurological disorders. The technology would not only increase research capabilities for this purpose but also offer the potential for implantable therapeutic devices [4, 5, 6, 7] with considerable advantages.

1.1. Background

1.1.1. Neuromodulation

The ability to modulate neuronal activity by means of non-destructive methods is of great interest to neurological research. It can be used to alleviate, cure or even prevent neurological diseases and disorders. Neuromodulation can presently be achieved through several modalities, each with its own benefits and detriments. The prevalent modality is the chemical manipulation of neuronal activity with medication, also known as neuropharmacology. This field of research is well established, but still rapidly growing due to increased demand for solutions for neurodegenerative diseases such as Alzheimer's and Parkinson's, but also psychiatric disorders [8]. Outside chemical delivery, neuromodulation is achieved by electrical [9, 10], optogenetic [11], magnetic [12], and ultrasonic [13, 14], stimulation [15]. These categories inherently possess a high spatio-temporal resolution because of advancements in their technology. Similar spatial resolution can also be achieved by chemical vesicles, which carry drugs and release them at the target site [16]. However, targeted chemical delivery for neurological disorders is tested only in a few human clinical trials [17] and seems difficult to realise in a closed-loop fashion with fast response times [18]. The increase in temporal resolution provided by non-chemical modalities enables real-time interventions and potentially allows for well-targeted treatment while limiting side effects. Although each of these methods enjoys different qualities, their rapid advances are all triggered

by the new possibilities in microfabrication technology which are fundamental to their implementation. The real-world presentation of this technology is mostly realised in devices, preferably implantable. Exemplar devices are deep brain stimulators for the treatment of tremors and epilepsy[19]; retinal implants for restoration of sight[20]; or even prosthetic limbs [21].

1.1.2. Ultrasound

The discussion concerning the differences between these high-resolution neuromodulation categories is portrayed in detail by other research [15, 22, 23], and will not be elaborated on here. In this thesis, a focus is put on ultrasound neuromodulation (USNM), which boasts minimal invasiveness and satisfactory spatio-temporal resolution. USNM is typically realised through the use of ultrasound (US) transducers which can convert electrical potentials into acoustic waves. The produced acoustic waves can stimulate or inhibit action potentials in neural tissue.

USNM dawns the engineering challenge to produce focused US waves that are able to pass the skull, while also minimising the energy needed to power the device at hand. This yields the need for a holistic understanding of the USNM devices, in relation to their microfabrication constraints, power efficiency, acoustic parameters used, and neuromodulation efficacy.

Additionally, from an academic perspective, there is an ongoing investigation of the fundamental biophysical mechanisms responsible for USNM. It has been uncovered that single neural cells independently activate after an ultrasonic stimulus [24], and so a cell within its tissue environment must have sufficient components to explain at least part of the mechanisms. Single neuron activity, such as an action potential, is by definition related to ionic displacements over a cell membrane. Therefore the membrane is the main subject of research together with the ionic channels that it incorporates. Specifically, the importance of mechanosensitive ion channels found in cellular membranes has been established [24]. However, the research done in this field has still been unable to produce an unequivocal explanation for the interactions and precise relationship between ultrasound and ion channels.

The investigation has now been grounded by its approach, from which can only be escaped by striking a different path to observe the mechanisms of interest. The studies done have been able to prove mechanisms on a cellular scale, leaving the exact physical effectors unknown. This can be attributed to two limitations: restricted independent control of acoustic parameters and the inability to measure the molecular mechanics at this cellular level. Additionally, the techniques used, such as calcium imaging and patch clamping, do not illuminate the fundamental behaviour of mechanosensitive ion channels, thus not revealing insight into the key mechanistic mediators. Furthermore, an ensemble of secondary US effectors on the membrane obscure the central physical contributor. These effectors include thermal effects [25], membrane cavitation [26], and radiative forces [27], all have consequently allowed different hypotheses to be satisfied.

With these studies, another complication arises, which is the lack of comparability between them. Unable to match the distinct provided US stimuli as well as the various subjected biological models over multiple studies will not provide confidence in their conclusions. Tackling the question from different angles is fruitful unless the solution presents a different face to each one.

Cutting the Gordian knot, a novel system will inevitably need to monitor the dynamics of mechanosensitive ion channels directly through their ion translocations. Sampling these events will require high temporal resolution and sensitive electrophysiological registration. The system may find itself as a platform testing a range of channels for a spectrum of US parameters. As such the system is a biological model able to robustly display the molecular fundamental mechanics of USNM with minimised bias.

Therefore, it is opted to investigate these biophysical mechanisms *in-vitro* on bilayer lipid membranes (BLMs), as a cell membrane surrogate. BLMs form measurable interfaces and can therefore be harnessed to experimentally investigate their electrophysiological activity when subject to US stimuli. Incorporation of individual channels into the BLM within such a setting has shown to be possible [28].

1.1.3. In-vitro experimentation

For conclusive determination of the mechanisms responsible for USNM, one must rule out as many confounding influences as possible, while having absolute control over as many independent variables as needed. For abstraction purposes, the latter is captured in the categorical biological entities tested

and the acoustic parameters they are subject to. Other factors are standardised to practically reasonable and representative levels, which is possible in *in-vitro* setups.

The acoustic parameters are primarily the source frequency, received intensity, and temporal patterning of the US signal. These parameters are currently differently represented in literature, leading to the unresolved question of their exact influence. Even after the separation of tissues in the peripheral nervous system from the CNS, the acoustic parameters do not show a clear correlation with the suppression or inducement of neural activity [29, 14, 30]. This together with the use of various neural tissue and the discrepancies between in-vitro and in-vivo experiments produces an ensemble of dependent variables out of which conclusions are difficult to draw. As stated by Darrow[31]: *"Novel experimental paradigms must be developed and employed to characterize the effects of ultrasound over this parameter space"*. Exploring this parameter space requires a setup capable of independent manipulation of each individual acoustic parameter.

The biological entities, in contrast to the acoustic parameters, are categorical, which does not fare well with a standardised setup that aims to achieve easily quantifiable differences. A biological entity needs a tailored environment to provide time-invariant observations. This is only possible when the tested range of entities can be stable in the same environment, and the environment allows them to operate with a high degree of authenticity. In this case, the biological entities thought to play a major role in the biophysical mechanisms of USNM, are the membrane and the mechanosensitive ion channels.

A study conducted by Hartel et al.[32] and the accompanying tutorial review Hartel et al.[28], show the possibility of performing electrophysiological measurements of the membrane incorporating a single ion channel. The authors prove it to be possible to separate the conductance states of the ion channel using high bandwidth circuitry. Continuation of this idea - specifically the use of mechanosensitive ion channels and the integration of a controlled US stimulus into the platform - would indeed allow for standardised measurement of the key players responsible for USNM. The idea is conceptualised in Figure 1.1.

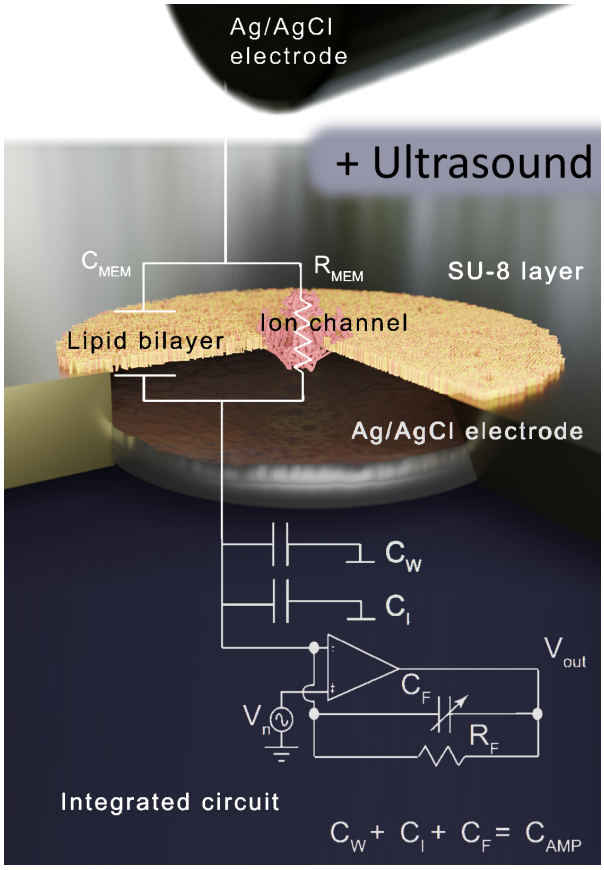

Figure 1.1: The research platform concept based on the platform from Hartel et al.[32] and adding the integration of ultrasound.

1.1.4. Thesis rationale

It is for these reasons that a platform for systematic testing should be developed to enable easy and reliable investigation of different US parameters and biological species. The platform would need to be biocompatible and include electrodes for the measurement of ionic currents and for driving the US source. This effort was made primarily to pave the way to a more conclusive answer on the biophysical mechanisms responsible for USNM. Although it is known that mechanosensitive ion channels within the cell membranes of neural tissue are at least partly responsible for the ultrasonic modulation of action potentials, other secondary effectors like temperature and cavitation might also contribute to the observed effects. To record the electrophysiological activity of a sample in the same temporal range as the US signal, the read-out circuitry ought to be of high bandwidth in order to resolve the responsible biophysical events. Satisfying the high bandwidth requirement while allowing the formation of a stable membrane leads to the need for small biocompatible microwells (10 to 250μm). Specifically, the suspension of BMLs on micro-wells and the future incorporation of mechanosensitive ion channels into these membranes will reveal details about the biophysical complexity of USNM.

This thesis will address the end-to-end fabrication of the complete platform and its validation testing. The main research question of this work is formulated as follows:

> **How can micro-wells that support bilayer lipid membranes be fabricated and integrated into a setup that minimises acoustic reflections from the substrate while allowing for the measurement of electrophysiological activity?**

The design, fabrication and testing of a platform with such microwells are done in this thesis project. Specifically, this thesis will elaborate on the workings of the microfabricated front-end, the ultrasound source, and the packaging that has been developed. The fabrication of the electronic circuit responsible for high bandwidth measurement is outside the scope of this work. Its function is replaced by an external potentiostat, with which platform validation tests were performed. These tests include the validation of the electrochemical properties of the front-end electrodes and the suspension of the lipid bilayer in which an ion channel can be incorporated.

The outline of the thesis is structured to firstly, provide the background of setup components; secondly, explain setup operation; and thirdly, discuss experimental results.

Starting from the contemporary knowledge in Chapter 2, where the acoustic, biological, electrochemical, fabrication, and packaging aspects are separately discussed. The setup design and its engineering considerations, followed by the fabrication methods and integration of the experimental setups are presented in Chapter 3. Within the latter, some additional theoretical support is provided to guide the reader through motivations and the needed considerations. Then, the setup's validation results are presented at each respective project stage in Chapter 4. The most consequential results are discussed in Chapter 5 followed by the conclusion and recommendations for further research in Chapter 6.

2

Theory

To substantiate design choices and explain the motivations for particular methodologies used, some theoretical background is required. The theory explained in this chapter is intended to serve as such. Additionally, it provides a theoretical summary of the different aspects relevant to the question at hand.

2.1. Ultrasound

Ultrasound (US) is made up of acoustic waves that possess relatively high frequencies ($> 20kHz$) and therefore small wavelengths. This property gives US waves a high spatial and temporal resolution, essentially by attribute of their high-pressure gradients. By controlling the generation of US, either by using a phased array of transducers [33] or a single focussed element transducer, a high-resolution focal pressure spot can be produced. The electrical or mechanical steering of the focal spot allows researchers to directly stimulate particular regions in biological tissue. This forms the basis of ultrasound neuromodulation (USNM), which is the research application of this thesis.

Acoustic waves are periodic pressure variations that progress radially. The pressure variations in acoustic waves can be mathematically described by wave equations, as well as the reflections found at phase boundaries. The speed of acoustic waves is dependent on the medium's compressibility and density, whereas their periodic frequency is established by the acoustic source.

Although precise time-dependent evaluation of the wave is possible, the acoustic signal is described by single value metrics. Descriptions of the acoustic signal's magnitude are captured in pressure or intensity metrics which are related to the acoustic impedance of the medium at hand. This impedance is again related to the medium's compressibility, κ, and its density, ρ [34]. This implies high impedance media are associated with having a high density and speed of sound. Assuming constant density, an acoustic signal entering a higher sound-speed media will increase its wavelength since the frequency is constant. Its intensity, however, drops because of the increase in acoustic impedance. This is illustrated in Figure 2.1 (c).

$$\text{Intensity } I = \frac{p^2}{2Z}, \qquad \text{acoustic impedance } Z = \rho c, \qquad \text{speed of sound } c = \frac{1}{\sqrt{\rho\kappa}}. \tag{2.1}$$

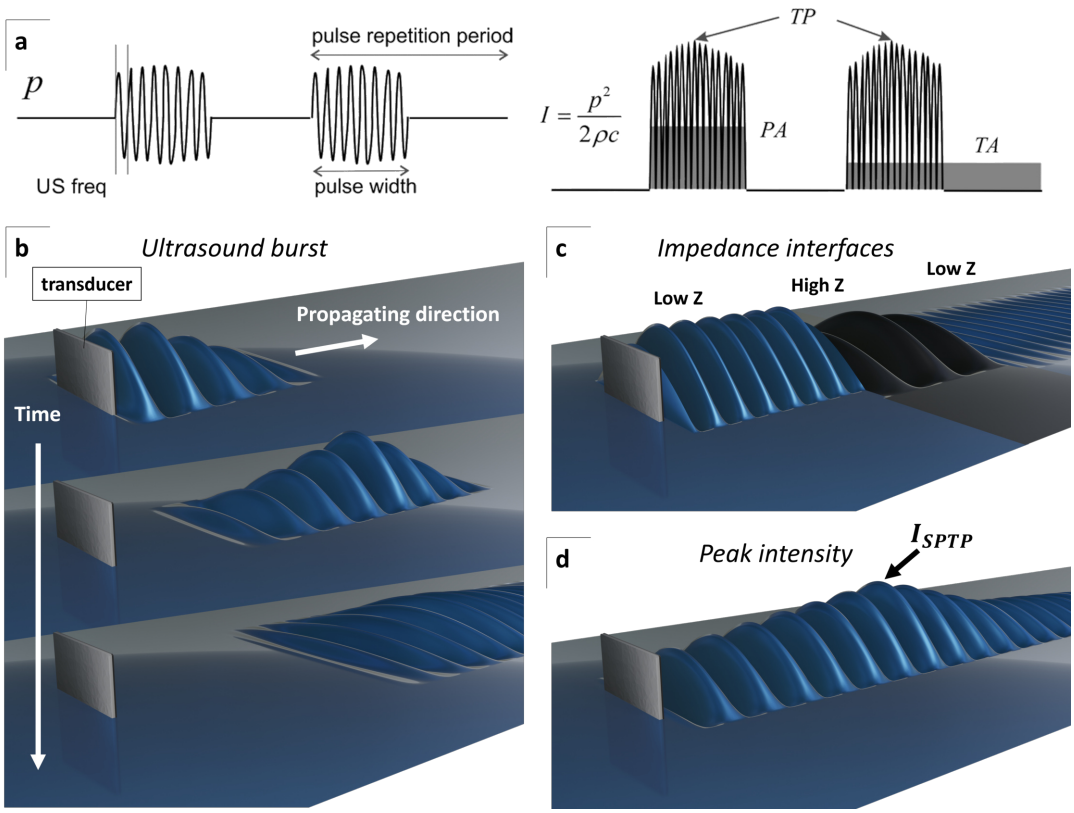

Figure 2.1: Each figure shows a schematic representation of an US transducer in a medium. The displacement in the medium is a graphic depiction of the pressure generated in the medium (in reality these are 3D longitudinal waves). *(a)* The temporal pressure and intensity of US, adapted from [29]. *(b)* An acoustic burst at 3 different points in time. Top: just after the burst is generated; Middle: the burst has traversed some distance and reached its natural focal spot; Bottom the waves attenuate due to their radial expansion. *(c)* An acoustic signal travelling through a high impedance medium, where its wavelength increases but the intensity drops after each interface. *(d)* A constant acoustic signal with its spatial-peak temporal-peak point of intensity labelled.

For both pressure and intensity, summary statistics in the spatial and temporal domains are taken in the form of averages or maxima. Spatial peak (SP) and spatial average (SA) are the maximum and mean magnitudes of the signal, respectively. Acoustic signals in the time domain may be composed of bursts of pulses, as shown in Figure 2.1 (a,b). Therefore, time domain averages can be established over the pulses within the burst, burst averaged (PA); or over the complete burst cycle, temporally averaged (TA); although the maximum value can also be obtained - temporal peak (TP) [29, 14]. The spatial-peak temporal-peak (SPTP) is conventionally used as a metric for comparison of the sourced intensity of simple transducers as seen in Figure 2.1 (d).

To quantify the losses of acoustic signal magnitude, one must take into account absorption, reflection, and refraction at phase boundaries. Assuming ideal transmission the inverse square root of the acoustic impedance ratio determines the ratio of acoustic pressure observed inside the media. However, when the acoustic signal is incident to a relatively high impedance medium the fraction of reflected energy, R', can not be neglected. And by conservation of total energy, the remaining fraction, T', corresponds to the transmitted intensity.

$$R' = \frac{(Z_2 - Z_1)^2}{(Z_2 + Z_1)^2}\,, \tag{2.2}$$

$$T' = 1 - R'\,. \tag{2.3}$$

Absorption and scattering effects are frequency-dependent losses of the acoustic signal. Although their mathematical formulation is possible in combination with experimentally derived data [35, 36], these effects are not prime contributors to the experimental work discussed here.

Lastly, the radial dispersion of the ultrasonic signal leads to an intensity drop relative to the inverse of the distance-to-source squared:

$$I(\bar{x}) = \frac{I_0}{\bar{x}^2}, \qquad \text{where} \quad \bar{x} : \text{distance from source}^1. \tag{2.4}$$

In-situ simulations of US wave evolution [37] provide a baseline prior to experimental research. Still, this generates only the restrictive conclusions attainable from mathematically ideal conditions, when in fact reality is more complex. Effects such as near-field variations, reflections, source non-linearity, and frequency modes complicate the translation of simulated results to the real world.

2.1.1. Ultrasound neuromodulation

The fact that US is capable of influencing neural activity was demonstrated almost a century ago [38]. Since then it has been shown that US is capable of suppressing and inducing action potentials [29, 14, 30]. Additionally, the US signal can be spatially and temporally focused to target a specific area for an indicated time. Recently, there has been an upsurge in US research, specifically, the low-intensity focused US. This has been with the motivation to aid medical research for the treatment of neurological disorders. Before low-intensity, the high-intensity focused ultrasound was already discovered as a potential modality for the treatment of a different class of neurological disorders [39, 40]. Its highly focussed energy is also used for lesioning procedures. These are primarily in the context of tumour ablation, for which commercial devices are available for clinical application [41, 42].

In contrast, low-intensity focused US attempts to provide as little energy as possible to the tissue while modulating neural activity. The steering is commonly achieved through the use of 2D planar phased array ultrasound transducers. Digital control over the transducers allows the output US phases to constructively interfere at a specified point in space. However, the control of US intensity in biological tissue is notoriously difficult due to the inherent heterogeneity of the tissue. It requires complex attenuation computations on anatomy specific tissue compositions [43, 29]. Essentially, the problem is accurate steering of the focal spot, although already efforts are made to integrate a secondary US imaging array to find the primary US focal spot [44, 45]. A device capturing such technology would imply a very high degree of neuromodulatory control. Until the realisation of such technology, *in-vitro* systems provide controlled measurements of biological samples, whereas *in-vivo* systems cannot guarantee the acoustic intensity exposed.

2.2. Biological components

For a more comprehensive understanding of the key biological components responsible for USNM an understanding is given in this section. Bilayer lipid membranes and ion channels are these components. They are important biomolecular building blocks of neural cells and are positioned on top of the platform's fabricated microwell.

2.2.1. Bilayer lipid membranes

To understand the membrane structure suspended on top of the microwell, it is best to start with its molecular component: the phospholipid. A phospholipid is a biomolecule, approximately 2 nanometers in size, consisting of a hydrophobic tail and a polar head group. These properties make phospholipids indissoluble in polar solutions such as water, in which they instead cluster together to minimise the exposure of their hydrophobic tail. This clustering manifests itself in a bilayer structure: non-polar tails in and polar phosphate heads out either as a vesicle or a membrane as seen in Figure 2.2 (a). These structures are seen everywhere in biology since all cellular life possesses membranes. Primarily, cell membranes by definition encapsulate cells and carry functions in cell regulation and cell communication. They form a barrier between the inside and outside of a liposome, an organelle, and the cell itself.

[1] When the path has reflections the cumulative distance from the source must be taken. The intensity does not account for interference with the sourced intensity at different time points.

Although there are many types of phospholipids, each with a particular charge distribution and influence on the final BLM stability, the main characteristics of a BLM system can be generally described. Inside the context of a cell, many other components also interact with the membrane structure. In cells, these are membrane proteins (e.g. ion channels) that are found within or near the bilayer, but also the complete cytoskeleton organelle which are the "bones" of the cell. These together with many more cellular components regulate membrane curvature and structure. The cytoskeleton introduces curvature and thus stress in the membrane. Whereas proteins edit the surrounding microenvironment, generate porosity, and create local deformations. With respect to this work, it is important to note that such local and global BLM modifications alter the electrophysiological properties of the membrane [46].

Although many precise molecular considerations surpass the scope of this work, an understanding of the physical mechanisms by which phospholipid interactions constitute to macro behaviour of the BLM, is of interest to theorise possible biophysical mechanisms responsible for USNM. Also, experimental derivation into BLM systems unequivocally means measuring macro properties, because of physical and practical limitations. Deconvoluting the observable macro behaviour to responsible micro dynamics within the membrane is also required for establishing a complete theory of the mechanisms of interest.

The lipid named 1,2-diphytanoyl-*sn*-glycero-3-phosphocholine (DPhPC) was selected over the many other commercially available types, because of its inherently high stability in bilayer formation. DPhPC is a type of (glycero)phospholipid and is thus suitable for the particular use case at hand. These specific lipids have also been used in prior research, showing their capability of self-assembly in *in-vitro* environments and use in electrophysiological measurements [47, 48].

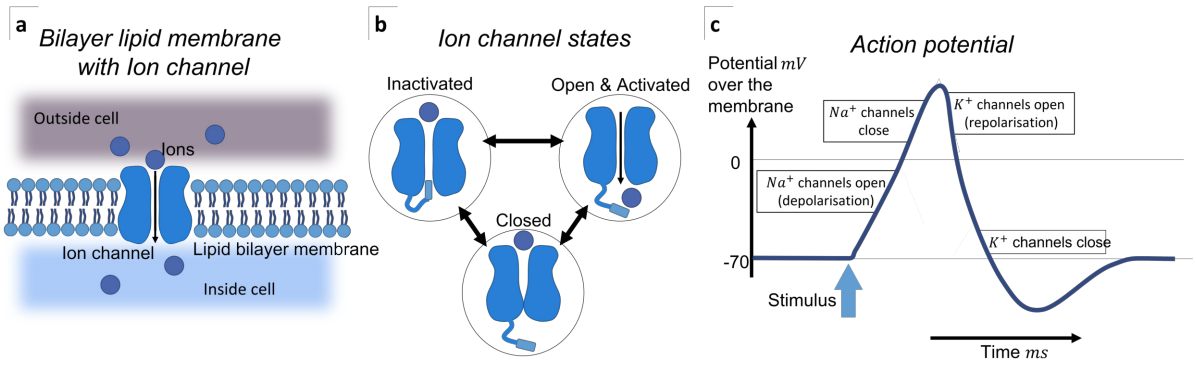

Figure 2.2: *(a)* Lipid bilayer membrane with incorporated sodium (Na^+) ion channel. *(b)* Different ion channel states. *(c)* Action potential in a neuron. A plot of the voltage in mV over the membrane vs the time in ms.

2.2.2. Ion channels

Ion channels are proteins capable of transporting ions through a cell membrane. There are many channel types, each transporting its designated ions differently. In the membranes of excitable cells, these channels play an active and passive role in establishing the action potential, as presented in Figure 2.2 (c). The action potential is a hallmark of the nervous system which conceptualises the generation of an electrical signal over the membrane of an excitable cell. The so-called firing of a neuron is the result of a cascade of action potentials along its membrane, which eventually may activate other neurons, ultimately giving rise to neural activity.

Proteins are built up from strings of peptides, together forming secondary structures, which again arrange into tertiary structures, and can combine to build quaternary structures. All these subunits may be dynamic, allowing proteins to change shape between conformational states. This is also true for ion channels as illustrated in Figure 2.2 (b), where these states are also known as conductance states because each conformation state's shape is associated with a specific conductance value. Any shift between conduction states is called a gating event and is influenced by the local molecular environment. Gating events are not the only kind of molecular dynamics, in which certain kinetics can contribute to the ion specificity of a channel and [49].

Characterisation of the molecular dynamics can be done indirectly through measurement of the ion channel's conductance states, therefore uncovering the mechanisms by which it operates. Accurate *in-vitro* assessment of these states involves high-bandwidth measurement to resolve the gating events. An implementation of a system capable of such measurements is discussed in the study by Hartel et al.[32]. Here a platform is described which integrates a BLM-ion-channel system on top of complementary metal-oxide-semiconductor (CMOS) technology. Essentially, the work shows how miniaturisation of the membrane and readout circuitry can lead to high bandwidth recording. This bandwidth improvement can be ascribed to the decrease of membrane capacitance and the parasitic capacitance of other system components.

Observation of ionic displacements and action potentials in neural tissue is commonly achieved through calcium imaging. It is a method enabled by the use of genetically encoded calcium indicators (GCaMP), a protein that fluoresces when binding with calcium ions. This consequently reveals action potentials within entire neural circuits. Current state-of-the-art fluorescent protein sensors (GCamP6f) allow such studies to push the imaging temporal resolution to the order of milliseconds [50].

In an imposing study carried out by Yoo et al.[24], macro characteristics are measured to determine the contribution of single proteins inside the cell membrane in neural tissue. The authors also identified the calcium response as a primary initiator in the US response. Therefore, the relative contribution of ion channels is investigated using calcium imaging. Specifically, channels with mechanical activation, called mechanosensitive ion channels, are shown to play an important role. To examine the individual ion channel species' performance, pharmacological blocking and genetic knockdowns are introduced by the researchers. The accomplished sequence of experiments shows the important contribution of specific mechanosensitive ion channels.

In-vitro studies such as this one are important to establish the responsible biological pathways and greatly increase the understanding of the biophysical mechanisms investigated. Still, they do not provide much quantitative information about the effect of the acoustic parameters. These parameters are known to dramatically alter the neural response [29, 14], and therefore call for further investigation. Investigating this aspect requires specialised electrophysiological measurement of an isolated ion channel.

Electrophysiological measurement provides a more direct observation of ion translocations through the ion channels at hand. After the successful setup of a membrane with an ion channel, the application of a voltage over the membrane generates the electric field needed to push ions over the channel. The reorganisation of ion concentrations is then registered at the electrode interface through a particular complex of electrochemical pathways. Combining this setup with a controllable acoustic stimulus provides a platform capable of systematically surveying the influence of acoustic parameters on the prominent biological components in USNM.

The realisation of the platform however is not trivial, and neither is the understanding of basic electrochemistry needed for proper interpretation of the results of an electrophysiological measurement.

2.3. Electrochemistry

To mobilise charges over an electrochemical system and read the resulting charge characteristics, the basis of electrochemistry needs to be understood. This is also true in the case of electrophysiological measurement, which involves electrochemical interactions. Although an in-depth description of the applied electrochemical process is out of this work's scope, some fundamental principles in the field require elaboration for consequent topics.

2.3.1. Measurement setup

Electrochemical measurements are quantised by either the translocation of electrons or the build-up of an electric potential. They are measured in current and voltage, respectively, at the terminal over a series of different phases. For this thesis, the theory can be limited to solid-liquid interfaces, physically corresponding to the electrode-electrolyte boundaries. Electrons will mobilise inside the solid electrodes, whereas, ions will start to move inside the liquid electrolyte. At their interfaces, there will either be a build-up of opposing charges, or a redox reaction. In a redox reaction, an atom gains or loses an electron, termed reduction and oxidation, respectively. Each of the phases and their interfaces along such a path influence electrical reactance and resistance. A typical electrochemical pathway where two

electrodes are immersed in an electrolyte can be denoted by the respective chemical species separated by a vertical line as such: electrode|electrolyte|electrode. The electrode where reduction happens is called the cathode, while oxidation happens at the anode. When the reaction is spontaneous, the cell is said to be galvanic, a potential or current will appear as the reactions progress. Whereas non-spontaneous cells require an externally applied voltage and are called electrolytic, a potential or current is applied to drive the reaction. This is schematically illustrated in Figure 2.3 (a,b).

Measurement of electrochemical systems is practically achieved by immersing electrodes into the electrolyte. A four-electrode setup separates the current and voltage control, quite similar to a Van der Pauw measurement in solid-state characterisation. There is a sense electrode (SE) from where the voltage is measured with respect to a reference electrode (RE). Then the current pathway is formed over a working electrode (WE) and a counter electrode (CE). However, in practice, three-electrodes setups are more applied, where the WE and SE are shorted. In a two-electrode setup, the CE and RE are also shorted. The two- and three-electrode setups have been used in this work and are shown in Figure 2.3 (c,d). The motivation for the number of electrodes used is dependent on the application [51, 52].

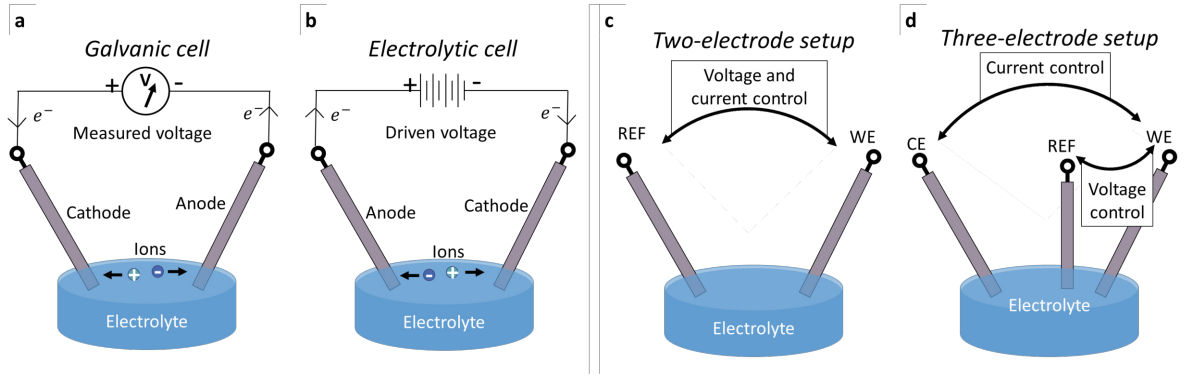

Figure 2.3: *(a)* A galvanic and *(b)* electrolytic cell. *(c)* A two-electrode setup and *(d)* a three-electrode setup. WE = working electrode, REF = reference electrode, CE = counter electrode.

In electrochemical measurement, the use of any electrode must be carefully considered, since the introduction of any component into the system greatly increases the possibility of measuring unforeseen chemical pathways. Especially in an environment that is not fully controlled, unanticipated reactions can have a big impact on the measured signal and lead to erroneous conclusions during its interpretation.

2.3.2. Chemical potentials

The notion of 'potential' in electrochemistry is confusion compared to its solid definition in the field electronics [53]. To illustrate this point, one can recognise that the potential difference measured over an electrode|electrolyte|electrode system only reflects the electrical work done by the system, while chemical and thermal work is left unappreciated. Additional complexity arises in the concept of potential when the initial charge reorganisations are considered. These charge reorganisations produce electric fields at the phase boundaries which in turn influence the chemical species' activity.

Cell potential

While appreciating the non-linearity of the inevitably complex system dynamics, the potential discussed for the remainder of this thesis is the cell potential, E_{cell}, unless stated otherwise. This cell potential thus pertains to the net electrical work done by the system as a whole and is always relative to the reference electrode in the electrochemical system. A high-impedance voltmeter can be connected to the terminals of the cell to directly observe the cell potential.

Standard potential

Assuming a steady availability of electrons (i.e. constant current), chemical species' tendency to reduce is dependent on the reduction potential also called the standard potential, E^0. This potential depends on the species' electron affinity. Absolute standard potentials are hard to determine and of limited practical value since they describe the chemical species outside of their immersed state. Therefore, the standard

hydrogen electrode (SHE) is by convention assigned as the reference potential. The reduction of two dissolved protons to hydrogen gas is defined as having a standard potential of zero. From left to right:

$$2\,H^+ + 2\,e^- \rightleftharpoons H_2(g), \qquad E^0 = 0. \tag{2.5}$$

The same reaction from right to left is the corresponding oxidation reaction, and its oxidation potential has the opposite sign. The standard potentials of most reactions are empirically determined and tabulated in databases. More accurately the activity coefficients of the involved chemical species can be incorporated into the equation yielding the formal potential $E^{0'}$. However, standard potentials are regarded as a good approximation, where activities can be approximated by species concentration in the absence of chemical effects in the medium [51].

After the determination of possible redox reactions, the potential at which these reactions take place can be theoretically ascertained. Besides the intensity and directionality of the reduction and oxidation reactions at hand can also be identified. The intensity depends on the thermodynamic electrochemical equilibrium, which is for instance influenced by the reaction kinetics, temperature T, and available concentrations of reaction products. Assuming standard conditions and complete reversibility, the directionality can be immediately observed from the sign of the reduction potential alone. The potential outside the standard conditions can be modelled using the Nernst equation [51], where C_O and C_R are the concentrations of the oxidating and reducing species, respectively.

$$E = E^0 + \frac{RT}{nF} \ln \frac{C_O}{C_R}, \qquad \text{for reaction} \qquad O + ne^- \rightleftharpoons R. \tag{2.6}$$

In practically realised electrochemical setups, the reduction reaction is paired with an oxidation reaction allowing control over the electron transfer directly. The reduction and oxidation reactions here form half-reactions contributing to an electrochemical cell. From both, the value of the potential at rest can be approximated.

Open circuit potential

Like the contact between two solid (semi)conductors materials can introduce diode-like behaviour due to a difference in work functions (and electron affinity for semiconductors), electrochemical interfaces can form build-in voltages [54]. However, unlike solid devices, electrochemical systems contain fluid phases capable of double-layer charging effects, redox reactions through faradaic pathways, and secondary effects.

Reduction and oxidation potentials at the working electrode mark the cell potentials where a cathodic or anodic current is forced. In between these potential limits, the system can settle. The cell potential of a system in these conditions is termed its open-circuit potential (OCP). The exact value depends on trace impurities and the aforementioned effects. The observed potential ultimately is the result of relative charge build-up at the working electrode with respect to the reference electrode [51, 55].

2.3.3. Electrochemical measurement

Driving charge over an electrochemical system is conventionally done by either controlling the current or potential and measuring its resultant counterpart, which is termed the galvanostatic or potentiostatic measurement, respectively. To quantify the resultant current or potential, the number of electrons is directly measured. Conventionally this is measured as $6.242 \cdot 10^{18}$ electrons in a coulomb (C), used in conjunction with the electrochemical number of $6.022 \cdot 10^{23}$ electrons in a single mole. And dividing these constants yields the Faraday constant, $F = 96485.3 C/mol$. This constant portrays the passage of coulomb which will contribute to a single mole in a chemical reaction.

Chronoamperometry

Chronoamperometry (CA) is the method where potential is applied at the working electrode with respect to the reference electrode and the current is measured as a function of time [51]. Essentially the method measures the potential step response and shows fast dynamics initially after reaching a steady state. In absence of redox pathways, the steady-state quickly introduces a low signal-to-noise ratio (SNR). Many electrodes (base metal, or Ag/AgCl) operate within reduction or oxidation conditions, and the constant supply of electrons will introduce redox reactions. The steady-state behaviour is in these cases dictated by the corresponding reaction rate until the finite reaction resources are depleted.

Cyclic voltrametry
Like CA, cyclic voltammetry (CV) requires the application of a voltage where the resulting current is measured. However, here the voltage is changed linearly between the set voltage limits. This results in a current trace as a function of voltage, where time is parameterised in the 'scan rate' in V/s. Unlike CA, CV never shows the system in equilibrium because of the constantly developing voltage. The degree to which the steady state is reached is then inversely related to the scan rate. Similar to CA, the availability of redox reactions within the voltage range used affects the measured response. Furthermore, the resultant characteristic depends on the reversibility of the charge translocations. Non-reversible reactions will show a difference between the anodic and cathodic currents observed.

Electrochemical impedance spectroscopy
The current observed in CA and CV measurement often consists of a complex of simultaneous electrochemical mechanisms that are difficult to isolate using chemical agents. Although many parameters influence an EIS measurement, the fundamental idea of EIS offers an attractive way of decomposing the electrochemical mechanisms. Namely, by changing the frequency of a small alternating potential (10mV) over the working electrode, the mechanisms limiting the current transfer over the electrode surface are separated due to their different response time. The resulting data acquired from such a measurement is a range of frequency-dependent impedance values, which are calculated by dividing the applied potential by the current observed. Additionally, the phase shift between the applied voltage and the resultant current is registered. This information is commonly compiled into a Nyquist- or a Bode-plot. The interpretation of such traces is accomplished by fitting the curves to a carefully chosen equivalent electrical circuit deemed to capture the chemical dynamics of the system. A manual indication of each electronic circuit component and its approximated initial value is needed for successful computational fitting.

This makes the interpretation of EIS results highly subjective to the experimenter's input. Ultimately electrical component values are estimated on an absolute scale, therefore each choice with a significant influence has to be justified. Similar to CA and CV this methodology depends on the practical realisation of a measurement setup, the prior conditions of all components, the used electrodes, the impedance spectroscopy system employed, and the parameter ranges specified. Tested samples are highly sensitive to environmental factors, which can cause considerable noise in the desired output values.

2.3.4. Electrodeposition
Like electrophysiological measurement, electrodeposition is another aspect of electrochemistry investigated in this thesis. During electrodeposition, a material is deposited on an electrode surface in an electrolytic cell. It conventionally employs galvanostatic measurement, to more reliably control the thickness of the layer being deposited. The volume of deposited material can directly be estimated by integrating the current over time, yielding the total charge that is representative of the number of ions reduced.

Still, the reactions at the cell's electrodes are determined by standard potentials. The intended reaction standard potential responsible for the deposition of a species can be found outside of the actual potential difference over the electrode interface. Precise control of the electric field over this interface requires a proper reference voltage. This implies a non-polarisable reference electrode, however by using galvanostatic control the steady state of the system is shifted by the reduction potential of a polarisable electrode as practised in Section 3.4. Still, the resulting potential difference over the interface is also dependent on the current applied, and attaining the intended reaction will require theoretical or experimental estimation of the current magnitude needed.

Another method to achieve high activity for the intended reaction to take place is to alter the properties of the immersed phase. Introducing reducing or oxidising agents may help to speed up the deposition reaction. Adjustment of the pH of the electrolyte is another avenue to reach the desired result, as was pursued in this work. For the latter, the Nernst equation can be adapted to yield the reduction potential of a reaction at a particular pH level. Commonly used in corrosion studies, a Pourbaix diagram presents the achieved phase at a specific cell potential and pH level. The plot can be constructed using the Nernst equation in combination with expertise about the possible reactions inside the potential-pH-landscape [56].

Many more material-specific considerations need to be made to get a satisfactory result. There are qualitative variables: seed layer material, anode composition, electrolyte solution, chemical agents used, prior cleaning, pre-treatment, conditioning, and electrical setup. But there are also many quantitative variables: electrolyte concentration[57], surface area of anode and cathode, their separation distance, voltage/current-density range, deposition time, and temperature. Additionally, actions have to be performed to help the setup approach ideal conditions. Sanding and conditioning of the sacrificial anode, but also agitation and filtration of the electrolyte might be needed [58].

In best practice, an existing recipe is used for electrodeposition with characterised results. This recipe can be adapted to receiving electrode's surface geometry and area to reach the desired deposit.

2.4. Microfabrication

In this thesis, microfabrication techniques were used to construct a substrate for the microwell with an electrode at its bottom. Here a brief overview of these techniques is provided. Most processes are robust and reliable fabrication techniques that profit from the research enabled by the semiconductor industry.

Starting with a wafer as the substrate, sub-millimetre patterns of etches or deposited metals, oxides, and organics are possible. This is done through the optical lithography workflow. The wafer is first coated with a photoresist. This layer of photoresist is then exposed to a partially masked UV light source. The mask is important since it determines the 2D pattern of light exposure to the photoresist, which only activates at the exposed portions. The polymers found in the activated photoresist can either be crosslinked (negative photoresist) or decomposed (positive photoresist), hardening them or making them more soluble, respectively. After this step, a chemical etchant (developer) is used to remove the soluble polymer leaving the patterned photoresist behind on the substrate.

The photoresist pattern forms the basis of all patterned layers in a microfabricated design. At this stage, one can either etch away the exposed substrate, oxidise it, or evaporate a thin layer on top of it. After the pattern transfer, the photoresist is removed yielding a patterned structure on the substrate. Having transferred multiple patterned structures onto the substrate a layered 3D design can be realised.

The described techniques were used in this project to build a range of passive chips with two patterned layers: gold and biocompatible photoresist. Many required steps to achieve patterned surfaces are omitted in the above description, like cleaning, baking, priming, plasma oxidation, mask alignment and lift-off. These are discussed in Chapter 3 in the context of the designed passive chips.

2.5. 3D Printing

Since the work described in this thesis depends highly on the integration of multiple components and their alignment, a package is required. It was chosen to use 3D-printed scaffolding to join together the various elements of the experimental setup.

Additive manufacturing or 3D printing is a fastly emerging technology composed of many different modalities. Generally, the sintering of powder, curing of liquid photopolymer, or melting of filament is employed to realise a specific 3D design. The systems handling the process are complex and dissimilar. Still, typically the 3D-printed part is produced through the delivery of focussed energy to successive locations on the part's surface where the material is consequently deposited. Whereas conventional manufacturing methods have a very long development time, additively manufactured parts do not suffer this fate. The speed at which a part can be created, re-designed for improvements and printed again, is one of the biggest advantages of 3D printing. Together with the freedom granted by digital design, this methodology allows for rapid prototyping, saving time and providing faster and more flexible research.

There is a vast field of engineering dedicated to additive manufacturing techniques, where each modality has its intricacies [59]. However, for the scope of this thesis, it was chosen to focus on material extrusion machines, specifically for the use of fused deposition modelling (FDM). This modality extrudes filament through a small heated nozzle which deposits lines or arcs of molten material which cools down and hardens on the part. After a layer of material is deposited the nozzle moves up to deposit the next layer on the previous one, ultimately creating the complete 3D part.

Unfortunately, FDM involves design limitations. Because after the initial layer the subsequent material has to be deposited on a previous layer, no floating or overhanging structures should be designed. Vertical structures can expand at approximately a 45° angle, needed to allow proper layer-to-layer adhesion. Although it is possible to use support structures (which are to be removed after printing) to aid overhanging structures, this requires post-processing steps that are in contrast with the idea of rapid prototyping.

The design of a 3D-printed structure is done digitally using computer-aided design (CAD) software. After this, the transfer of the digital design requires the creation of standard triangulated 3D object files (STL) containing the complete 3D part structure. This file must be interpreted by slicer software, calculating a set of paths for the 3D printer to successfully deposit the object in layers. The slicing of the 3D object involves many parameters which need to be customised and tested to fit the print at hand. The parameters used in this project were iteratively determined because of the unusually small part size, as is described in Chapter 3.

3

Methods

This chapter will describe precisely how the various aspects of the project were carried out. Firstly, the passive chips were designed and later fabricated in the EKL cleanrooms. Then the process of creating adaptive packages is explained. These served as the scaffolds during electrodeposition and electrophysiology. The exact silver electrodeposition on the microwell electrodes of the passive chips is elaborated upon. The acoustic characterisation is briefly touched upon, before going into the electrophysiological measurement methods and the preparation of the lipids.

3.1. Chip design

For the design of the chips the following key requirements were taken into account:

- Biocompatibility
- Fabrication simplicity
- Easy integration into the experimental setup

Biocompatibility is important to ensure the design is applicable beyond this single-use case and could also be used in other biological applications. Especially, since this project is part of a greater effort for ultrasound neuromodulation, future projects might profit from this quality. Making the design biocompatible, meant the use of biocompatible materials. Specific to this project, the use of hydrophobic material for the microwell was essential because it provides an anchoring point for the lipids during the assembly of a BLM.

The microwells needed required microfabrication in cleanrooms. Still, fabrication was kept as simple as possible by using a two-layer system. After these layers were in place, the silver-silver chloride (Ag/AgCl) electrodes would be constructed. Silver (Ag) could be deposited using electrodeposition techniques and chlorination would be achieved chemically.

Easy integration meant the chips should be conveniently handlable. This ultimately implies making the interfacing features large enough. Every feature, except the microwells, was therefore chosen to be visually identifiable simplifying alignment. The contact pads were sized up to form an accessible external electrical connection interface, and the individual dies were made big enough to grasp with tweezers.

Furthermore, the decision was made to design additional external connections and an extra electrode could be used in future work. Besides their use in testing, these were not employed during this project.

All these considerations were taken into account during the system design, preceding the photolithographic mask designs. The passive chips were designed as modular and simplistic units to prevent the possibility of unforeseen complications. This is especially important in the face of time constraints, since mask deliveries, fabrication steps, and lithography optimisations would hinder the possibility to continue beyond fabrication and execute subsequent steps in the project. The modular design unit consisted of a microwell surrounded by a ring electrode, its interconnects and contact pads. Another

bigger gold ring was added for visual indication during mounting, as well as an extra contact pad for a potential future connection. The units were arranged in an alternating fashion concerning their outgoing interconnect direction (north-south). This was done to fit more units and have the adjacent microwells spaced further apart. Each unit had a specific microwell diameter, either 5, 10, 20, 30, 40, 50, 60, 100, or 250μm. These specific dimensions were decided upon in the trade-off between fabrication yield, BML capacitance, and feasibility of membrane formation. The modular unit design is shown in Figure 3.1 (a,b) as well as their arrangement in the wafer design in Figure 3.1 (c). The microwell is found in the centre of the two rings. It was originally expected that the ring electrode components would only be used during later stages and therefore the contact openings were absent for half of the units to mitigate possible electrolyte interactions.

In order to minimise fabrication complexity while allowing silver electrodeposition, it was opted to use gold (Au) as the material for the interconnects and electrodeposition seed layer. The SU-8 was chosen as a biocompatible negative photoresist since it is well-characterised in the field of microfabrication. The SU-8 would be spun on the evaporated gold surface as well as the substrate. The use of 200nm thick, 100μm wide gold tracks was chosen since these form the reliable and highly conductive paths needed for the conduction of the electric signal. Both layers required a brightfield mask to establish their pattern. After design in commercially available software (Tannertools, L-Edit) the needed GDSII-schematics were produced. The gold and SU-8 patterns were printed on chromium-glass masks (MicroCreate BV).

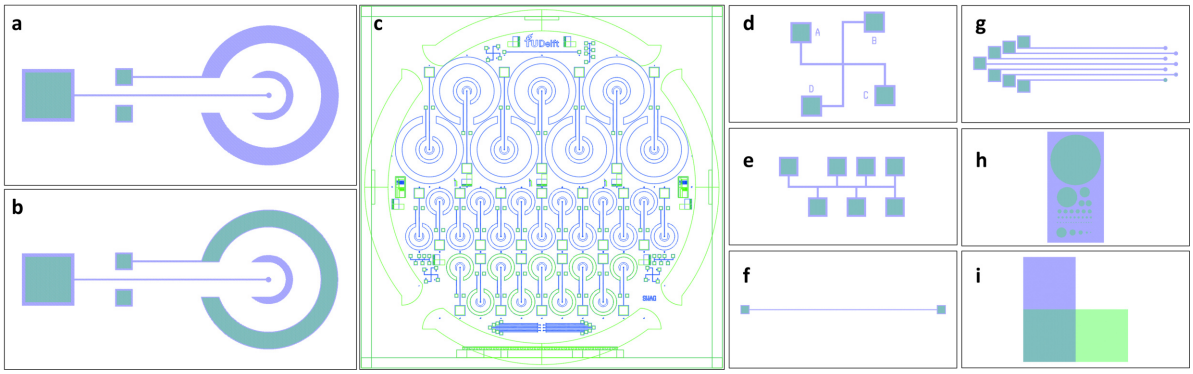

Figure 3.1: All microfabrication design layout elements. The green shaded regions indicate the masked area for the SU-8 mask, whereas the blue shade is for the gold mask. *(a)* The modular microwell unit without opened ring electrode. *(b)* The modular microwell unit with an opened ring electrode. *(c)* The outlines of the complete design of the two masks. *(d)* A greek cross, or van der Pauw's structure used for thin film resistance characterisation. The short arms are 1mm in length, the longer arms connected to the centre of the cross are 2mm. *(e)* A custom structure was also used for resistance characterisation. *(f)* The 21mm interconnect served as a resistance measurement model for the modular microwell units. *(g)* Multiple microwells connected to their respective contact pads, a structure used for testing. *(h)* Multiple microwells on a gold substrate, used for profiling and microscopy during the SU-8 layer optimisation. *(i)* A test structure intended to be used for acoustic characterisation of the individual layers.

3.2. Microfabrication

Using the facilities in the Else Kooi Laboratory (EKL) at TU Delft, the main system components were developed inside clean rooms (ISO5 and ISO7). The usage of microfabrication technology and procedures are vital for the creation and characterisation of reliable micron-scale components. Standard photolithographic methodologies and chemical process steps were used to realise gold and SU-8 patterned layers on top of a silicon wafer. The flowchart for this fabrication process can be found in Appendix E.

A 100mm diameter [1,0,0] silicon wafer served as the initial substrate. Photoresist (Shipley SPR3012) coating on top of the substrate after HDMS treatment was done using the automatic coater (EVG120). The positive photoresist was exposed to the zero-layer mask using a stepper (ASML 5500/80). Following exposure, the development (Shipley MF322) step was executed by the same automatic coater. This resulted in the negative zero-layer pattern of photoresist on the wafer, which was then dry etched into the wafer surface achieving a depth of 120nm. The remaining photoresist was then stripped of the surface using a plasma system (Tepla Ωmega 201). This left the zero-layer imprint of the alignment markers in the wafer.

After the creation of the zero-layer containing the alignment markers, the gold thin film pattern must be made to form the contact pads, microelectrode seed layer, and the tracks running between them. This was done using a lift-off process. Again similar patterning of the photoresist was achieved using the automatic coater. However, the photoresist used was different (AZ Nlof2000) and the exposure was done with a custom mask using the contact aligner (SUSS/MicroTec MA/BA8). This patterned photoresist layer was then brought to a metal evaporation system (CHA Solution Std.). Here a chromium adhesion layer of 20nm and a gold layer of 200nm were sequentially deposited on top of the patterned photoresist. Then the photoresist was chemically released from the silicon leaving its negative metal pattern. More detailed information about the lift-off process is provided in Appendix E.

Finally, the SU-8 negative photoresist layer was introduced to pattern the hydrophobic microwells and the contact pad openings. This was achieved by manual coating inside a wet bench with a fume hood. The substrate was pretreated with HDMS gas flow for 10min. The wafers were subsequently spun with SU-8 (MicroChem SU-8-2015) at 5000rpm, backside cleaned with q-tip and acetone, and then soft baked on a hotplate (contact, 100°C, 3min). The SU-8 was exposed (168mJ/cm^2, 120% relative dosage because of the partial gold substrate) using a second brightfield mask in the contact aligner and baked again (contact, 100°C, 4min). Developing was also done manually using PGMEA. After rinsing and drying, a final baking step at high temperature was performed (contact, 150°C, 10min). This yielded an $\approx 11.5\mu$m thick patterned SU-8 layer.

The parameters of spin-coating speed, exposure dose, and development time were achieved through multiple rounds of optimisation. This adaption was necessary to achieve the fully opened 10μm and 20μm diameter microwells, which were unattainable with initial recipes. The 5μm diameter microwells could not be realised due to the use of manual contact alignment and the fact that the high aspect ratio structures did not properly develop.

At this point, the wafers were diced (Disco DAD321) into their intended die sizes as shown in Figure 3.2. The total work described above was repeated in three batches. The first batch consisted of 2 wafers, the second had 3, and 6 wafers were processed in the last batch.

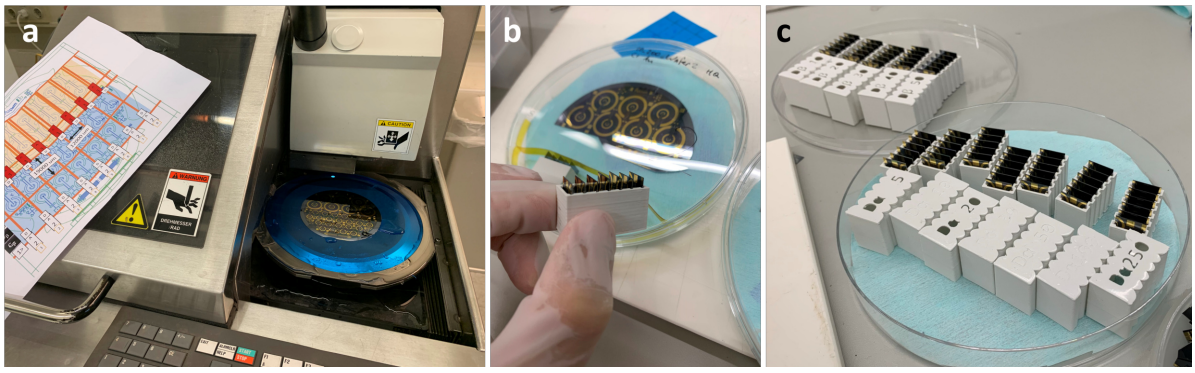

Figure 3.2: *(a)* Finished wafer on the dicer's vacuum chuck together with the dicing schematic. *(b)* Chips from a single wafer separated from dicing foil and stored in a 3D-printed PLA box. *(c)* All chips from the last batch were stored separately according to their respective microwell diameter.

3.3. Adaptive packaging

Interfacing with the produced 12 by 19mm passive die can be achieved in various ways. Conventionally, a specialised printed circuit board (PCB) is used, which can be designed or picked from a range of standard types to fit the application. The dies are mounted to the PCB and their contact pads are wired with a wire bonding system. Although the wire bonding was performed (TPT wire bonding) and a successful connection to a PCB could be achieved, in this project it was opted to use a different packaging method.

The chip's design incorporated contact pads large enough for direct interfacing with alligator clips. This allowed the die itself to be exchangeable and thus a single package could be used for multiple different chips. However, it requires careful handling of the dies during the exchange. Still, moving away from

per-die packaging and abandoning die mounting not only saved time but also allows the package to be tailored and iteratively adapted to fit the application. The convenience of adaptive packages generates most of its potential when working in the design space provided by 3D printing, allowing highly customised interfaces with the outside world. It was therefore employed as the packaging methodology in this study.

The electrical connections were formed by a soldered alligator clip. The clip had a spring-loaded jaw with a tin droplet inside. This tin droplet formed an ohmic interface with the gold contact pad on the passive chip. The clip is also shown in Figure 3.6 (h,i). This connection was characterised by DC measurements and was considered stable and reliable, as presented in Section 4.1.3.

The 3D-printed scaffolds formed the mechanical support for the chip, its alignment with other setup components, and a reservoir for electrolyte and DI water. The scaffolds were designed in 3D modelling software (Blender) with the precision modelling methodology. As opposed to CAD software (e.g., Fusion 360 or SOLIDWORKS), this software allows for faster manipulation and easy visualisation of the produced 3D objects. From Blender, the designs were converted to Standard Tessellation Language (STL) files, which could again be imported into slicing software (CURA). CURA produces gcode in their respective gcode file format, which represents the machine instructions the 3D printer needs to execute the print. These files are copied to a drive, which is inserted into the 3D printer (Ender-3 Pro, Creality 3D). Here the gcode files can be selected to start the 3D printing process. Before and during printing the machine has to be calibrated to level exactly with the polypropylene printing bed. This was achieved through manual mesh bed levelling before printing and small-scale z-stepping based on observations during the printing of the first layer, see Figure 3.3 (a). This step is essential to form proper printed parts since the temperature of the printing bed (80°) warps the bed itself as well as the printed part. The rest of the printing procedure is automatically executed by the machine based on the provided gcode. The printing of an electrodeposition test bath is shown in Figure 3.3.

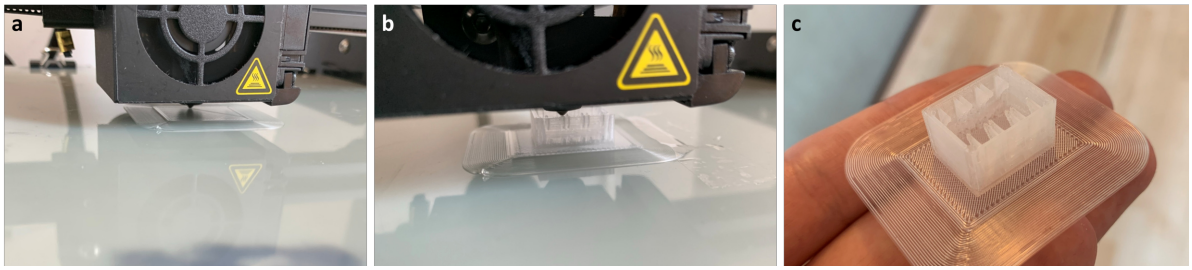

Figure 3.3: Progress of 3D-printed polypropylene scaffold for electrodeposition tests. *(a)* Printing of the initial layer, requiring supervision. *(b)* Unsupervised printing of the remaining layers. *(c)* The finished product with bed adhesion brim.

Over many iterations, this workflow was optimised to yield the most desirable result. Optimisations were done both in the 3D design, but also in the slicing settings to generate the most effective machine instructions. A vast number of total designs were made, ranging from 1 to 10 iterations for upward of 20 different designs. Every subsequent iteration had slight modifications to particular areas for better integration. Most of these only contain small alterations or eventually produced ineffective scaffolds, which are not presented in this report. Still, many productive scaffolds were produced. Each one was used for testing or employed as part of the electrodeposition setup, and the electrophysiology setup, but also for transport and handling. The selection shown in Figure 3.4 captures the most essential attributes of the scaffolds. The slicing optimisations were mostly targeted to make scaffolds watertight and reduce stringing effects. Eventually, a set of slicing settings was established, which were tailored to produce the relatively small-scale scaffolds. These settings are presented in Appendix A.1.

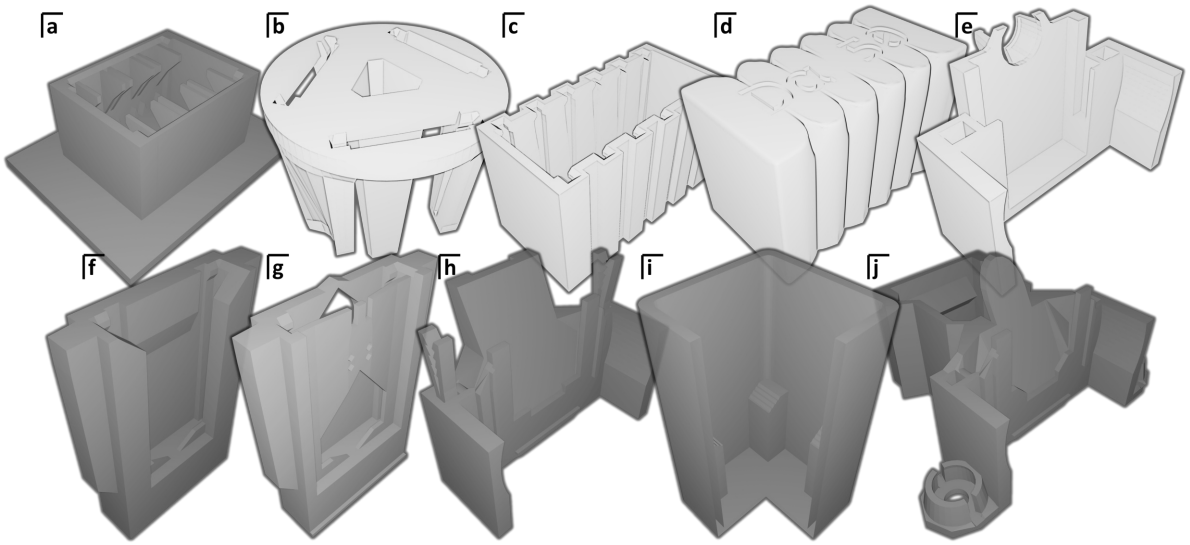

Figure 3.4: 3D scaffolds were printed and used during this thesis project. The bright white scaffolds *(b,c,d,e)* were printed using PLA, whereas the others were made from polypropylene. They are used for electrodeposition *(a,e,f,g,h)*, electrophysiology *(h,j)* , transport *(c,d)*, testing *(e,i,j)*, and cleaning *(b)*.

Two thermoplastic filament materials were selected for the creation of the scaffolds. Polylactic acid (PLA) filament was used to print rigid parts, while polypropylene (PP) was used to print detailed flexible parts that required chemical and electrical resistance [60]. Especially for the electrodeposition scaffolds, the use of PP is essential, since it was tested and found to be chemically resistant to ammonia, whereas PLA is not (see Appendix A.2).

3.4. Electrodeposition of silver on recessed gold microelectrodes

Since many factors influence the deposition obtained during an electrodeposition process, it was chosen to stick to a single established procedure found in literature. Therefore, the work here is done largely according to the methodology of Polk et al.[61], since their process matched well with the current design. Silver deposits were formed on the electrode at the bottom of the microwell and later chlorinated. The authors lay out the electrodeposition procedure required to form reliable Ag/AgCl electrodes on top of an gold seed layer. The procedure was adapted to a two-electrode setup to reduce the number of components required. The steps involved are shortly discussed below.

Over many trials, it became clear that the procedure used was not optimal for deposition. Both the size of the openings and SU-8's hydrophobic surface are thought to be responsible. Different durations and intensities of oxidative pre-treatment, anode conditioning, and electrodeposition were attempted. This was done for each of the openings in the SU-8 mask ranging from 10 to 250 micron. The results of this investigation are shown separately in Section 4.2.2. The conclusions to these intermediary results emphasized the need for a wetting step and a current amplitude correction due to the voltage dependency of electrochemical reactions. These results were based on observations done with a pocket microscope (Carson MicroFlip 250x) which was integrated into the electrodeposition setup by using 3D-printed scaffolds. The microscope was aligned to a mobile phone camera for viewing. This was done to allow direct and real-time observation of the electrodeposition process.

The camera setup showed the need for an additional ethanol washing step, as parts of the microwell were not reproducibly wetted. The image capturing the remaining air bubble in a microwell and its removal with the ethanol wash is shown in Figure 3.5. A second adaption was made to the current amplitude to achieve a specific local voltage and was also characterised by the camera setup. This could be done because of the high reflectivity of the deposited polycrystalline silver, as shown in Figure 3.5 and Figure 3.6. Combining the read-out current with empirical confirmation of deposition yielded a methodology with a much higher success rate as described in Section 4.2.2. A photo of the deposited silver in the microwell can also be seen in Figure 3.5.

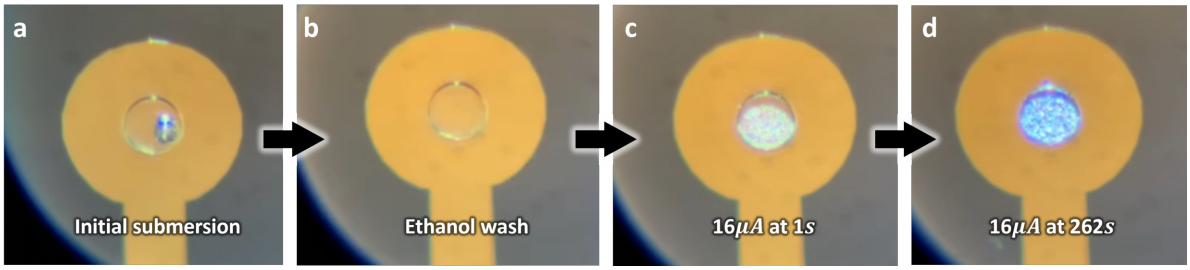

Figure 3.5: The electrodeposition is shown for a 50μm diameter microwell. *(a,b)* The importance of the ethanol washing step to remove air bubbles before electrodeposition. *(c,d)* Photos of the silver deposits 1s and 262s after initiation of 16μA current.

These realisations led to an improved setup. Here chips were placed inside a replaceable 3D-printed PP scaffold. They were then clamped to achieve an electrical connection to the gold seed layer. The clamp used was a filed-down alligator clip with a tiny drop of solder (60/40 lead/tin) in the clamp jaw to ensure the needed removable ohmic contact to the gold contact pad. This connection was extensively tested and deemed reliable. A silver sheet (8x20mm, 0.5mm thick) was cut to allow a viewing window and soldered to a tungsten wire (99.95%, 0.05mm ⌀, annealed). The plate was inserted into the same PP scaffold, 0.5-1mm parallel to the chip. This scaffold was glued (EPOTEK 301-2f, two-part epoxy) to a glass coverslip (Bresser, 18x18x0.17mm), which created the transparent viewing window for microscopy during electrodeposition. The coverslip and scaffold created a reservoir ($\approx 300\text{mm}^3$) opened only from the top to form the electrolyte bath. Subtracting the volume of the chip and silver sheet, the resulting volume amounted to approximately 200mm^3 or 200μL, which was filled with the electrodeposition solution. The microliter volume could be inserted using a mechanical micropipette (Europhysica, 20-200μL). A mobile camera (iPhone XR, 12Mp, 26mm, HD 30fps) recorded the deposition through the pocket microscope. The microscope was aligned by snapping it into a 3D-printed PLA attachment in which the PP reservoir could be mounted. This allowed for monitoring of silver deposit on top of the gold seed layer during electrodeposition. Observing the deposition in real time also made it possible to apply a high current density and manually stop the process once the silver deposition is registered.

Before the assembly of all components, the electrodeposition solution was prepared. The electrolyte was formed out of 0.3M $AgNO_3$ dissolved in 1M NH_3(aq). The dissolved aqueous ammonia concentration was made by diluting 28% NH_3(aq) with DI (1mL:15mL). Then the 815mg of $AgNO_3$ powder was added to form the electrodeposition solution. The reservoir scaffold was cleaned and then dried using a nitrogen gas stream before filling it with the solution. For the chips, the patterned SU-8 served as the mask for the electrodeposited silver on the gold seed layer. Also, the chips were extensively cleaned to avoid contaminations on this seed layer. This was done through ultrasonication in baths of firstly IPA and secondly HCl, with a DI-water rinse after each step. The silver sheet anode was sanded, rinsed, and subsequently conditioned on a larger silver surface inside the reservoir. After these steps, the solution was rinsed out and a fresh solution was used for electrodeposition. Any air bubbles that remained in the microwell were mitigated by using the low surface tension of ethanol. The ethanol was pipetted in small volumes ($< 10\mu$L) on the microwell and washed out with DI-water, moments before insertion. Then an electrochemical cell was formed by the silver sheet anode, the electrodeposition solution as the electrolyte, and the recessed gold electrode as the cathode. The enlarged schematic of the 3D-printed PP scaffold with the inserted components is shown next to its photos in Figure 3.6.

The electric control of the deposition was carried out by a SourceMeter (Keithley 6430, Sub-Femtoamp Remote SourceMeter) with its pre-amplifier. This device was chosen because of its real-time control capability of the supplied current. The high and the low input-output were connected to the anode and cathode, respectively, as shown in Figure 3.6. The operation could be controlled programmatically through the use of a digital I/O port (GPIB to IEEE-488) from a laptop through SCPI commands. The commands are sent using a Python serial port module (pyvisa). This allowed for easy data saving and device configuration. The device allowed for 2500 data points (measured voltage, current and impedance) to be saved during a linear sweep of applied current. Code for this operation is shown in Appendix D.3. Although the current magnitude differed throughout optimisation, a current of 16μA was deemed most successful for all microwells with diameters $10 - 100\mu$m.

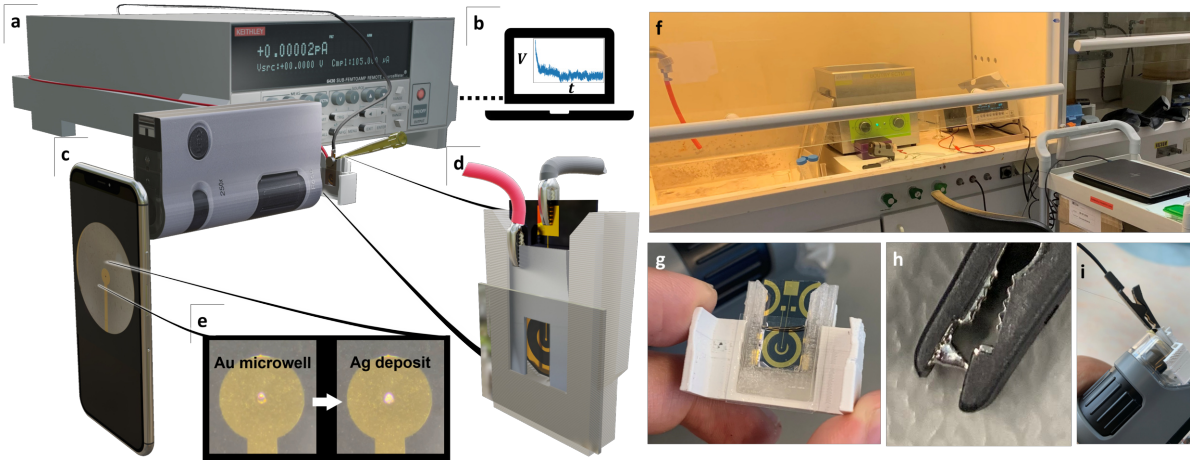

Figure 3.6: Schematic of the electrodeposition setup used, with an enlarged view of the PP scaffold bath with chip and silver sheet anode. *(a)* The Keithley 6430 SourceMeter used for current control and electrical measurment. *(b)* The SourceMeter was connected to a laptop to monitor the voltage during deposition and record the data. *(c)* An iPhone connected to a pocket microscope (Carson Microflip 250x) was interfaced with the PLA holder to visually confirm silver deposition and to see potential remaining air bubbles in the microwells. *(d)* The chip and the silver sheet inside the electrolyte reservoir scaffold. The red cable represents the connection from the silver sheet anode to the Sourcemeter, and the black cable represents the alligator clip that interfaces with the cathode chip's contact pad. *(e)* Images of the microwell captured before and after electrodeposition. The silver deposit has a high reflectivity. *(f)* Photo of the setup inside the fume hood. *(g)* Photo of the reservoir scaffold with the chip inside, it is filled with DI water. The reservoir is inserted into the PLA holder. *(h)* The alligator clip with solder tip inside used for interfacing with the chips. *(i)* The assembly of the pocket microscope, PLA holder, PP scaffold, chip, aligator clip and silver sheet.

For the last batch, height profiles were constructed in order to accurately estimate the deposited silver thickness. After and before electrodeposition the microwells were profiled using a profilometer (DEKTAK 150). The probe tip with a 12.5μm radius was applied with a force of 3mg over a length of 600μm in 20s and with a vertical range of 65.5μm (depressions).

Additionally, to get a better understanding of the deposition profile a scanning electron microscopy (SEM) image was made using a state-of-the-art SEM system (Hitachi Regulus 8230). A 50μm chip was diced at the edge of its microwell after silver electrodeposition. The deposit in the microwell was subsequently imaged from several angles using the SEM settings described in Appendix A.3.

Chlorination of the electrodes was achieved by exposing the silver to 50mM of $FeCl_3$ dissolved in DI for 50s. An ethanol-washing step was always executed before chlorination.

With this setup it was also investigated whether the deposition was reversible, removing the deposited silver. This would also indicate whether the gold electrodes could be electrochemically polished prior to electrodeposition. This was achieved with the same setup but by reversing the polarity, essentially swapping the anode and cathode. This produced non-reproducible results and was therefore not employed for the subsequent chip batches.

3.5. Ultrasound characterisation

The acoustic pressure and intensity at the surface of a silicon wafer were characterised before the design and fabrication of the device to reveal which intensity of US would pass through a chip. Experimental results and in-situ acoustic simulations were employed to best determine the acoustic signal in the focal region.

3.5.1. Simulation in K-wave

All acoustic simulation was done in MATLAB K-wave [37]. The specified pressure variations propagated from a single boundary through the specified media (water or silicon). The modelled pressure variations followed a sinusoidal curve with a frequency of f = 9MHz with an amplitude of precisely 360kPa to achieve a reference focal intensity of P_{SPTP} = 100kPa. The spatial discretisation was 50μm on a 10x1mm^2 grid, surrounded by a perfect matching layer. Time steps of 0.5ns provided sufficient temporal resolution, and the total simulation duration was 10μs. Although the raw temporal data was recorded,

most profiles were calculated using time and space clipping values to decrease the computational cost of simulation. This spatial clipping removes the area before the second silicon interface, and the temporal clip removes simulation before 0.3μs. The results of such a simulation pair are shown in Figure 4.9. The MATLAB code is also attached in Appendix D.1.

3.5.2. Ultrasound integration

A 2.8x2.8mm^2 PZT transducer was diced from a sheet (PZT-5H, PIEZO.com) and served as the acoustic signal source. The PZT ground connection was formed by either conductive epoxy (GENTEC EPOTEK H20E) or by pressing it on conductive tape (ARclad 9032-70, Adhesives Research). With either of these, it adhered to a brass plate of 18x25mm^2. This plate was clamped by an alligator clip with an outgoing cable to the ground connection of the function generator. A tungsten wire (99.95%, 0.05mm $\varnothing$, annealed) was glued with a conductive epoxy to the top of the PZT, used to drive the 20V signal. The epoxy was cured on a hotplate (Thermo Scientific SP88857107) at 80°C.

3.5.3. Ultrasound measurement

With the acoustic source in place and connected to a function generator (RIGOL DG4202), the receiving measurement setup was established. A 3-axis positioning system (Gampt, VK-62100) moved a needle hydrophone (1mm, 1.35mV/Pa @ f = 8MHz, Precision Acoustics, NH1000) in an indicated line, plane or volume. Its preamplified electric signal (Precision Acoustics) was monitored by the oscilloscope (InfiniiVision, DSO-X 3032A), which was triggered with a second signal from the function generator. The positioning system, oscilloscope and function generator were operated via custom MATLAB software (Experimental Visual Acoustics, Burghoorn[62]). This allowed for the measurement of acoustic profiles at different locations, and for specified acoustic parameters (e.g., frequency, burst number, and voltage). The data points in the automatically generated plots represent the maximum peak-to-peak pressure measured. Photos of the setup and the software are shown in Figure 3.7.

The acoustic signal was a V = 20V sinusoidal burst consisting of 20 oscillations. The time range of the measured trace was triggered 3μs after driving the acoustic signal to prevent EMI pickup during measurement. Each trace consisted of 16000 voltage values, each averaged over 16 separate estimations. These average voltages could directly be converted to pressure observations using the frequency-dependent hydrophone sensitivity. From here the maximum peak-to-peak pressure was calculated by subtracting the minimum from the maximum pressure. This value was representative of the temporal peak acoustic intensity.

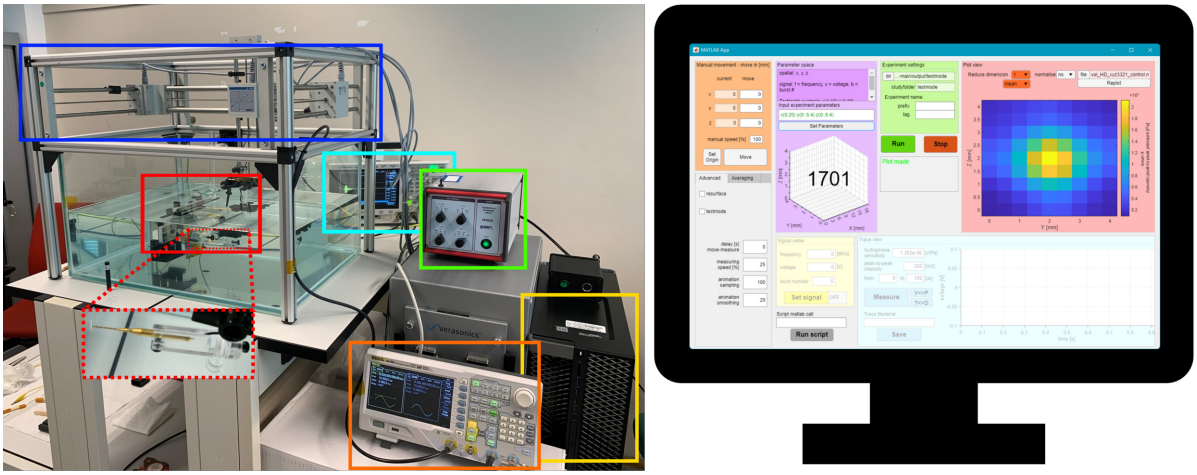

Figure 3.7: The acoustic characterisation setup. (Dark blue, top left) 3-axis positioning system; (Red, centre left) the immersed elements: hydrophone (+ zoom-in), and holders; (Light blue, top middle) oscilloscope; (Green, centre right) control unit; (Orange, bottom middle) signal generator; (Yellow, bottom right) PC.

During the initial design stages of the platform, measurements of the acoustic losses due to the silicon interfaces were measured. This was done before the platform design because the ability to generate sufficient acoustic intensity would be crucial during the investigation of the formulated research question.

These investigations were done in the experimental setup with two conditions. In the first, the PZT transducer intensity profile was measured, which served as the reference. Then the second measurement is done to establish the profile at the same location after the PZT's acoustic signal had passed through a silicon wafer.

Later, when acoustically characterising the scaffolds used for the electrophysiological setup, a similar approach was adopted. However, the measurement of the final setup was always preceded by two reference measurements. The first reference characterised the signal from the PZT on brass in DI without any obstruction. The brass plate was then inserted into the scaffold, which aligned to the location of the chip's microwell. Before inserting the chip itself, the scaffold with PZT was submerged in DI water and acoustically characterised as a second reference measurement. Finally, a chip was inserted and the actual acoustic intensity to which the microwell was subjected could be measured. The reference measurements were used to infer the acoustic losses caused by each component and were compared to earlier estimations for validation.

3.6. Electrophysiology

Measuring the electrical properties of the BLM could be done through multiple electrochemical measurements. The measurements were instrumental in the determination of the actual presence of a membrane.

Each electrophysiological measurement requires distinct experimental conditions and is dependent on different electrical parameters for driving, signal amplification and filtering. Still, a generalised mode of operation can be described. Firstly, the measurement front end which consists of a physical setup with different electrodes submerged in an electrolyte reservoir. The chip's microwell was the Ag/AgCl WE, which was washed with ethanol before submersion. The CE and REF electrodes were also found in the same electrolyte to close the current pathway and provide the reference voltage, respectively. The chip's contact pad and the backside of the CE and REF were clamped and wired to a potentiostat. The use of a dedicated potentiostat for electrochemical measurement (Autolab Metrohm PGSTAT302N) with its accompanying software (NOVA 2.1), made it easy to switch between measurement modes and select the independent variable ranges corresponding to the conditions of interest. Since the software did not allow for easy comparison of multiple measurements, the results were directly exported and automatically processed by custom Python software, which is shown in Appendix D.2.

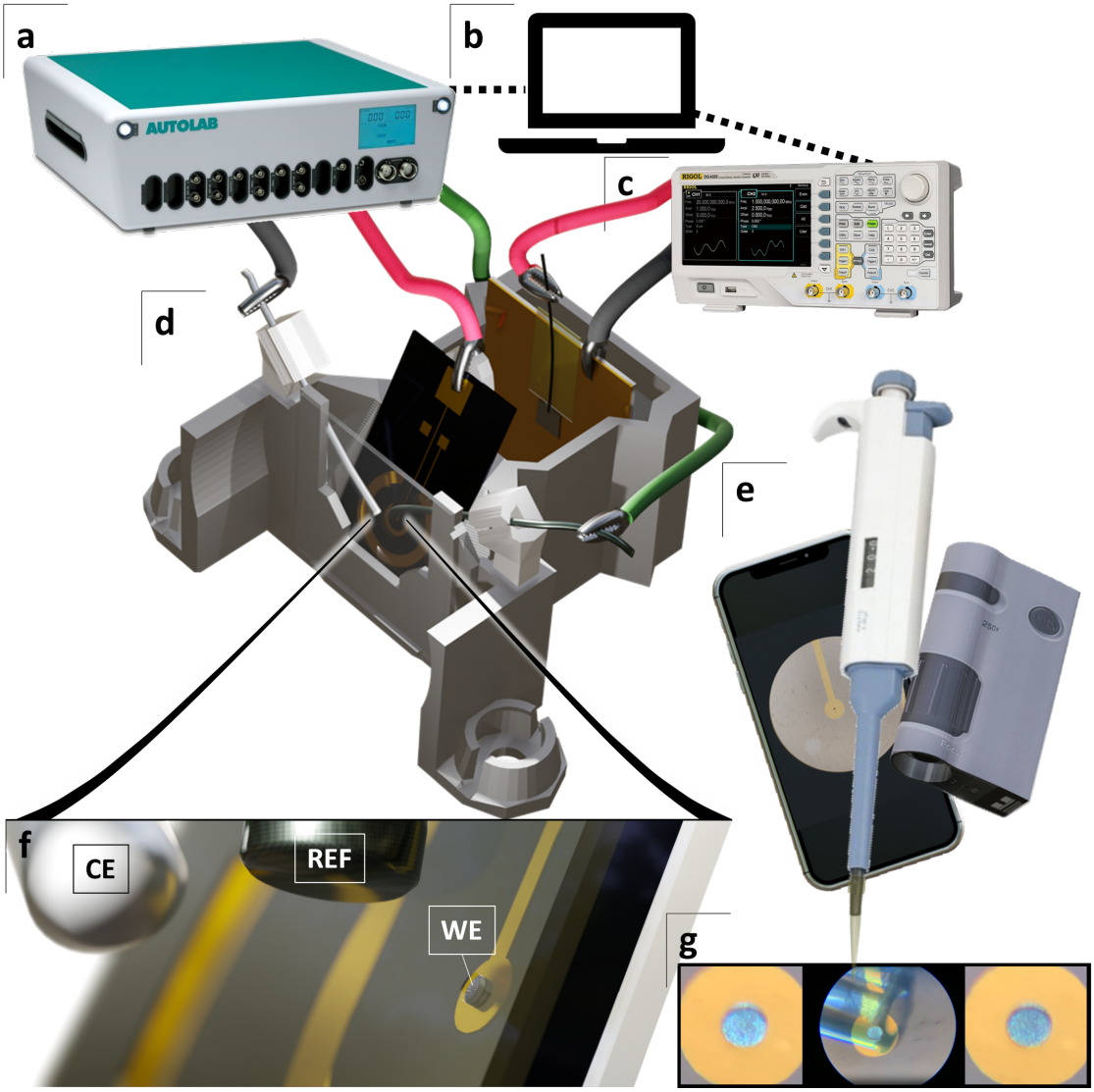

Figure 3.8: Figure showing the setup used for electrophysiological measurement. The chip's microwell served as the WE *(Left red cable)*. This connection together with the Ag/AgCl REF *(Green cable)* and the Pt CE *(Left black cable)* are connected to the potentiostat. The other connections *(Left red and black cable)* drive the acoustic source to produce ultrasound. The components in this figure are to scale, however, only relative to elements within their respective subfigure. *(a)* The Autolab potentiostat PGSTAT302N is used for voltage control and signal filtering and amplification. *(b)* Laptop to control the potentiostat and process its data. It is also used to control the function generator. *(c)* The RIGOL DG4202 function generator is used to drive the acoustic source. *(d)* The 3D-printed scaffold with a glass slide forms a reservoir for the electrolyte. PLA pinholes direct the REF and CE to the microwell's WE on the passive chip. The electrolyte reservoir is separated from the second reservoir with an epoxy film behind the chip (see f). The acoustic source produces its acoustic signal in the second reservoir, which is aligned to the backside of the microwell as shown in Figure 3.9 (c). *(e)* The iPhone and pocket microscope are used for image recording. The mechanical pipette and its pipette tip are used for painting the membrane. *(f)* A close-up schematic of the three-electrode configuration shown in (d). *(g)* Photos of the membrane painting process. From left to right: microwell without membrane, pipette near the microwell, microwell with membrane.

The discussed experimental front end was supported by a scaffold similar to the one used for electrodeposition. Also here a glass coverslip created a viewing window for microscopy during electrophysiology. The electrolyte used consisted of 1M KCl buffered with 20mM Tris (pH of ≈ 7) dissolved in DI water. This electrolyte was contained in the primary scaffold chamber, which was separated from a second chamber with pure DI by a thin epoxy (EPOTEK 301-2f, two-part epoxy) film. The second chamber was used to support the acoustic source, which was purposefully separated from the microwell electrode to limit electromagnetic interference (EMI). This is illustrated in Figure 3.9 (a,c). In the case of a two-electrode

setup, a single Ag/AgCl wire was used as the REF and CE. The electrode could easily be fabricated from a pure silver wire (99.9%, 1mm ⌀, Europhysica) and was dipped for 50s in household bleach (Glorix), which contains sodium hypochlorite (4.5% active chloride). This same electrode was also used in a three-electrode setup as the REF, whereas the CE was represented by a platinum (Pt) wire (99.95%, 0.5mm ⌀, BASi). The REF and CE electrodes were physically supported by 3D-printed PLA pinholes that could be inserted into the PP scaffold. To make sure the scaffold did not shift during assembly, small Neodymium magnets were attached to the sides of the scaffold fixing it in place. The electrochemical pathways transporting the current signal for the two- and three-electrode setup are shown in Figure 3.9 (b) and Figure 3.9 (c), respectively.

EIS measurements were done on the bare gold electrodes to validate the formation of a conductive path between the components. Specifically, the response in the high-frequency part of the spectrum was investigated, since these are of interest in future implementation. Also, these tests would confirm the relationship between area-dependent charge storage and different diameter microwells. The two-electrode setup could be employed since the faradaic current was negligible for the polarisable gold electrodes. A 10mV sinusoidal signal was applied over the voltage measured at the Ag/AgCl wire REF. The signal was swept in the frequency domain from 1Hz to 1MHz, which was, unfortunately, the upper limit of the potentiostat. Measurements of 10 points per decade were done in this range.

The resulting traces of these measurements can then be fitted to an electrical equivalent circuit model by standard mathematical optimisation. The precise optimisation method is outside the scope of this work but requires the number of circuit components, the kind of components, and their initial values to estimate the component values. These circuit components and their values represent the electrochemical mechanism and its magnitude, respectively. The model employed for this fit consisted of a resistance in series with multiple parallel resistor-constant phase element[1](CPE) pairs. Since the obtained results could not be fully processed these fits are not presented in this work.

After several setup trials, a procedure was found to obtain accurate membrane measurements. This required the use of a three-electrode setup while establishing the membrane and switching to a two-electrode setup when a membrane seal was created. The three-electrode setup was used because a separate CE enables the REF to stably measure voltage without being subject to high faradaic current. However, using the single CE/REF in the two-electrode setup mitigated the small signal low-frequency oscillations that were observed. These oscillations were possibly caused by WE to REF feedback. A more detailed discussion of this phenomenon requires interpretation of measured results and is found in Section 4.4.2.

[1] The constant phase element (CPE) is a component that can be incorporated into an electrical equivalent circuit model that fits electrochemical observations. The CPE can be conceptualised as an imperfect capacitor that has a phase angle smaller than 90°. Equivalently, it could be thought of as a resistor with a phase delay. There is a multitude of electrochemical dynamics that can be responsible for such behaviour [63].

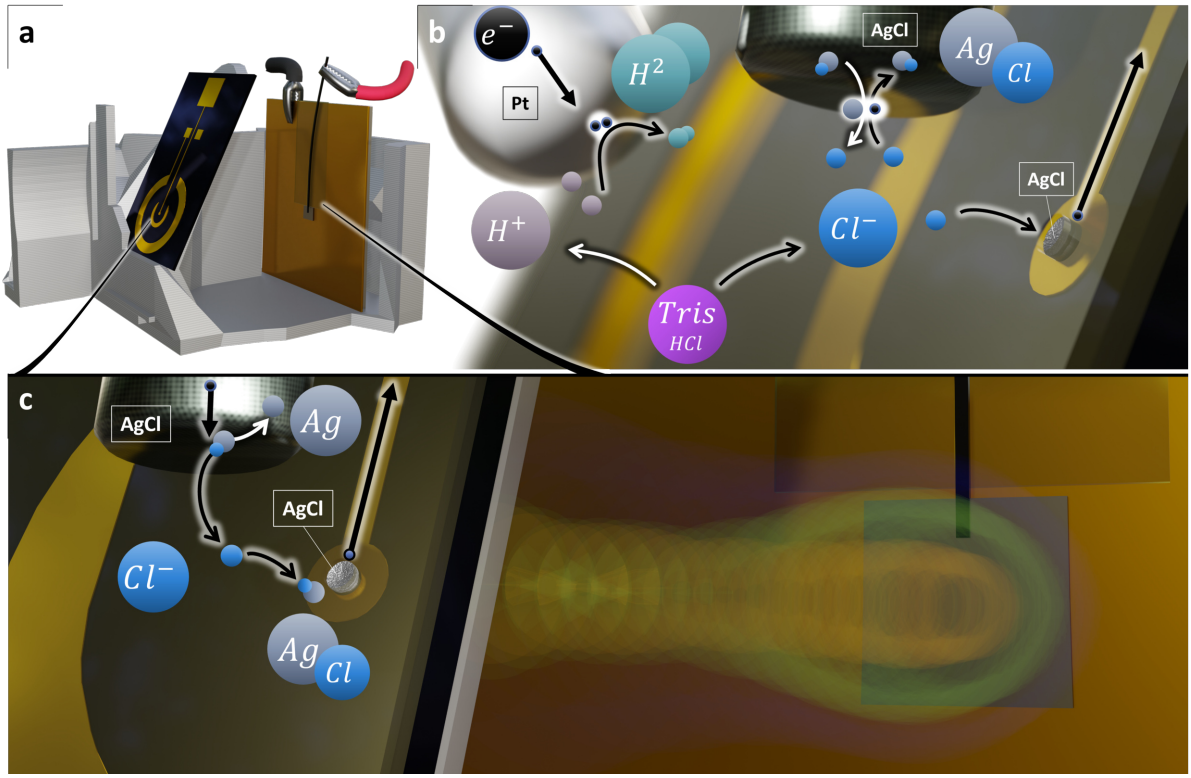

Figure 3.9: The chemical interactions during electrophysiological measurement. The white and black arrows indicate the opposing current and electron flow direction, respectively. The schematic shows the set of reactions that ideally occur when a small positive voltage is applied at the WE. *(a)* A crossection of the electrophysiology scaffold with the chip and acoustic source inserted into their respective reservoirs. *(b)* Three-electrode setup, used when no membrane is present to prevent fast degradation of Ag/AgCl REF. There should be approximately zero net current going through the REF. The buffer keeps pH constant and indirectly allows for the transfer of negative charge from the Pt CE to Ag/AgCl WE. *(c)* Two-electrode setup, used when a membrane is present to mitigate the small signal feedback between the WE and REF. The REF here also serves as CE and therefore will slowly deplete its silver chloride layer to silver upon the arrival of electrons. On the WE the Cl^- ions consume the remaining silver to form silver chloride leaving an electron in its wake. The right side of this figure shows the acoustic signal that arrives at the backside of the substrate, as is the case in the electrophysiological setup in Figure 3.8.

Using CA with 0.2V applied at the WE, the current was measured for several minutes (2-40). Experiments were lengthy in order to involve the steps needed for:

1. ensuring a conductive path (wetted microwell)
2. waiting for stabilisation of the current
3. establishing a suspended BLM
4. switching to a two-electrode setup
5. measuring a reference current
6. measuring current again during acoustic stimulation
7. measuring a second reference

However, steps 1-4 may be skipped when a membrane was still in place from the measurement before. Due to project time constraints, acoustic stimulation of the BLM was only not fully characterised, having only a handful of unsystematic measurements. Still, during this project, a vast amount of data was generated. The produced CA traces were primarily analysed qualitatively since the acquisition of accurate absolute values required a lengthy equilibration step of the electrodes. Still, suspension of the BLM was the most time-consuming since it had to be achieved manually. This is described in the next section with photos from the microscope setup.

3.7. Lipid preparation and suspension

The suspension of a BML had to be done manually. The methodology used for BLM suspension is that of Braun et al.[64] and Hartel et al.[28]. Before the actual lipid suspension, however, many preparations were required to get the biomolecules in proper condition for handling. The lipids had to be aliquoted, dried and resuspended, and the steps taken for this are briefly described in this section.

3.7.1. Lipid preparation

Lipids were ordered through Avanti Polar Lipids (200mg, DPhPC 1,2-diphytanoyl-sn-glycero-3-phosphocholine) and were delivered dissolved in chloroform inside two 4mL ampules. The ampules were stored at −20°C. One of the ampules was later used to make the 12 aliquots. These aliquots needed to be prepared inside a fume hood, since chloroform is very volatile and should not be inhaled. In preparation for this, a glass syringe was soaked in acetone, dried, and cleaned trice with chloroform (HPLC > 99.8%, amylene stabilized). When the ampule was at room temperature, 200μL of the solution was extracted with the syringe and put into a small glass vial. Then a steady stream of nitrogen gas was blown into the vial while rotating. This evaporated the chloroform and precipitated the lipid biomolecules on the inside of the glass vial. The vial was placed in a desiccator under a vacuum to get rid of the remaining chloroform. After this step, the lipids could be redissolved into the non-polar solution, n-Decane (99%, for synthesis). 200μL of this solution was then found in each vial, achieving the same 25mg/mL of lipid concentration. After screwing on the PTFE cap and redisolving all the lipids, the vial is wrapped in Parafilm and Kapton tape and can be stored at −20°C until its use.

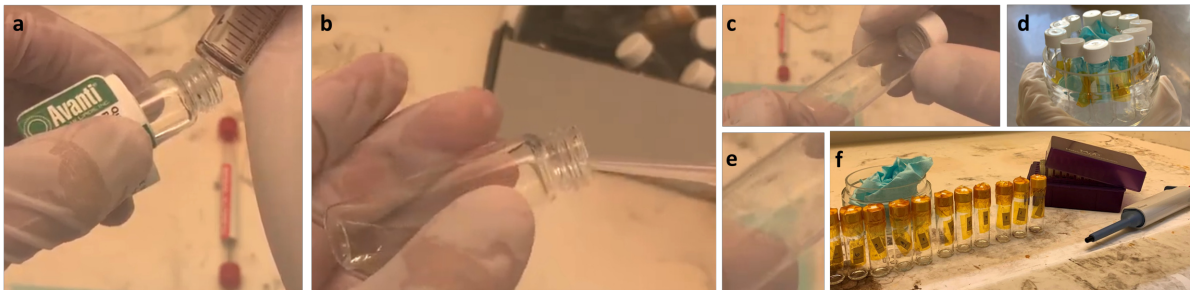

Figure 3.10: The photos that were taken during the preparation of the lipids. *(a)* Using the glass syringe 200μL of lipids suspended in chloroform is extracted and transferred to a separate vial. *(b)* The chloroform is slowly evaporated under a fume hood by using a low-pressure nitrogen stream connected to a pipette tip (right) while rolling the vial slowly up and down between the fingers. *(e)* The precipitated lipids in a glass vial with the screw PTFE cap. *(d)* The series of aliquots that are brought to the desiccator. *(e)* A close-up of the precipitated lipids in a glass vial wall. *(f)* The aliquots in the vials are wrapped in Parafilm and Kapton tape to prevent hydration and can be stored at −20°C.

3.7.2. Membrane suspension

When all measurement setup components were made ready, a vial was taken from the freezer for use. The non-polar solution with the lipids would quickly reach room temperature, and could then be opened. Dipping a clean pipette tip into the vial's liquid without pipetting provides enough biomolecules to suspend a complete BLM. The dipped pipette tip was submerged and brought into proximity to the microwell, at a slight angle. Here a 0.5 – 1μL volume air bubble is created by using the mechanical pipette. The air bubble would arrange the lipids on its surface because of electrostatic interactions of the polar and non-polar molecular groups. The air bubble is dragged over the microwell's cavity to deposit some lipids, a technique also referred to as 'painting the membrane'. The same electrostatic interactions will allow the lipids to self-assemble into a double layer over the microwell after binding to the hydrophobic SU-8 layer edges. See Figure 3.11 for a visual representation of this process.

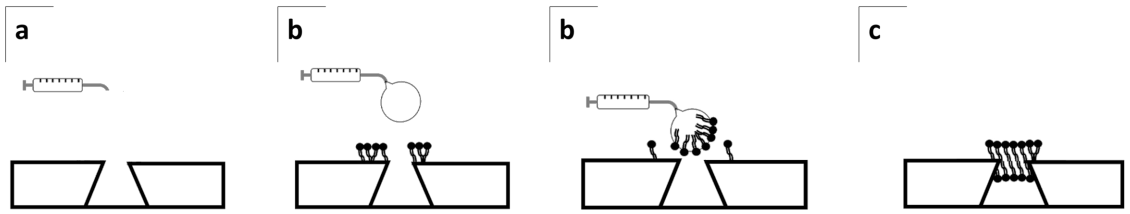

Figure 3.11: The membrane painting procedure on a microwell schematically, adapted from Braun et al.[64]. Not to scale. *(a)* Lipids can be brought in proximity to the hydrophobic SU-8 walls of the microwell with an air bubble. Here they will anchor their hydrophobic tail towards the material. *(b)* Lipids can be brought in proximity to the hydrophobic SU-8 walls of the microwell with an air bubble. Here they will anchor their hydrophobic tail towards the material. *(b)* Dragging the air bubble over the microwell will allow the lipids to span over the top and create the membrane. *(c)* A bilayer seal is created and will remain stable for some time.

It is essential that the microwell is properly wetted before attempting the suspension since any remaining gas inside the microwell will interfere with the bilayer formation, but also with the electrochemical measurement. Therefore, using an ethanol wash before the submersion of the microwell into the electrolyte is crucial.

The painting technique can require many attempts and does not produce an ideal membrane every time [64]. Moreover, since the membrane is hard to register visually, its formation is better observed by running a CA measurement while painting. Once a membrane has formed, the current will dramatically drop, since the membrane forms a high impedance seal for the WE on top of the microwell. The painting technique was also monitored using the handheld microscopy setup, photos of this can be seen in Figure 4.16. Since the stability of the membrane is usually only a few minutes [64], the membrane may have to be painted multiple times during a single experiment.

4

Results

This chapter presents the results and is subdivided into sections. The first section describes the microfabricated passive chips produced and the process optimisations done. Then all silver deposit characteristics are compiled into the electrodeposition section. Afterwards, the predicted acoustic intensities are compared with the in-situ derived and experimentally measured acoustic profiles. Lastly, electrophysiological validation of the gold microwell electrodes is followed up by CA measurements of suspended BMLs on Ag/AgCl microwell electrodes.

4.1. Passive chips

The designed passive chips were fabricated in three batches. During the first batch, gold deposition was optimised as well as the SU-8 height. The second batch also targeted optimisation of the SU-8 layer and achieving proper development to make sure the electrodes were fully opened. Later, the gold track resistances were characterised with help of the patterned gold structures.

4.1.1. Gold evaporation

Gold was evaporated on top of the wafer and patterned with the lift-off methodology using Nlof photoresist. The gold layer thickness was characterised by a sensor within the chemical evaporation system during deposition. Resistance measurements would later prove the thickness of the gold layer corresponded with the sensor's indicated thickness. Initial lift-off trials on the first batch showed satisfactory overall patterning. However, regions with high densities of gold flakes seemed to have redeposited on the gold surface during the lift-off process. This was solved in the subsequent batches by doing an additional sonication cleaning step in 80°C DI water for 5min directly after lift-off. No gold flakes were observed in these batches. An overview of the observations and ultrasonication is shown in Figure 4.1.

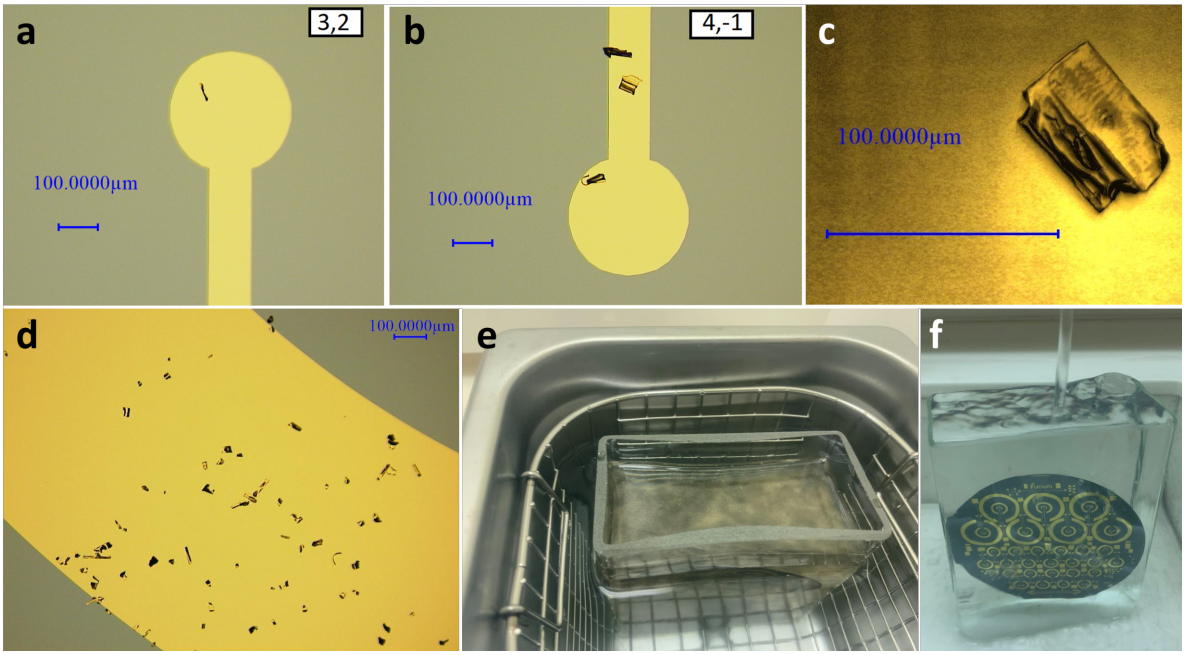

Figure 4.1: Photos of gold flake redeposition on the gold evaporated surfaces after lift-off and the ultrasonication process. *(a)* An gold electrode tip with a single gold flake on its surface. *(b)* An gold electrode tip with multiple gold flakes on its surface. *(c)* Zoom-in image of a single gold flake. *(d)* The outer gold ring with many redeposited gold flakes. *(e)* A first batch wafer in an NMP bath undergoing ultrasonication. *(f)* A first batch wafer being rinsed in DI water after undergoing ultrasonic cleaning.

4.1.2. SU-8 profiles

The first and second batches of wafers were utilised for SU-8 layer thickness and development optimisation, respectively. The recipe was constructed as specified in SU-8-2015 datasheet [65]. However, the spin speed was altered to the maximum possible value of 5000rpm, which allowed the desired smaller SU-8 thickness, which was $\approx 11.5\mu$m. Although extensive tests were done, some thickness variation between different regions of the wafer remained. Edge beads were thought to be responsible for this variation.

The exposure dose and development time of the SU-8 layer could also be found in the same datasheet. However, the exposure dose had to be corrected (1.5x relative dosage) due to the gold substrate, which has a different reflectivity than the standard value that is based on silicon. Still, due to overexposure smaller openings were left undeveloped. The relative dosage chosen was finally left at 1x and the development time was taken 1min longer than indicated on the datasheet. Results of this process are shown in Figure 4.2. With these optimisations, successful openings were achieved for all microwells with diameters $\geq 10\mu$m in the third fabricated batch.

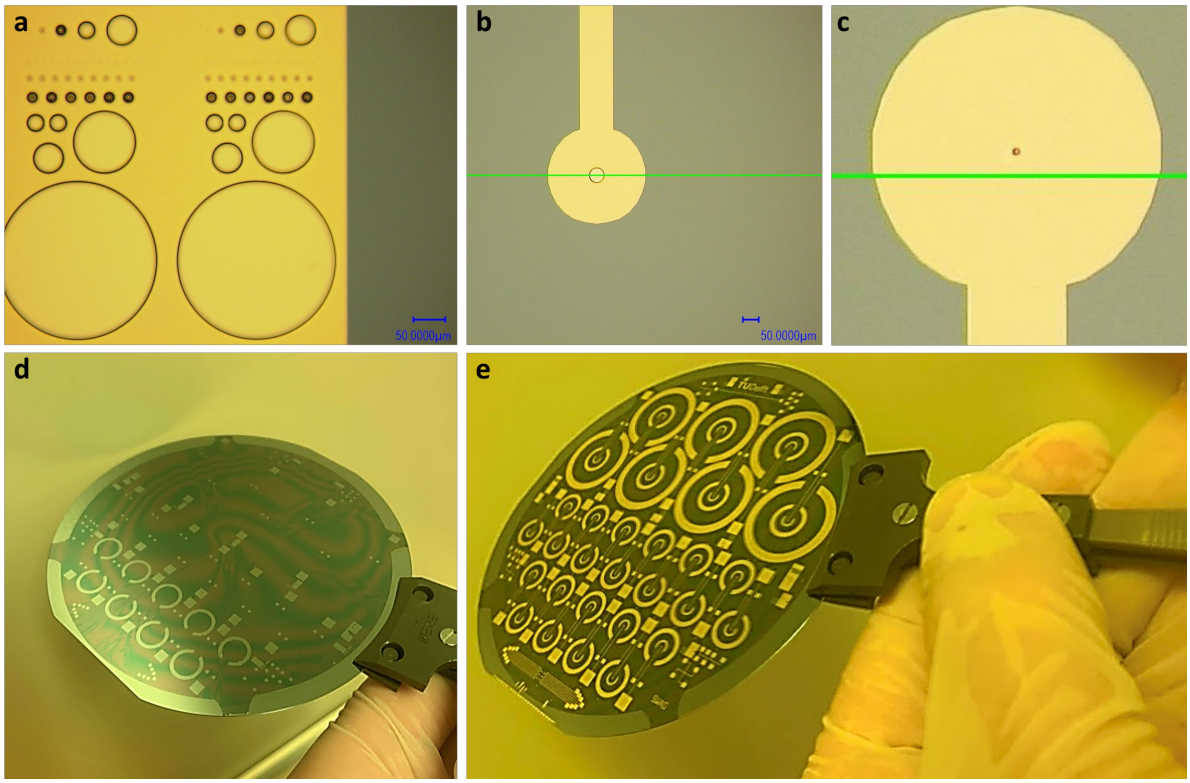

Figure 4.2: The different SU-8 patterning results. *(a)* The test microwell pattern shows undeveloped microwells for diameters < 30μm. *(b)* A 50μm diameter microwell from the third fabricated batch fully opened. *(c)* A 5μm microwell from the third fabricated batch which was not fully opened. *(d)* The SU-8 patterned layer on a first batch wafer for thickness optimisation. *(e)* A third batch wafer with the gold and SU-8 pattern.

4.1.3. Track resistance

The resistance of the tracks was tested using the clamping method and a multimeter. The resistance values and distances of all pad-to-pad paths of the 7 contact pad test structure are presented in Table 4.1. Measurement of the structures in Figure 3.1 (d,f) was also done for validation. For the van der Pauw cross an average resistance of 8.6Ω was measured, whereas the long line had a resistance of 29.3Ω. Dividing these values by their track lengths of 6 and 21mm and multiplying with the track area, yields the specific resistances of 29.7 and 28.0pΩm, respectively. The specific resistances are also compiled for the 7 contact pad test structure, their results are shown in Figure 4.3. Their mean specific resistance is 28.8pΩm. All these values are slightly higher than the specific resistance of 24pΩm found in databases [66]. The resistance test structures are found several times distributed over the final wafer layout, as can be seen in Figure 3.1.

Table 4.1: Resistance in Ω at DC of the 7 contact pad test structure. The indices correspond to those found in Figure 4.3.

	1	2	3	4	5	6	7
1	-	4.3	7.0	1.8	3.6	5.6	8.8
2	-	-	4.3	4.3	2.3	3.0	6.2
3	-	-	-	6.9	5.0	3.0	3.6
4	-	-	-	-	3.7	5.6	4.7
5	-	-	-	-	-	3.6	6.9
6	-	-	-	-	-	-	5.0
7	-	-	-	-	-	-	-

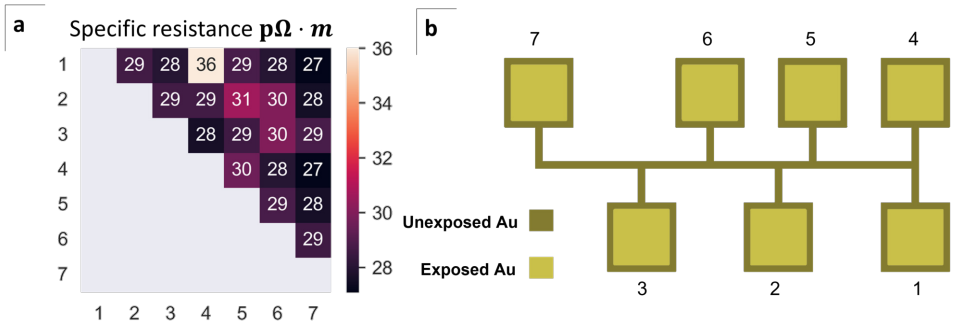

Figure 4.3: *(a)* The table of the specific resistance values corresponding to the measurements done on the presented resistance test structures. The column and row indices represent the pair of pads tested. *(b)* The 7 contact pads in test structure the contact pad denotations to the corresponding specific resistances in (a).

4.2. Electrodeposits

The electrodeposition process was the most time-consuming step in the fabrication of the passive chip. This can mainly be attributed to the labour-intensive process and the needed optimisation of the complete procedure. An effort was made to gather as much local expertise in the respective field, still, the practised procedure was primarily based on the elementary knowledge available. Modifying the recipe of Polk et al.[61] to a two-electrode setup, in combination with real-time monitoring of electrodeposition led to fascinating observations and a novel understanding of the qualitative aspects of electrodeposition on this specific scale. Still, only a selection of the chips was processed.

4.2.1. Small electrolyte volume analysis

The electrodeposition solution volume in the employed setup was orders of magnitude smaller than those seen in conventional electrodeposition setups. This might influence the bulk ionic concentration available during the initial stages of the electrodeposition process. It was estimated that $4.34 \cdot 10^{-8}$ mole of silver ions is used, while $6 \cdot 10^{-5}$ mole is available in the bulk solution. This is based on the longest deposition time, 262s, at 16μA, and it assumes no dissolution of the anode silver sheet. This is calculated using the concentration and the electrodeposition volume injected, which is also captured in the code shown in Appendix D.4.

4.2.2. Parameter determination

After initial attempts to reproduce the methodology of Polk et al.[61], additional modifications needed to be made to the setup. Since the setup was galvanostatically controlled in order to estimate the deposition thickness, the voltage was a compliant parameter. However, here it was found that the voltage magnitude was critical to achieving controlled silver deposition.

Multiple tests were performed on chips from the second batch in order to optimise the electrodeposition process. Various current densities were attempted, and also the silver nitrate concentration was altered as these were the main independent variable with influence on the deposition process. Initially, the process either produced large crystalline structures, partial deposits or completely failed to deposit any material. Although they were beautiful, these electrodeposits carry no scientifically compelling conclusions their results are left to Figure A.4 in Appendix A.4.

After these attempts and the integration of the microscope into the setup, a more structured approach was adopted to find the optimal electrodeposition parameters. For this, a logarithmic sweep of current was used to cover a large range of current magnitudes in a short time span. This was done for most microwell diameters available over 7 separate chips. This showed that the required current range for all diameters was strikingly similar, $\approx 1\mu$A, as can be seen in Figure 4.4. The results also revealed dramatically qualitative differences in the deposition profile. This can for instance be noticed when comparing the concave profile of chip 4 to chip 5, both having a 50μm diameter. In chip4 and chip 7 there were deposits prior to the application of galvanostatic control. Partial depositions were observed in chip 3 and chip 4. The magnification of the microscope was not high enough to assess the electrodeposition quality in microwells with a diameter $\leq 20\mu$m, although the deposition in chip 1 seems uniform.

The results of chip 2 and chip 5 require a more detailed overview and are shown in Figure A.5 in Appendix A.4. Particularly, in chip 5 with a microwell diameter of 100μm, the formation of pillars is observed, although later the remaining gold seed layer is also covered with a silver deposit.

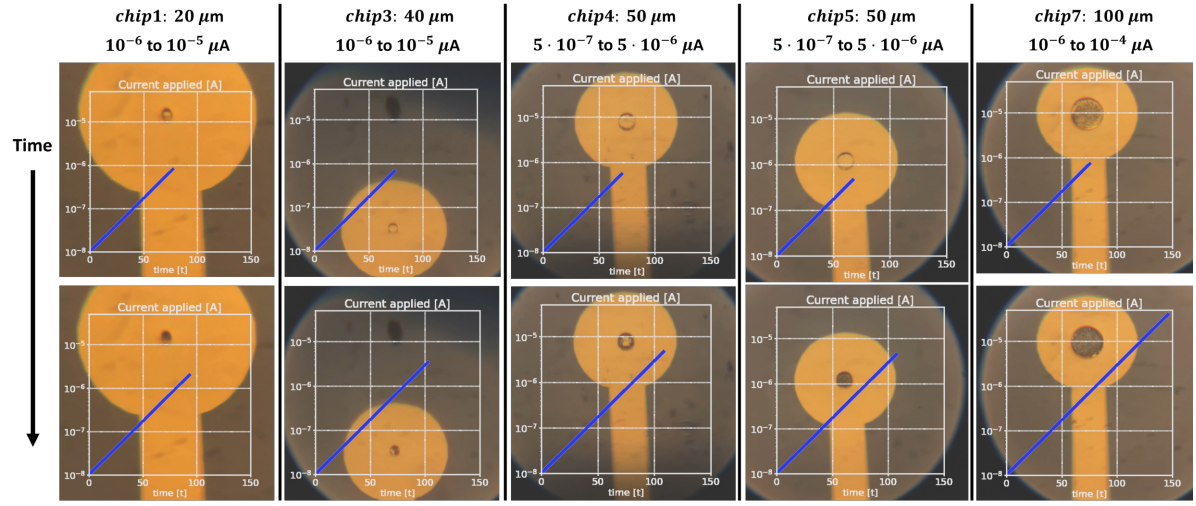

Figure 4.4: The snapshots of various microwells undergoing electrodeposition with logarithmically scaled current magnitude sweep. The microwell photo is superimposed with a plot of the progress within the current sweep, log-current vs time. The snapshots of different microwells are represented in each column, where the sampled times increase downwards in each column separately.

The results showed that the current magnitude was decisive in achieving an electrodeposit, although literature suggests current density is the metric of importance. After consultation with knowledgeable individuals about the suspected cause of this phenomenon it was indeed hypothesised that not the current density or magnitude, but the potential over the microwell's seed layer is responsible for successful electrodeposition. This was thought to be related to overcoming the initial barrier of silver deposition on gold through its Helmholtz layer. The specific current magnitude at the initiation of electrodeposition that was observed was thought to be an affectant of its driven voltage.

Still desiring galvanostatic control, this required setting the current equal to the fraction of the intended voltage over the cell impedance. The impedance of such a cell is primarily determined by the microwell's small recessed opening [67]. From here, the current magnitude corresponding to the voltage needed to initiate the electrodeposition reaction would be determined. Previous observations of large-diameter microwells demonstrated the best characterisable deposition responses. The 250μm diameter microwells from the last batch were selected for finding the best operating current magnitude. Also, it was already shown electrodeposition started around the 1μA current magnitude. In these additional tests on the 250μm diameter microwells, the current, voltage and impedance traces were recorded during electrodeposition.

The current was logarithmically swept from 10nA to 10 – 50μA, corresponding to a current density of 20μA/cm^2 and 100mA/cm^2, respectively. This range was based on the previously obtained results. The impedance and voltage were simultaneously measured, from which clearly the threshold could be identified. However, high variation was obtained between the individual results, indicating different threshold voltages for the same current densities. Two of these results are shown in Figure 4.5. Here also the total injected charge until the observed critical voltage was calculated to be in the order of tens of mC.

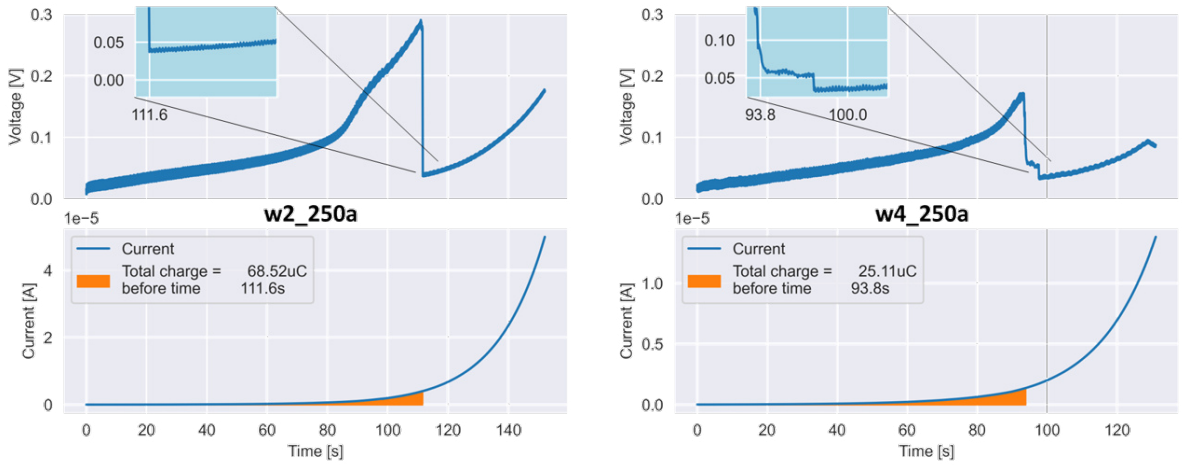

Figure 4.5: The measured voltage and current trace of the last batch's chips wafer 2 and 4 for microwell diameters 250μm. Driving a current with a logarithmic sweep from 10nA to 10 – 50μA, revealed a critical voltage point where the electrodeposition process initiated.

4.2.3. Characterisation of deposits

To ensure the required critical voltage was always reached, the observed maximum current needed was doubled. Specifically, using a current density of 100mA/cm^2 for a 100μm microelectrode yielded a current magnitude of 8μA. Consequently, a current magnitude of 16μA was used for all consecutive electrodepositions.

The chips from wafer 1 were kept as a reference during electrophysiological measurement and were therefore not exposed to the electrodeposition process. The chips from wafer 2 through 4 with microwell diameters 20μm through 100μm were deposited on. The 30μm diameter microwell marked the smallest dimension with useful profilometer data. This was because the profiling-tip-radius was 12.5μm, which did not allow measurement of the bottom plane for $< 30\mu$m microwell diameters. This meant the 20μm diameter microwells were not able to be profiled, and their results are not discussed here, although their characteristics can be found in Appendix A.4.

There was no strict requirement set on the height of the formed deposit, although it was ideally at least a few microns in height, while not surpassing the SU-8 thickness. Therefore the time used for electrodeposition could vary. Unfortunately, the SourceMeter used did not allow simple control over the recording period due to the fluctuating source-delay time adding approximately 15% extra time to a set sweep. It was for this reason only a couple of delays were calibrated, yielding four different timings used for electrodeposition. The timings were 65s, 112s, 138s and 262s. These correspond to the specified source-measurement delay timings noted in Table 4.2. Each source-measurement delay was executed 2500 times, corresponding to the 2500 measurements for each electrodeposition. The theoretical injected charge for the respective duration at a current magnitude of 16μA was calculated for each deposition duration and can be seen in the same table.

Table 4.2: Total theoretical charge in mC transferred to chips during electrodeposition of wafer 2 through 4 for microwell diameters 30μm through 100μm. The first column shows the source-measurement delay that could be specified on the Keithley SourceMeter, with its corresponding time duration in the second column. The third column contains the charge that can be calculated by integrating 16μA for that particular duration. See Appendix D.4 for the data processing.

delay s	time s	charge mC
0.02	65	1.040
0.04	112	1.792
0.05	138	2.208
0.10	262	4.192

Taking the minimum value registered by the profilometer before and after electrodeposition gave an indication of the deposited silver thickness. The estimations are summarised in Table 4.3, with

the accompanied profile line plots in Figure 4.6. The injected charges and heights for each of these depositions were also compared against the theoretical performance in Table 4.4. The Python code in Appendix D.4 shows the exact data processing for the generation of Table A.2,

Table 4.3: Estimated silver deposition heights in μm chips of wafer 2 through 4 for microwell diameters 30μm through 100μm. This value is estimated by taking the difference between the minimum profiled heights before and after electroplating. The profile line plots are shown in Figure 4.6. In case the profile was not measured before electroplating, a SU-8 height of 11630nm was used. The measured current traces were obtained during the separate electrodepositions. See Appendix D.4 for the data processing.

	microwell diameter		
wafer	30μ m	50μ m	100μ m
2	6.538	1.757	2.225
3	8.680	3.374	1.952
4	8.670	10.795	4.625

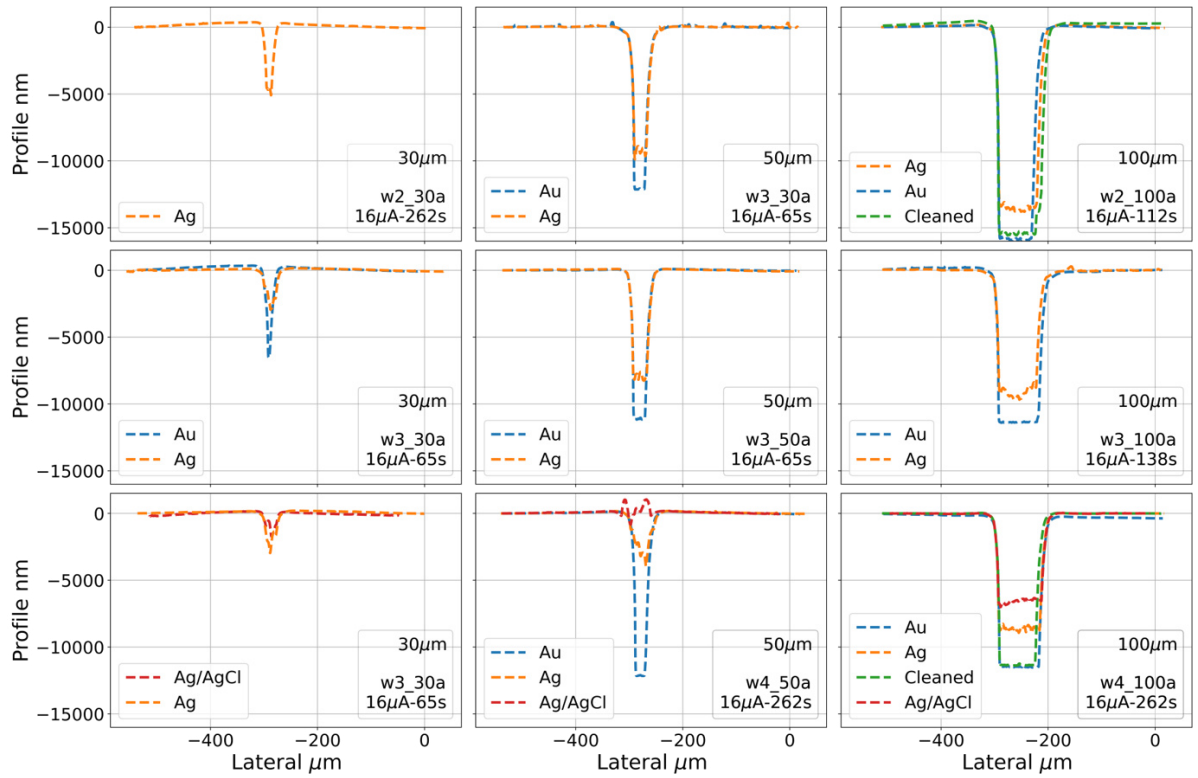

Figure 4.6: The profiles of the last batch's chips wafer 2 through 4 for microwell diameters 30μm through 100μm. The accompanying voltage and impedance traces are shown in Figure A.6. The profiles were made with a DEKTAK profilometer. The superimposed lines show the profiles recorded before electrodeposition *(blue)*, after electrodeposition *(orange)*, and after chlorination *(red)* for each microwell, although not all microwells were recorded at each stage. See Appendix D.5 for the data visualisation code.

Table 4.4: The electrodeposition results from the chips of wafer 2 through 4 for microwell diameters 30μm through 100μm. Within a diameter category, each row represents one chip, which has three data points. The first is the specific time duration used for the electrodeposition process. The second provides the calculated theoretical charge *(left)* besides the measured injected charge *(right)* for the specific duration at a 16μA current. The third data point uses the theoretical charge to estimate the deposited height. This actual height is divided by this theoretical estimate, which yields the value as seen in the table. It is a measure of the actual charge employed for deposition. See Appendix D.4 for the data processing.

microwell diameter								
30μ m			50μ m			100μ m		
time s	charge mC	depos.	time s	charge mC	depos.	time s	charge mC	depos.
65	1.040/0.996	0.042	65	1.040/0.999	0.031	112	1.792/1.797	0.092
65	1.040/0.996	0.055	65	1.040/0.996	0.060	138	2.208/2.196	0.065
262	4.192/4.191	0.014	262	4.192/4.256	0.047	262	4.192/4.191	0.081

The last batch's chip from wafer 3 with a microwell diameter of 50μm was diced on the edge of its microwell, to be able to look inside. An SEM image provided an impressive view of the electrodeposit inside the microwell, as can be seen in Figure 4.7. In these images not only the granular structure of the electroplated material is observed, but also its geometry near the edges. This information was not capturable using the profilometer, because of its wide tip radius. The deposit near the edges seems to be slightly elevated compared to the microwell's centre.

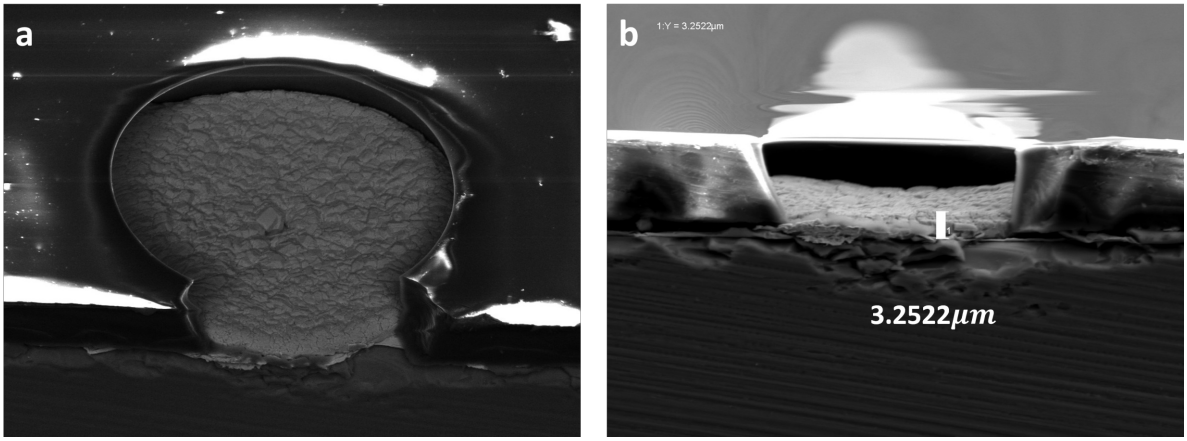

Figure 4.7: The profiles of the last batch's chip of wafer 3 with the 50μm microwell diameter. The chip was diced separately through the edge of the microwell after silver electrodeposition. The SEM image was taken with a Hitachi Regulus 8230. See Appendix A.3 for the settings used. *(a)* An SEM image of the tilted chip with 3D information on the electrodeposit inside the microwell. *(b)* An SEM image taken from the side of the cut, showing its crossection. The white marker shows the same $\approx 3.25\mu$m electrodeposit at the centre of the microwell as seen in the profiled data of Table A.2. The sides of the microwell seem to have slightly more deposited material.

The chlorination of the electrodes also expanded the thickness of the deposits because of the silver that was consumed to form silver chloride. This was done for the 4th wafer of the last batch for all three chips with their respective microwell diameter. The AgCl growth was found to generate a slight radial expansion pushing the surrounding SU-8 upwards. This effect can be seen in the profiles in Figure 4.6. For the 50μm diameter microwell the AgCl layer surpassed the microwell boundary and was therefore not used in successive experiments. Chlorination could also be visually observed through the slight darkening of the silver electrode surface.

4.2.4. Pourbaix diagram

To investigate the hypothesis of voltage-dependent deposition, several people were consulted to provide their expertise and interpretation of the above results. It was found that the electrochemistry for electrodeposition could also be related to Pourbaix diagrams, which indicate the chemical species landscape for the pH scale vs the applied electromotive force. Such a diagram was found in literature [68] and is discussed here in relation to the observed results.

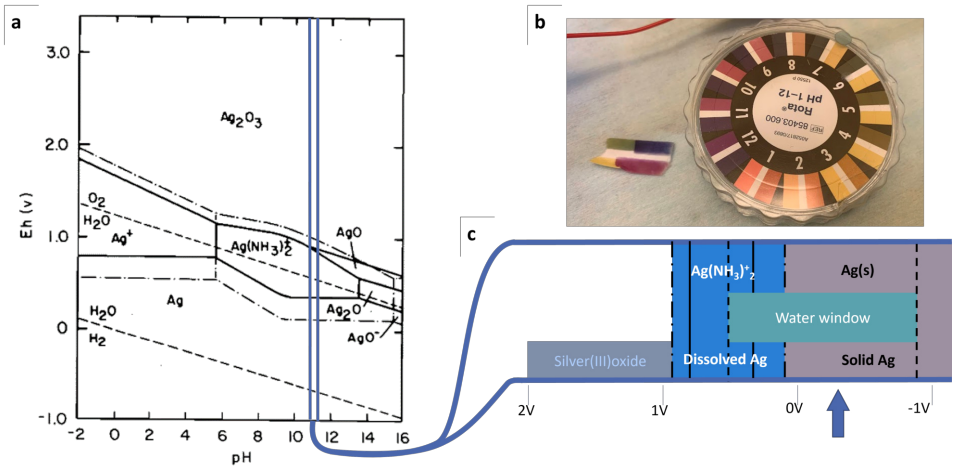

Figure 4.8: *(a)* The Pourbaix diagram for silver-ammonia-water, taken from [68]. The diagram considers an ammonia concentration of 1M at 25°C for atmospheric pressure. These are the same conditions as those used in this work. *(b)* A photo of the pH indicator paper used to validate the theoretical pH estimation of ≈ 11.6. *(c)* The information at 11.6 pH was extracted from the same diagram, to give a better overview of the phase conditions at different voltages applied for this particular case.

Although the Pourbaix diagram in Figure 4.8 (a) was originally constructed for silver dissolution, it does indicate the reaction equilibria, and may therefore provide a guideline for the electrodeposition process. It was estimated that the pH of the aqueous ammonia used was ≈ 11.6, therefore any negative voltage should be sufficient for dissolved silver deposition, see Figure 4.8 (c). Confirmation was done with pH paper, of which a photo is shown in Figure 4.8 (b). Oppositely, forcing a positive current with a resultant positive voltage can be used to again dissolve the silver into the solution, although carefully considering the possibility of surpassing the water window or oxidising the gold microelectrode itself. Possible open circuit potentials complicate the application or measurement of the resultant voltage over the electrode-electrolyte interface.

Nonetheless, this diagram shows that a slightly more negative voltage over the microwell cathode would drive the equilibrium phase to solid. Since electrodeposition implies an electrolytic cell where the cathode is the negative terminal, a slight positive voltage is needed to obtain the desired silver deposition.

4.3. Ultrasound magnitude estimation

The focal intensity magnitude of an ultrasonic signal passing through silicon had to be characterised to know the absolute contribution of the acoustic parameters as independent variables in the final setup. Theoretical estimations were made and confirmed by experimental results and in-situ acoustic simulations.

4.3.1. Theoretical transmitted intensity

From the relation described in Equation 2.2 the reflectivity of a silicon chip in a water medium can be established. Knowing both media's acoustic impedance[1], the reflected fraction can be calculated, yielding 74% of the incident wave intensity.

$$R'_{aq/Si} = 0.74, \qquad Z_{1,aq} = 1.48MRayl, \qquad Z_{2,Si} = 19.7MRayl. \tag{4.1}$$

[1] $Z_{aq} = \overset{\rho[kg/m^3]}{1000} \cdot \overset{c[m/s]}{1480} = 1.48MRayl$, $Z_{Si} = \overset{\rho[kg/m^3]}{2330} \cdot \overset{c[m/s]}{8436} = 19.7MRayl$ at 293K. Data sources:[69, 70]

The reflection happens when the acoustic signal both enters and exits the crystalline silicon. The loss in intensity is the remaining fraction and so the total remaining intensity after the chip can be calculated. A wave transmitted through a piece of silicon submerged in water only leaves 6.8% of the initial intensity, since it passes two silicon interfaces[2].

$$I_{aq/Si/aq} = (1 - R'_{aq/Si})^2 I_0, \qquad = 0.26^2 I_0, \qquad = 0.068 I_0. \tag{4.2}$$

Conventional USNM intensities are in the range of $I_{SPTA} = 0.15$ to 6.2W/cm^2 [71], which correspond to peak pressures $P_{SPTP} = 67.08$ to 427.01kPa, respectively[3]. Achieving the lowest intensity in this range would require the original acoustic source to be able to produce 1MPa instantaneous pressure.

4.3.2. Simulated intensity and profile

Simulations were performed to uncover the intensity magnitude and profile at the second silicon-water interface. In these results a reference simulation, without silicon obstruction, is compared to a simulation with a 300μm silicon plate.

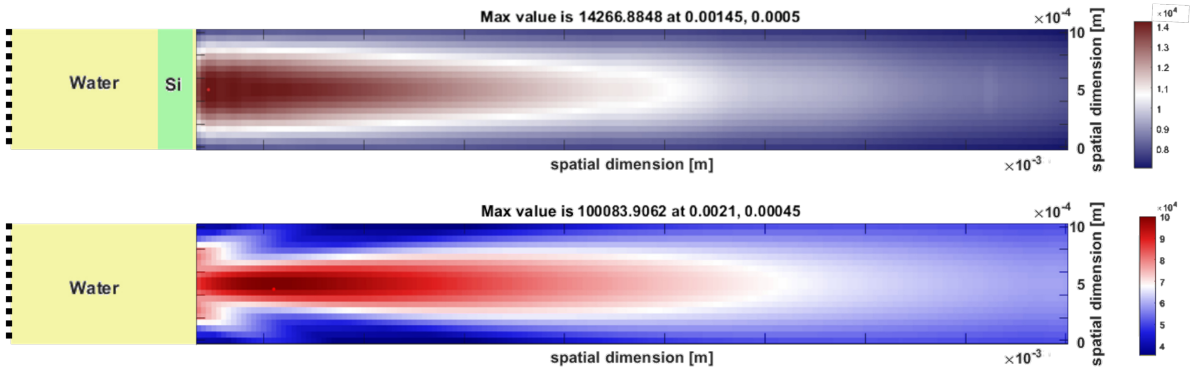

Figure 4.9: The top image shows the intensity profile in water after the acoustic signal has traversed a 300μm silicon wafer. The bottom image shows the same intensity profile in water without any obstructions in its path. Please note their respective magnitude extends. The signal is generated at the left-most dashed line, 1mm away from the intensity profile boundary at the first silicon interface. The distance between each consecutive tick in the horizontal direction of the figure is 1mm.

In the simulation shown in Figure 4.9, the focal intensity is automatically indicated together with its position relative to the second silicon interface. The reference intensity was $I_{SPTP} \approx 100.1$k, whereas the silicon obstructed simulation gave the intensity $I_{SPTP} \approx 14.27$k. The location for the focal spot also shifted by a few hundred microns as indicated by the respective red dots in Figure 4.9.

A difference in intensity profile can also be observed in the same figure. The reference shows some side lobes, which are artefacts of the pressure array and are also seen in real-world phased array transducers[33]. In the silicon-obstructed medium such side lobes can not clearly be identified. However, a high-angle diverging profile is seen close to the second interface, its focal spot is slightly wider, and the focal spot is located significantly closer.

So unlike the mathematically derived value, the achieved focal intensity is measured to be around 14% of the incoming intensity. This would imply a transducer capable of generating an P_{SPTP} of 485kPa.

4.3.3. Measured intesity profile

The measurements that were done prior to platform fabrication indicated the same results as those found in the simulated scenarios. The 3D intensity profiles of this investigation are provided in Figure 4.10, and the 3D view of the unobstructed measurements are provided in Figure B.2.

[2] Since $R'_{aq/Si}$ is equal to $R'_{Si/aq}$, the fraction of transmitted energy through the $aq/Si/aq$ interfaces is $(1 - R_{aq/Si})^2$

[3] The calculated pressure values relate to the instantaneous peak pressures when assuming constant sonication, here referred to as P_{SPTP}. The I_{SPTA} values found in table 1 of Fomenko et al.[71] are used. The intensities used are $I_{SPTA} = 0.152, 0.7, 3.5, 0.72, 6.16\ \text{W/cm}^2$, with their pressure values $P_{SPTP} = 67.08, 143.94, 321.87, 145.99, 427.01$kPa, respectively

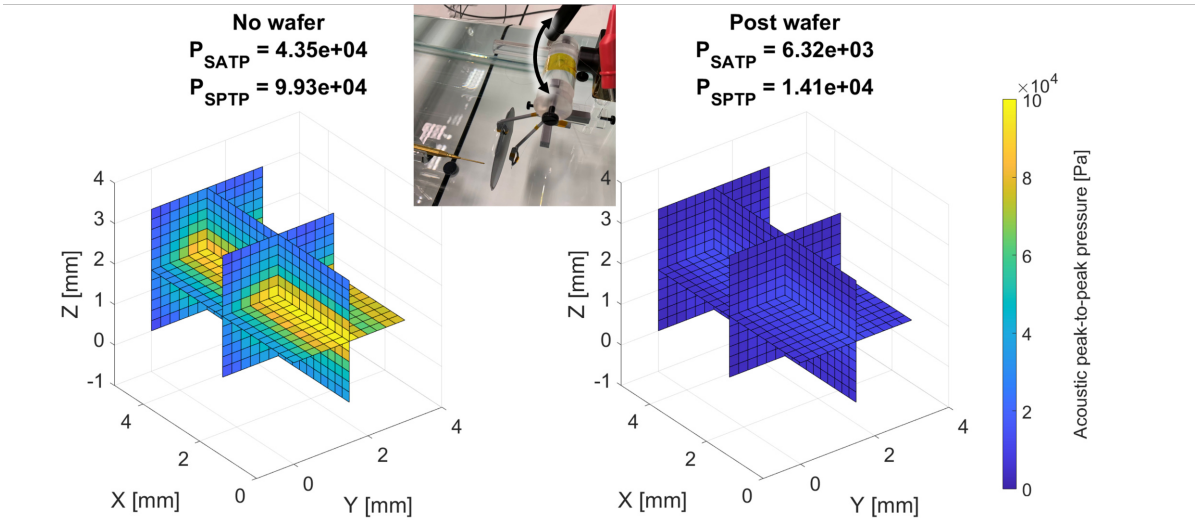

Figure 4.10: Initial measurements are done to confirm the viability of a platform relying on a through-silicon acoustic signal. The intensity metrics are shown at the top of the 3D plots. Each pixel within a slice represents the maximum peak-to-peak pressure, P_{TP}, measured at the respective position. *(Left)* The measured intensity profile of an acoustic source without the obstruction of a silicon wafer. *(Middle)* A small inset photo of the experimental setup. the acoustic source is found behind the silicon wafer with the gold needle hydrophone in front of it. The arrow shows how the holder can be rotated to lift the wafer out of the water without further change to the setup. *(Right)* The same measured intensity profile of the same acoustic source with the obstruction of a silicon wafer.

As can be observed in Figure 4.11, the acoustic intensity profile was characterised for the used electrophysiological setup. This involved measurement of the acoustic signal: without obstruction (control), passing through the scaffold's epoxy film, and passing through the epoxy film plus silicon chip. A 3D view of the unobstructed US profile is provided in Figure B.1.

Remarkably, the output acoustic pressure P_{SPTP} increased to ≈ 350kPa due to the scaffold obstruction, compared to the control, ≈ 280kPa. Here the focal spot location shifted by ≈ 150μm. After the insertion of the chip this shift, however, is absent. The acoustic intensity observed after chip insertion is ≈ 20kPa, and is 5.7% of the scaffold's acoustic intensity output.

Looking at the temporal character of the signals, the envelope of the scaffold obstructed signal peaks after the 10th oscillation, whereas the unobstructed signal does so before. However, the unobstructed signal seems to have higher pressure variations during the falloff. The signal that was obstructed by the scaffold plus chip, has a second peak at the 20th oscillation. A secondary signal or an interruption of the primary signal is also observed in this case.

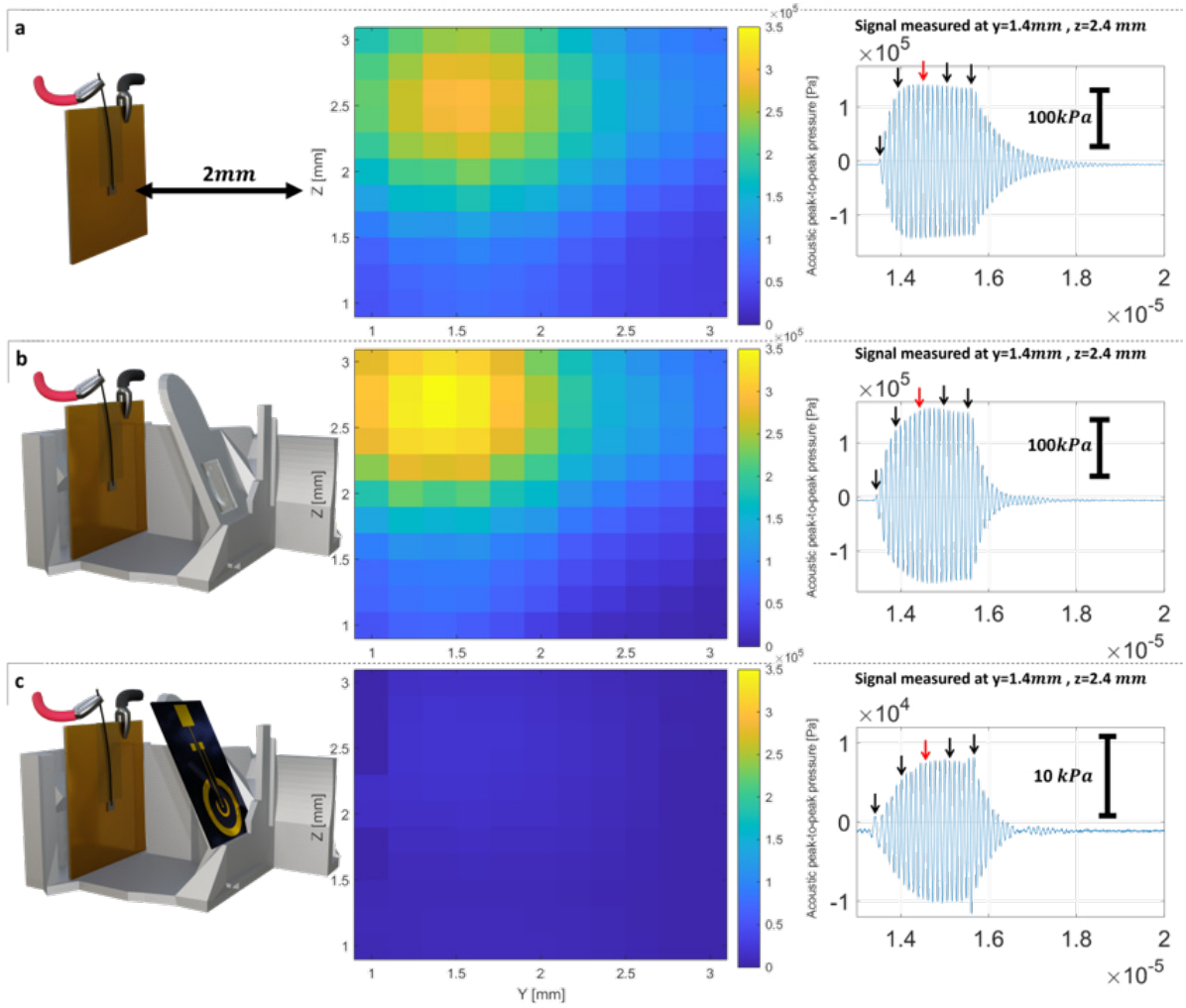

Figure 4.11: Measurements for each of the three conditions are shown: *(a: without obstruction) (b: scaffold obstruction) (c: scaffold plus chip obstruction)* The obstruction is found between the receiving hydrophone and the acoustic source. The crossection of the intensity profile at a 2mm distance from the acoustic source is plotted beside the experimental setup. Each pixel represents the maximum peak-to-peak pressure, P_{TP}, measured at the respective position. Also, the transient signal for a single pixel in the focal region is shown (at y = 1.4mm and z = 2.4mm in the respective crossection). These line plots show the instantaneous pressure measured from 13μs to 20μs after the trigger. Within the line plots every 5th peak is annotated, the 10th in red, others black. The scale of line plot (c) is highly magnified in order to see the signal characteristics.

4.4. System measurements

This section contains the final validation measurements of the platform. Firstly, it is measured whether the WE diameter relates inversely to the impedance at high frequency. Then the electrophysiological measurements of the membrane are presented, together with visual confirmation of BLM formation. Lastly, a single US stimulus measurement of the membrane is shown.

4.4.1. Electrode measurements

EIS measurements of the reference gold electrodes showed capacitative characteristics in the high-frequency regime that correlated with the microwell diameter, as presented in Figure 4.12. The lower-frequency characteristics however also showed variability although these correlated with the measurement order and were therefore thought to be related to the reference electrode stability. These data were also labelled according to their measurement time, and the results for the impedance and phase delay are separated in Appendix C.1.

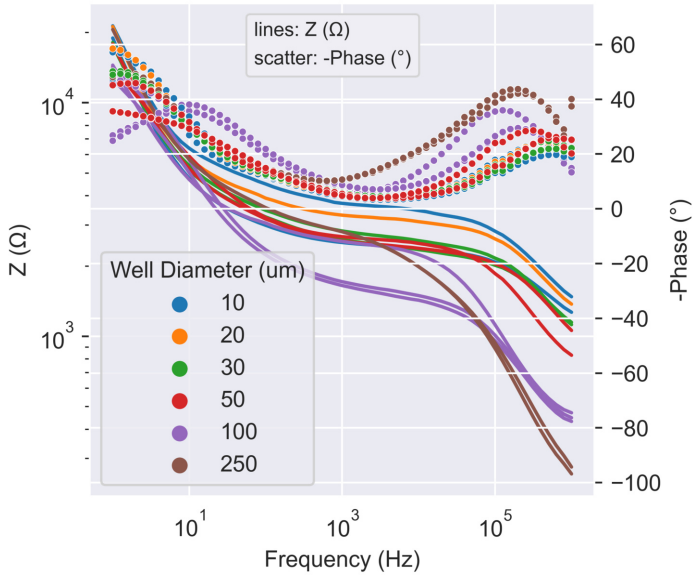

Figure 4.12: The EIS bode plot results of the various microwell sizes. A 10mV sinusoidal signal relative to the REF was applied. The signal frequency was swept from 1MHz to 1Hz with 10 measured points per decade. The colours as indicated in the legend relate to the microwell diameter dimension. The lines present the impedance data, while the points indicate the negative phase delay for each measured frequency.

4.4.2. Membrane measurement

The frequency behaviour was difficult to accurately characterise. This is attributed to the fact that each membrane may have vastly different measurements, but also because of its short transient stability. It is therefore that the results achieved during this thesis are more qualitative.

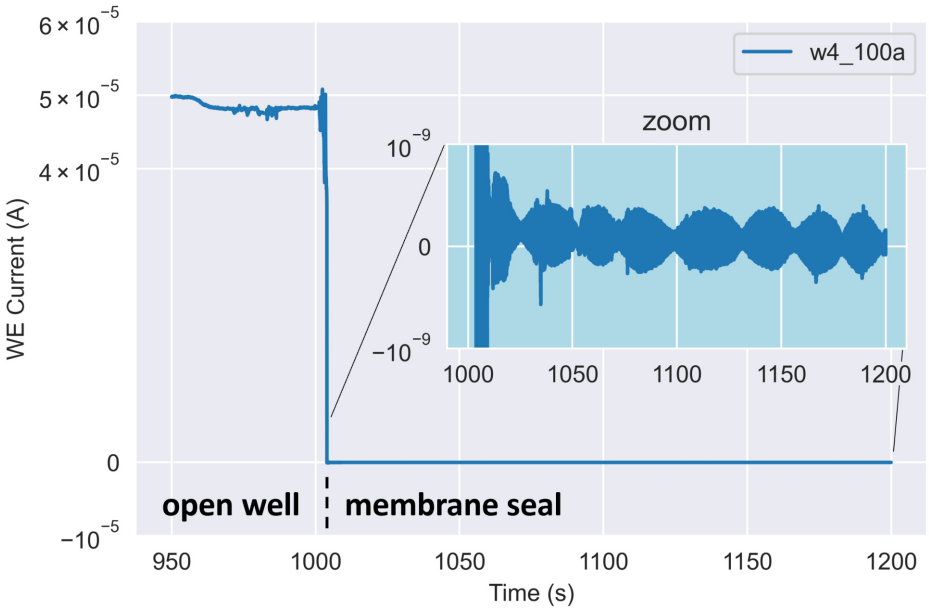

Figure 4.13: A CA recording during the suspension of a BLM on a 100μm diameter chlorinated microwell. A properly equilibrated three-electrode setup is used, where the microwell electrode forms the WE, a chlorinated wire is a REF, and a platinum wire is the CE. The inset plot shows a zoomed-in image of the low current characteristics. The painting method used is shown in Figure 4.16, described in Section 3.7.2.

The CA shown in Figure 4.13 illustrates the drop in current achieved by the membrane seal on top of the microwell. Initially, the current is observed to be ≈ 50μA, corresponding to ≈ 4kΩ at the applied 0.2V. After painting, the current dropped dramatically with a baseline of ≈ 0.1nA, corresponding to ≈ 20GΩ.

The time scale in the figure was clipped from 950s to 1200s, since this is representative of the membrane formation event. Still, the membrane was found to be stable for longer durations (2 to 5min)when it was left undisturbed.

As is shown in the figure inset, the current through the membrane exhibits oscillatory behaviour. The frequency of this oscillation is in the range of 0.05 to 0.1Hz. These results were also observed in other membrane measurements Figure 4.14. Notably, the results were not always easily obtained, since the painting was done by hand and therefore required many tries in order to establish a membrane. This is also seen in the same figure.

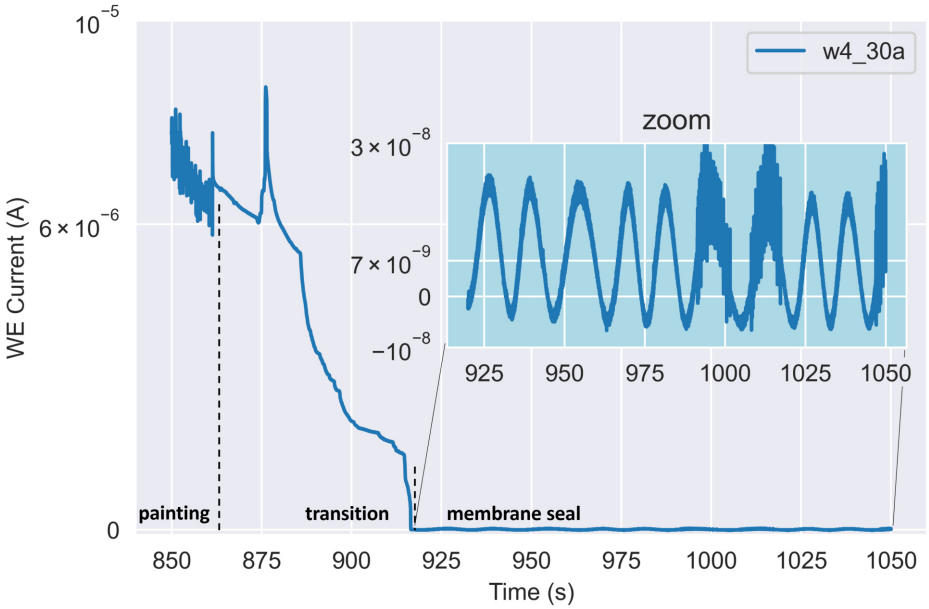

Figure 4.14: A CA recording during the suspension of a BLM on a 30μm diameter chlorinated microwell. Using a three-electrode setup, where the microwell electrode is the WE, a chlorinated wire is the REF, and a platinum wire is the CE. The inset plot shows a zoomed-in image of the low current oscillations. The painting period and membrane formation transition are labelled.

The effect's cause needed to be investigated since such low-frequency behaviour was unexpected. After multiple experiments, it was hypothesised that this oscillatory effect may originate from feedback between WE and REF. Therefore the experiment shown in Figure 4.15 was conducted. Here the membrane was established and the Pt wire CE was removed from the electrolyte and shorted with the REF.

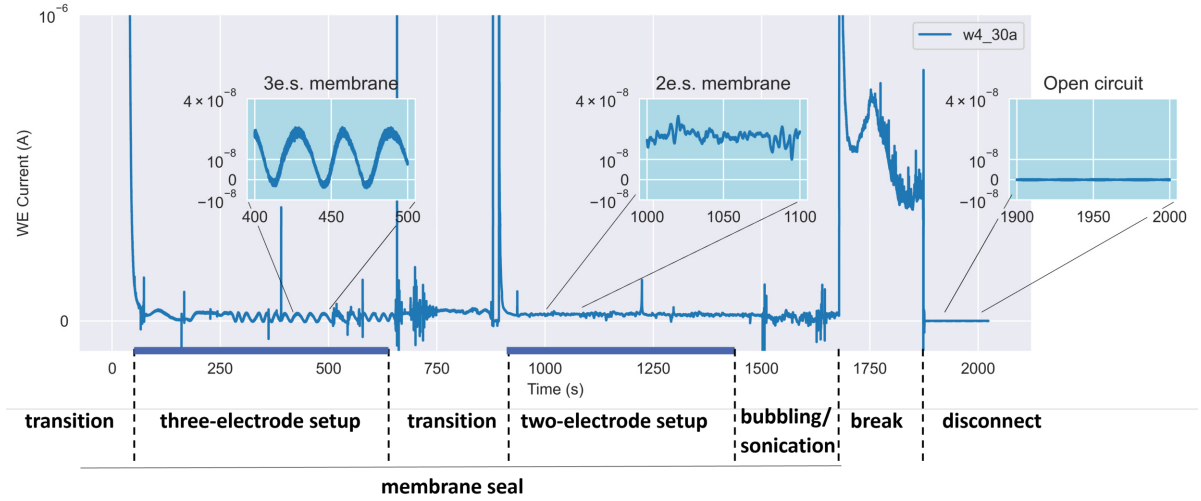

Figure 4.15: A CA recording of a full-time scale experiment where the membrane was already established beforehand. The actions taken during the measurement are shown beneath the plot. The two-electrode setup was restored and air bubbles were used to remove the membrane seal.

Also, image recordings were made during the painting of the membrane and discolouration of the WE was observed after electrical confirmation of the membrane seal. The before and after snapshots of such a result for 100μm diameter microwell are shown in Figure 4.17. The colour difference was thought to be unrelated to the lighting conditions since the microwell's surroundings did not show such colour discrepancies. The enlarged image is shown in Appendix C.2.

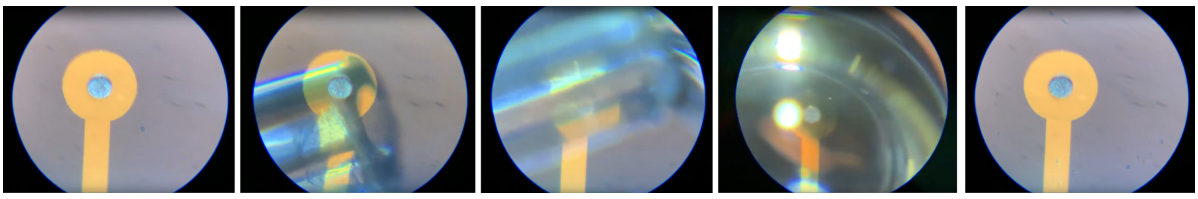

Figure 4.16: *From left to right* (1) The microwell with Ag/AgCl electrode on the bottom, properly wetted and submerged in KCl electrolyte. (2) Lipid-dipped pipette tip brought into close proximity. (3) An air bubble is pipetted sticking to the end of the tip. (4) The air bubble is moved over the microcavity, depositing lipids on the SU-8. (5) The lipids self-assemble on top of the microwell and form a lipid bilayer.

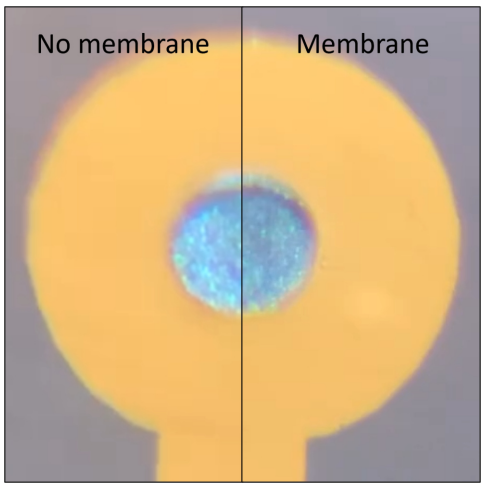

Figure 4.17: Images acquired with the microscopy setup before (left) and after (right) a membrane was established. The images show the discolouration seen at 100μm diameter microwell after a seal was electrically registered.

Lastly, acoustic stimulation was done on an established membrane of the 30μm diameter microwell. Multiple acoustic stimulations (n=5) of the membrane over a series of CA measurements did not yield any noticeable effect on the current characteristics. However, during one of the acoustic stimulations, an effect was observed. The exact stimulation onset and timings were not recorded although noted down by hand. The acoustic stimulation showed a disruption in the membrane several seconds after applying the maximum capable intensity. The acoustic source was turned off when the membrane was thought to be disrupted. The overview of this experiment is shown in Figure 4.18

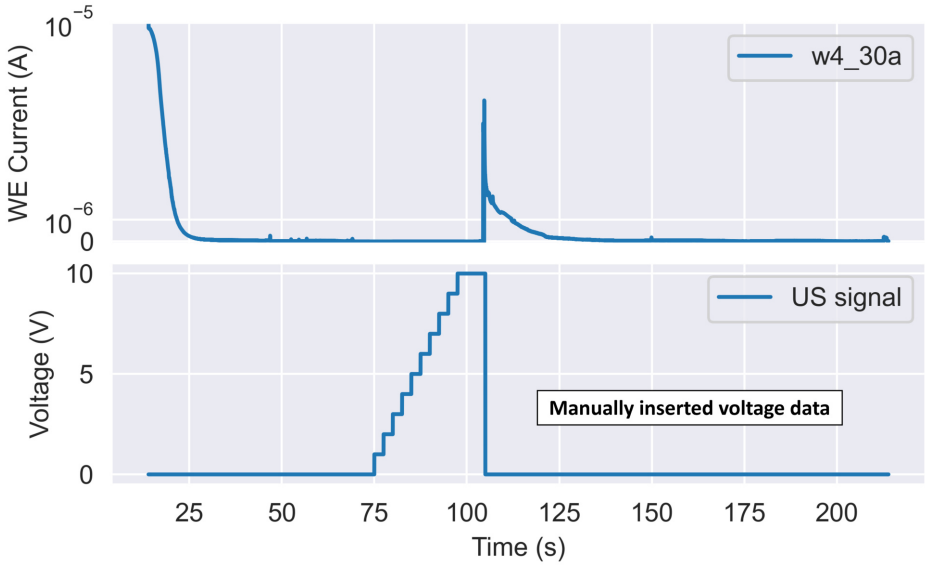

Figure 4.18: A CA recording of this membrane seal was already established beforehand. The acoustic source was turned on and seemed to disrupt the membrane when it was brought to its maximum intensity of stimulation. The exact timings of the acoustic signal onset, step increases and termination are not known. The voltage vs time data is constructed from manual notes taken during the experiment.

5 Discussion

Firstly, this chapter will give a brief overview of the limitations in the measurement speed of the current setup and explain the relevance of such high-speed measurements. Then the observed results of the fabrication of such a research platform are discussed here. The electrodeposition results are mainly interpreted through the lens of electrochemistry. Then a short discussion is provided on the acoustic characterisations done. Lastly, all electrophysiological observations are interpreted, with a focus on the measurements of the bilayer lipid membrane.

5.1. Limitations in measurement speed

This thesis work assumes that the biophysical mechanisms for USNM are correlated to measurable transmembrane electrophysiology. The series of experiments carried out by Yoo et al.[72] supports this assumption. The study also shows its research complexity, which requires interdisciplinary collaboration and the use of an elaborate set of resources to investigate the mechanistic contribution of individual ion channel types. Still, other mechanisms are thought to be partially responsible for neuron US response. Throughout published works, different regimes of acoustic parameters are being tested, which complicates the formation of a definitive narrative. The measurability of US stimuli, for the purposes of this investigation, is still limited by the sampling frequencies of hundreds of kilohertz to a few megahertz. Resolving the individual pressure variations within such a frequency range would require sub-microsecond resolution. Ideally, even faster sampling is possible to distinguish individual ion channel gating events, which are in the order of nanoseconds [32]. This is needed to overcome the temporal kinetics of fluorescent protein sensors such as GCaMP6f are insufficient to monitor calcium responses, since its rise and fall time is still in the order of tens of milliseconds [50]. The potentiostat used for the measurements presented does not have the capacity for such fast measurements. It is therefore that the developed in-vitro research platform must be integrated with a high-bandwidth measurement device. This also requires additional design considerations towards low-noise, low-capacitance signal transfer for amplification.

5.2. Fabrication and deposition

The fabrication of the wafers and the various processes used in the cleanroom yielded predictable complications which were easily solved with the guidance of experienced supervisors. Gold flake redeposition during lift-off was tackled with additional cleaning steps, while the SU-8 patterning required underexposure and overdevelopment to open the negative photoresist fully. Standard thin film resistance measurements showed a specific resistance between 28.0 and 29.7pΩm, which are comparable to those found in established databases, although slightly higher. This increase could be explained by the gold-spitting defects originating from the evaporation process, or by an increased gold thickness overall.

The electrolyte used during electrodeposition was found in a small reservoir and was thought to potentially inhibit the process due to the finite availability of ions. This was theoretically investigated

and deemed an insignificant effect based on the mass of silver ions deposited with the current applied. The calculated amount of silver ions used during electrodeposition with the current density used was several orders of magnitude smaller than the total silver ions available.

The log sweep results indicate that the used electrodeposition parameters did not necessarily yield reproducible deposition profiles for the initially employed process. The current magnitude was strikingly similar for each microwell diameter, although short time spans were used. Still, it could not be afforded to investigate with long process times. Instead, these electrodepositions executed under 5min provide the observation that the microwell silver deposition is dependent on voltage. Arguably, current control is still needed to allow calibration of the deposit thickness. A current of 16μA was applied for all subsequent electrodepositions, pushing the cathode interface to a negative potential of a few hundred millivolts. This was enough to initiate deposition and is thought to be related to overcoming an initial voltage barrier.

Still, depositions were not fully controlled and the silver layer thicknesses had high variability. Theoretical estimation of the silver deposition volume and height did not yield comparable results. This suggests an alternative current pathway or deposition beside the microwell's electrode. This could be achieved through different redox reactions, particularly O_2 evolution in the presence of slight potential shifts at this very basic pH.

Evidence also suggests that the gold seed layer is not always uniformly deposited, as can be seen in Figure A.4 (e,f) and Figure A.5. This could also be explained by the gold-spitting defects, which could provide certain spots on the electrode with better conductivity resulting in a faster local deposition. On the other hand, it might be the case that a thin layer of SU-8 remained on the gold electrode after development, which would yield similar deposition results.

The obtained SEM images provide a nice overview of the silver deposit quality in a 50μm diameter microwell. They indicate the centre of the deposition profile to be slightly depressed relative to the deposit found closer to the microwell walls. This can be explained by the field lines of ionic supply. When the ions are in flux, the edges of the recessed electrode have access to more of them because of the particular geometry. Other unknown effects might also contribute to this particular deposition profile, such as the direction of the electric field within the microwell. This electric field is thought to be normal to the electrode surface although part of the gold seed layer is unexposed, perhaps allowing a significant radial electric field to establish in the seed layer proximity.

Also, the SEM images validate the profiled result and provide information on the crystalline structure of the electrodeposited silver. No large crystallisations seem to have formed yielding a rather uniform deposition on the micro-scale. More chips should be characterised with SEM to confirm the findings reported here.

The chlorination methodology was taken directly from Polk et al.[61] and proved to be an excellent way to form an Ag/AgCl electrode. The chlorination could be visually confirmed by AgCl's slightly darker tone. The stability of the AgCl layer was untested although this would be important for obtaining reproducible results. Also, the thickness of the formed AgCl layer seemed to be more than the designed 100nm from profilometer measurements, this could have resulted in significantly higher series resistance of the electrode itself.

The presented Pourbaix diagram provides a theoretical framework which may provide a possible explanation for the observations that were made. However, many other electrochemical mechanisms might be involved. These potentially consist of unknown kinetics and unanticipated chemical pathways. Although electrodeposition is not excused from the voltage-dependency of electrochemical reactions, the correlated phenomena do not necessarily imply causality. Additionally, the voltage might not be as controllable as it is deemed to be, because of OCPs and the polarisable character of silver.

Besides the discussion on theoretical validity, the developed procedure did produce the needed results for Ag/AgCl electrode fabrication, which progressed this project to the next stage.

5.3. Ultrasound intensity profile interpretation

The discrepancy between the mathematically derived peak intensity and the simulated or experimental intensity is attributed to the refraction of the indicent acoustic signal. Essentially, the high sound-speed silicon medium acts as a converging lens for the diverging ultrasound source. This effect may explain the slight increase in intensity after the acoustic signal exits the silicon relative to the mathematical estimations.

The increase in acoustic intensity achieved by the epoxy film in the electrophysiology scaffold was unexpected but can be explained by a similar effect as seen in the simulations. The epoxy window created might form an acoustic lens amplifying the focal gain. However, the epoxy film is thought to have a slightly concave form, which would imply a diverging signal. Additionally, the epoxy's acoustic impedance is comparable to water [33] limiting the potential focusing effect. There may be value in such a simplistic acoustic amplification method, which would require further investigation.

The temporal analysis also indicates a gain in the peak pressure of the scaffold obstructed signal over the unobstructed signal. And although this effect may still either originate from the focused pressure of refractive interference, a frequency shift originating from the setup change could also yield a more optimal mechanical resonance of the PZT source.

From the same analysis, the chip's induced acoustic losses can be characterised in more detail. The introduction of the silicon interface, caused by inserting the chip, shows an interrupted envelope which could indicate interference by a reflected signal arriving at the respective moments.

The focal spot shift seen for the scaffold measurement indicates that alignment is robust throughout the assembly of setup components, although not perfect. Insertion of the chip also deviated the focal spot from its prior location. However, this was in the opposite direction and might indicate that the epoxy film had a slight angle, which the chip corrected. Still, the shifts might also be cumulative and opposite in direction by chance.

The pressure needed by this particular transducer was not yet high enough to provide acoustic stimuli in the range of USNM, especially considering the instantaneous pressure recorded following the acoustic losses induced by the chip. Optimising the acoustic intensity and identifying possible reflective losses could be done by scanning through the signal in the time domain. This would allow for the optimisation of refractive components in the scaffold. The acoustic output can also be increased using a higher driving voltage, which is an easier and more viable approach.

5.4. Membrane measurements

Through measurement of differently sized microwell diameters, it was made sure that the electrophysiological measurements were based on information acquired by the WE within the respective microwell. The last batch's chips without silver deposits were used to examine this. EIS measurements were obtained with a two-electrode setup, capturing the capacitative features of the polarisable gold electrodes. This indicated that the setup was capable of measuring the characteristics of the WE.

Two chips, one with a 30μm diameter microwell and another with a 100μm diameter microwell were employed for membrane measurements. Membranes could successfully be painted on top of both microwells and showed the expected current drop during CA measurements.

Photos of the BML on top of the microwell are shown in Figure 3.8. The membrane is indirectly observed via the significant colour difference seen through the pocket microscope. Since the photos were taken at different time points and therefore the photo's lighting conditions needed to be analysed, this was not deemed the cause for the discolouration. Although other sources also show the possibility of BLM visual confirmation [73, 74], this observed visual effect might also be explained by the chemical reactions happening at the Ag/AgCl WE. AgCl is known to be photosensitive and under photoreduction when exposed to low-wavelength light.

The REF and WE should be placed in close proximity to establish a proper voltage reference. Although the REF Ag/AgCl wire was placed very near the microwell, there may still have been a delayed voltage influence of the WE on the REF. The physical distance between the WE and the REF might have been large enough such that an additional voltage difference is registered. This voltage would probably

originate from the potential difference between the CE and WE, i.e. the current path. Since this small discrepancy between the measured and applied voltage can not be corrected instantaneously, there is negligible current flowing from the WE to the REF. The exact mechanism for the hypothesised feedback is still to be investigated.

Multiple ultrasonic stimulations of a 30μm membrane were attempted, of which only a single one showed a noticeable current increase. The spike in current is thought to be caused by a disruption in the membrane induced by the US stimulus. Still, other effects might have played a role in this particular current spike, although the temporal correlation is unlikely to be an effect of chance. Still, more experiments with the same setup should be done to indicate the causality of this effect.

6

Conclusion

This thesis showcased the work done during the end-to-end development of a BML research platform for the application of ultrasound neuromodulation. The complete integration of the multidisciplinary aspects was proven to be possible. The novel approach of adaptive packaging was introduced and employed to couple macro components and measurement equipment used with the micron-scale region of interest on a passive chip. The chips of 12 by 19mm with variable size microwells in the order of tens of microns were designed and later fabricated in the cleanroom. These chips were then interfaced with simple modded alligator clips, 3D-printed scaffolds, and a pocket microscope to reveal electrochemical activity and analyse electrodepositions in real-time. Electrodeposition for the small-scale systems was investigated and optimised. At a high pH value, it was found that voltage-dependent current-controlled electrodeposition could robustly form silver layers on recessed gold seed layers of several microns. The resulting deposits could be analysed with profilometry and scanning electron microscopy and compared to theoretical charge injection estimates. The preparation and resuspension of lipids were executed and BMLs were suspended on top of the microwells using the air bubble painting technique. Simple electrical characteristics of the membrane could be established by using two- and three-electrode setups. The realm of electrochemistry was explored to allow for a proper understanding of the mechanisms that play a role in the realised electrophysiological measurements. Overall, the created platform presented successful operation and therefore shows good prospects for its integration into a final lab-on-a-chip research tool.

6.1. Contributions

As investigations into the biophysical principles of ultrasound continue, in-vitro experiments can aid the research on the specific influence of acoustic parameters on cellular mechanics. The work was done as part of a greater initiative supported by the Human Frontiers Science Program (HFSP). However, serving this particular investigation, here it is shown how the various aspects involved are combined during the creation of a platform electrophysiologically interrogating membranes exposed to an ultrasonic signal. Although more experimentation could still be done to benefit this fundamental research, results achieved outside of this specific goal were also deemed significant. These results find relevance in the field of electrodeposition, and electrochemistry. Additionally, the great potential of doing experimental research in combination with 3D printing was demonstrated.

6.2. Future work

Thinning of the backside silicon under the microwell front end will allow a higher acoustic intensity to be transmitted to the BML. This would be an additional but simple step inserted at the end of the microfabrication process. A systematic optimisation is needed to find a clear relationship between the microwell diameter, the current and other variables that influence the electrodeposition process. However, the electrodeposition itself was found to be a very time-consuming aspect of the platform fabrication and it could be argued that an alternative approach should be pursued. This could be achieved through the use of ion-beam-aided silver deposition or simply by using bare polarisable

gold electrodes. Another fabrication step that should be explored is the final integration of the chip's second electrode, this will allow for a simplified experimental setup and potentially more accurate measurement of electrophysiological measurements. Also, it is known that many other techniques exist for the assembly of a stable lipid bilayer besides the discussed painting technique, their viability should be explored. Future fabrication of an active chip capable of low-noise high-bandwidth amplification of the electrophysiological signal would allow for reliable measurement of single ion channel channels incorporated into the lipid bilayer. This incorporation of the ion channels was not done in this project and would require expertise in biological purification steps. In addition, this thesis showed a need for supplementary expertise in the fields of acoustics, microfabrication, and electrochemistry, which will necessarily make the project multidisciplinary.

References

[1] Marcus E. Raichle. "Two views of brain function". en. In: *Trends in Cognitive Sciences* 14.4 (Apr. 2010), pp. 180–190. ISSN: 1364-6613. DOI: 10.1016/j.tics.2010.01.008. URL: https://www.sciencedirect.com/science/article/pii/S136466131000029X (visited on 05/29/2022).

[2] Nikolaus Kriegeskorte and Pamela K. Douglas. "Cognitive computational neuroscience". en. In: *Nature Neuroscience* 21.9 (Sept. 2018). Number: 9 Publisher: Nature Publishing Group, pp. 1148–1160. ISSN: 1546-1726. DOI: 10.1038/s41593-018-0210-5. URL: http://www.nature.com/articles/s41593-018-0210-5 (visited on 05/29/2022).

[3] Karla Batista-García-Ramó and Caridad Ivette Fernández-Verdecia. "What We Know About the Brain Structure–Function Relationship". In: *Behavioral Sciences* 8.4 (Apr. 2018), p. 39. ISSN: 2076-328X. DOI: 10.3390/bs8040039. URL: https://www.ncbi.nlm.nih.gov/pmc/articles/PMC5946098/ (visited on 05/29/2022).

[4] Rhaya L Johnson and Christopher G Wilson. "A review of vagus nerve stimulation as a therapeutic intervention". In: *Journal of Inflammation Research* 11 (May 2018), pp. 203–213. ISSN: 1178-7031. DOI: 10.2147/JIR.S163248. URL: https://www.ncbi.nlm.nih.gov/pmc/articles/PMC5961632/ (visited on 05/19/2021).

[5] Elinor Ben-Menachem. "Vagus-nerve stimulation for the treatment of epilepsy". en. In: *The Lancet Neurology* 1.8 (Dec. 2002), pp. 477–482. ISSN: 1474-4422. DOI: 10.1016/S1474-4422(02)00220-X. URL: https://www.sciencedirect.com/science/article/pii/S147444220200220X (visited on 05/19/2021).

[6] Joel S. Perlmutter and Jonathan W. Mink. "Deep Brain Stimulation". In: *Annual review of neuroscience* 29 (2006), pp. 229–257. ISSN: 0147-006X. DOI: 10.1146/annurev.neuro.29.051605.112824. URL: https://www.ncbi.nlm.nih.gov/pmc/articles/PMC4518728/ (visited on 03/08/2022).

[7] Andres M. Lozano and Nir Lipsman. "Probing and Regulating Dysfunctional Circuits Using Deep Brain Stimulation". en. In: *Neuron* 77.3 (Feb. 2013), pp. 406–424. ISSN: 0896-6273. DOI: 10.1016/j.neuron.2013.01.020. URL: https://www.sciencedirect.com/science/article/pii/S089662731300086X (visited on 05/19/2021).

[8] Andy Wai Kan Yeung, Nikolay T. Tzvetkov, and Atanas G. Atanasov. "When Neuroscience Meets Pharmacology: A Neuropharmacology Literature Analysis". eng. In: *Frontiers in Neuroscience* 12 (2018), p. 852. ISSN: 1662-4548. DOI: 10.3389/fnins.2018.00852.

[9] Gerald E. Loeb. "Neural prosthetic interfaces with the nervous system". en. In: *Trends in Neurosciences* 12.5 (Jan. 1989), pp. 195–201. ISSN: 0166-2236. DOI: 10.1016/0166-2236(89)90071-4. URL: https://www.sciencedirect.com/science/article/pii/0166223689900714 (visited on 03/08/2022).

[10] Stuart F. Cogan. "Neural stimulation and recording electrodes". eng. In: *Annual Review of Biomedical Engineering* 10 (2008), pp. 275–309. ISSN: 1523-9829. DOI: 10.1146/annurev.bioeng.10.061807.160518.

[11] Lief Fenno, Ofer Yizhar, and Karl Deisseroth. "The development and application of optogenetics". eng. In: *Annual Review of Neuroscience* 34 (2011), pp. 389–412. ISSN: 1545-4126. DOI: 10.1146/annurev-neuro-061010-113817.

[12] Masahito Kobayashi and Alvaro Pascual-Leone. "Transcranial magnetic stimulation in neurology". en. In: *The Lancet Neurology* 2.3 (2003), pp. 145–156. ISSN: 1474-4422. DOI: 10.1016/S1474-4422(03)00321-1. URL: https://www.sciencedirect.com/science/article/pii/S1474442203003211 (visited on 03/08/2022).

[13] Omer Naor, Steve Krupa, and Shy Shoham. "Ultrasonic neuromodulation". en. In: *Journal of Neural Engineering* 13.3 (May 2016). Publisher: IOP Publishing, p. 031003. ISSN: 1741-2552. DOI: 10.1088/1741-2560/13/3/031003. URL: https://doi.org/10.1088/1741-2560/13/3/031003 (visited on 05/19/2021).

[14] Joseph Blackmore et al. "Ultrasound Neuromodulation: A Review of Results, Mechanisms and Safety". en. In: *Ultrasound in Medicine & Biology* 45.7 (July 2019), pp. 1509–1536. ISSN: 0301-5629.

DOI: 10.1016/j.ultrasmedbio.2018.12.015. URL: https://www.sciencedirect.com/science/article/pii/S0301562919300043 (visited on 05/20/2021).

[15] Song Luan et al. "Neuromodulation: present and emerging methods". In: *Frontiers in Neuroengineering* 7 (2014). ISSN: 1662-6443. URL: https://www.frontiersin.org/article/10.3389/fneng.2014.00027 (visited on 03/08/2022).

[16] Xin Guo and Francis C. Szoka. "Chemical Approaches to Triggerable Lipid Vesicles for Drug and Gene Delivery". In: *Accounts of Chemical Research* 36.5 (May 2003). Publisher: American Chemical Society, pp. 335–341. ISSN: 0001-4842. DOI: 10.1021/ar9703241. URL: https://doi.org/10.1021/ar9703241 (visited on 09/30/2022).

[17] Salman Ul Islam et al. "Intranasal Delivery of Nanoformulations: A Potential Way of Treatment for Neurological Disorders". eng. In: *Molecules (Basel, Switzerland)* 25.8 (Apr. 2020), E1929. ISSN: 1420-3049. DOI: 10.3390/molecules25081929.

[18] Theresa M. Allen and Pieter R. Cullis. "Drug Delivery Systems: Entering the Mainstream". In: *Science* 303.5665 (Mar. 2004). Publisher: American Association for the Advancement of Science, pp. 1818–1822. DOI: 10.1126/science.1095833. URL: https://www.science.org/doi/full/10.1126/science.1095833 (visited on 09/30/2022).

[19] Andres M. Lozano et al. "Deep brain stimulation: current challenges and future directions". en. In: *Nature Reviews Neurology* 15.3 (Mar. 2019). Number: 3 Publisher: Nature Publishing Group, pp. 148–160. ISSN: 1759-4766. DOI: 10.1038/s41582-018-0128-2. URL: https://www.nature.com/articles/s41582-018-0128-2 (visited on 05/19/2021).

[20] Helmut G. Sachs and Veit-Peter Gabel. "Retinal replacement—the development of microelectronic retinal prostheses—experience with subretinal implants and new aspects". en. In: *Graefe's Archive for Clinical and Experimental Ophthalmology* 242.8 (Aug. 2004), pp. 717–723. ISSN: 1435-702X. DOI: 10.1007/s00417-004-0979-7. URL: https://doi.org/10.1007/s00417-004-0979-7 (visited on 03/08/2022).

[21] Max Ortiz-Catalan, Bo Håkansson, and Rickard Brånemark. "An osseointegrated human-machine gateway for long-term sensory feedback and motor control of artificial limbs". eng. In: *Science Translational Medicine* 6.257 (Oct. 2014), 257re6. ISSN: 1946-6242. DOI: 10.1126/scitranslmed.3008933.

[22] Philip M. Lewis et al. "Brain Neuromodulation Techniques: A Review". en. In: *The Neuroscientist* 22.4 (Aug. 2016). Publisher: SAGE Publications Inc STM, pp. 406–421. ISSN: 1073-8584. DOI: 10.1177/1073858416646707. URL: https://doi.org/10.1177/1073858416646707 (visited on 09/14/2022).

[23] William J. Tyler. "Noninvasive Neuromodulation with Ultrasound? A Continuum Mechanics Hypothesis". en. In: *The Neuroscientist* 17.1 (Feb. 2011). Publisher: SAGE Publications Inc STM, pp. 25–36. ISSN: 1073-8584. DOI: 10.1177/1073858409348066. URL: https://doi.org/10.1177/1073858409348066 (visited on 05/19/2021).

[24] Sangjin Yoo et al. "Focused ultrasound excites cortical neurons via mechanosensitive calcium accumulation and ion channel amplification". en. In: *Nature Communications* 13.1 (Jan. 2022). Number: 1 Publisher: Nature Publishing Group, p. 493. ISSN: 2041-1723. DOI: 10.1038/s41467-022-28040-1. URL: http://www.nature.com/articles/s41467-022-28040-1 (visited on 09/30/2022).

[25] Morgan Newhoff. "An Investigation of the Cellular Mechanisms Underlying Ultrasound Neuromodulation". en. In: (Aug. 2020). Accepted: 2020-10-26T19:50:15Z. URL: http://conservancy.umn.edu/handle/11299/216851 (visited on 05/19/2021).

[26] Meghedi Babakhanian et al. "Effects of Low Intensity Focused Ultrasound on Liposomes Containing Channel proteins". en. In: *Scientific Reports* 8.1 (Nov. 2018). Number: 1 Publisher: Nature Publishing Group, p. 17250. ISSN: 2045-2322. DOI: 10.1038/s41598-018-35486-1. URL: https://www.nature.com/articles/s41598-018-35486-1 (visited on 05/20/2021).

[27] William J Tyler, Shane W Lani, and Grace M Hwang. "Ultrasonic modulation of neural circuit activity". en. In: *Current Opinion in Neurobiology*. Neurotechnologies 50 (June 2018), pp. 222–231. ISSN: 0959-4388. DOI: 10.1016/j.conb.2018.04.011. URL: https://www.sciencedirect.com/science/article/pii/S0959438817302015 (visited on 10/08/2022).

[28] Andreas J. W. Hartel et al. "High bandwidth approaches in nanopore and ion channel recordings - A tutorial review". en. In: *Analytica Chimica Acta* 1061 (July 2019), pp. 13–27. ISSN: 0003-2670. DOI:

10.1016/j.aca.2019.01.034. URL: https://www.sciencedirect.com/science/article/pii/S0003267019301035 (visited on 05/30/2022).

[29] Bin Feng, Longtu Chen, and Sheikh J. Ilham. "A Review on Ultrasonic Neuromodulation of the Peripheral Nervous System: Enhanced or Suppressed Activities?" en. In: *Applied Sciences* 9.8 (Jan. 2019). Number: 8 Publisher: Multidisciplinary Digital Publishing Institute, p. 1637. DOI: 10.3390/app9081637. URL: https://www.mdpi.com/2076-3417/9/8/1637 (visited on 07/02/2021).

[30] William J. Tyler et al. "Remote excitation of neuronal circuits using low-intensity, low-frequency ultrasound". eng. In: *PloS One* 3.10 (2008), e3511. ISSN: 1932-6203. DOI: 10.1371/journal.pone.0003511.

[31] David P. Darrow. "Focused Ultrasound for Neuromodulation". en. In: *Neurotherapeutics* 16.1 (Jan. 2019), pp. 88–99. ISSN: 1878-7479. DOI: 10.1007/s13311-018-00691-3. URL: https://doi.org/10.1007/s13311-018-00691-3 (visited on 03/09/2022).

[32] Andreas J. W. Hartel et al. "Single-channel recordings of RyR1 at microsecond resolution in CMOS-suspended membranes". In: *Proceedings of the National Academy of Sciences* 115.8 (Feb. 2018), E1789–E1798.

[33] Timoteo Oliveira, Flávio Buiochi, and Estevão Patricio. *Development and characterization of a 2D phased array ultrasonic transducer for underwater applications*. Jan. 2017. DOI: 10.26678/ABCM.COBEM2017.COB17-2391.

[34] Frederick W. Kremkau. *Diagnostic Ultrasound: Principles and instruments*. Publication Title: Amazon. 2006. URL: https://www.amazon.com/Diagnostic-Ultrasound-Instruments-Frederick-Kremkau/dp/0721643086.

[35] M. J. Rice. "Acoustic attenuation in crystalline solids". en. In: *Proceedings of the Physical Society* 89.2 (Oct. 1966). Publisher: IOP Publishing, p. 373. ISSN: 0370-1328. DOI: 10.1088/0370-1328/89/2/317. URL: https://iopscience.iop.org/article/10.1088/0370-1328/89/2/317/meta (visited on 09/14/2022).

[36] Alex Chen, Steven Freear, and David Cowell. "Measurement of solid in liquid content Using Ultrasound Attenuation". In: Jan. 2007.

[37] Bradley E. Treeby and B. T. Cox. "k-Wave: MATLAB toolbox for the simulation and reconstruction of photoacoustic wave fields". eng. In: *Journal of Biomedical Optics* 15.2 (Apr. 2010), p. 021314. ISSN: 1560-2281. DOI: 10.1117/1.3360308.

[38] E. Newton Harvey. "THE EFFECT OF HIGH FREQUENCY SOUND WAVES ON HEART MUSCLE AND OTHER IRRITABLE TISSUES". en. In: *American Journal of Physiology-Legacy Content* (Dec. 1929). Publisher: American Physiological Society. DOI: 10.1152/ajplegacy.1929.91.1.284. URL: https://journals.physiology.org/doi/10.1152/ajplegacy.1929.91.1.284 (visited on 09/17/2022).

[39] W. J. Fry et al. "Production of Focal Destructive Lesions in the Central Nervous System With Ultrasound". en_US. In: *Journal of Neurosurgery* 11.5 (Sept. 1954). Publisher: Journal of Neurosurgery Publishing Group Section: Journal of Neurosurgery, pp. 471–478. DOI: 10.3171/jns.1954.11.5.0471. URL: https://thejns.org/view/journals/j-neurosurg/11/5/article-p471.xml (visited on 09/17/2022).

[40] J E Kennedy, G R ter Haar, and D Cranston. "High intensity focused ultrasound: surgery of the future?" In: *The British Journal of Radiology* 76.909 (Sept. 2003). Publisher: The British Institute of Radiology, pp. 590–599. ISSN: 0007-1285. DOI: 10.1259/bjr/17150274. URL: https://www.birpublications.org/doi/full/10.1259/bjr/17150274 (visited on 09/17/2022).

[41] Tony R. Wang, Rob Dallapiazza, and W. Jeff Elias. "Neurological applications of transcranial high intensity focused ultrasound". In: *International Journal of Hyperthermia* 31.3 (Apr. 2015). Publisher: Taylor & Francis _eprint: https://doi.org/10.3109/02656736.2015.1007398, pp. 285–291. ISSN: 0265-6736. DOI: 10.3109/02656736.2015.1007398. URL: https://doi.org/10.3109/02656736.2015.1007398 (visited on 09/17/2022).

[42] Yi-Hsuan Hsiao et al. "Clinical Application of High-intensity Focused Ultrasound in Cancer Therapy". In: *Journal of Cancer* 7.3 (Jan. 2016), pp. 225–231. ISSN: 1837-9664. DOI: 10.7150/jca.13906. URL: https://www.ncbi.nlm.nih.gov/pmc/articles/PMC4747875/ (visited on 09/17/2022).

[43] R. Amin Viren. "DSpace Angular Universal". In: (1989). URL: https://dr.lib.iastate.edu/entities/publication/db59bf2a-30fd-4a4c-92bf-0e3800c8dc72 (visited on 09/13/2022).

[44] Mickael Tanter and Mathias Fink. "Ultrafast imaging in biomedical ultrasound". eng. In: *IEEE transactions on ultrasonics, ferroelectrics, and frequency control* 61.1 (Jan. 2014), pp. 102–119. ISSN: 1525-8955. DOI: 10.1109/TUFFC.2014.6689779.

[45] Stephen A. Lee, Hermes A. S. Kamimura, and Elisa E. Konofagou. "Displacement imaging during focused ultrasound median nerve modulation: A preliminary study in human pain sensation mitigation". In: *IEEE transactions on ultrasonics, ferroelectrics, and frequency control* 68.3 (Mar. 2021), pp. 526–537. ISSN: 0885-3010. DOI: 10.1109/TUFFC.2020.3014183. URL: https://www.ncbi.nlm.nih.gov/pmc/articles/PMC7858702/ (visited on 09/15/2022).

[46] Cyrus R. Safinya and Joachim O. Rädler, eds. *Handbook of Lipid Membranes: Molecular, Functional, and Materials Aspects*. Boca Raton: CRC Press, Sept. 2021. ISBN: 978-0-429-19407-8. DOI: 10.1201/9780429194078.

[47] Jakob Andersson et al. "A tethered bilayer lipid membrane that mimics microbial membranes". en. In: *Physical Chemistry Chemical Physics* 20.18 (May 2018). Publisher: The Royal Society of Chemistry, pp. 12958–12969. ISSN: 1463-9084. DOI: 10.1039/C8CP01346B. URL: http://pubs.rsc.org/en/content/articlelanding/2018/cp/c8cp01346b (visited on 09/08/2022).

[48] Bernhard Schuster et al. "Self-assembled -hemolysin pores in an S-layer-supported lipid bilayer". en. In: *Biochimica et Biophysica Acta (BBA) - Biomembranes* 1370.2 (Mar. 1998), pp. 280–288. ISSN: 0005-2736. DOI: 10.1016/S0005-2736(97)00274-5. URL: https://www.sciencedirect.com/science/article/pii/S0005273697002745 (visited on 09/08/2022).

[49] Katherine Henzler-Wildman and Dorothee Kern. "Dynamic personalities of proteins". en. In: *Nature* 450.7172 (Dec. 2007). Number: 7172 Publisher: Nature Publishing Group, pp. 964–972. ISSN: 1476-4687. DOI: 10.1038/nature06522. URL: http://www.nature.com/articles/nature06522 (visited on 09/17/2022).

[50] Tsai-Wen Chen et al. "Ultrasensitive fluorescent proteins for imaging neuronal activity". en. In: *Nature* 499.7458 (July 2013). Number: 7458 Publisher: Nature Publishing Group, pp. 295–300. ISSN: 1476-4687. DOI: 10.1038/nature12354. URL: http://www.nature.com/articles/nature12354 (visited on 05/30/2022).

[51] Allen J. Bard and Larry R. Faulkner. *Electrochemical methods fundamentals and applications*. New York u.a.: Wiley, 1980.

[52] Cynthia G. Zoski. *Handbook of electrochemistry*. Amsterdam: Elsevier, 2007.

[53] Shannon W. Boettcher et al. "Potentially Confusing: Potentials in Electrochemistry". In: *ACS Energy Letters* 6.1 (Jan. 2021). Publisher: American Chemical Society, pp. 261–266. DOI: 10.1021/acsenergylett.0c02443. URL: https://doi.org/10.1021/acsenergylett.0c02443 (visited on 08/30/2022).

[54] Donald A. Neamen and Dhrubes Biswas. *Semiconductor physics and devices*. McGraw Hill Education (India), 2020.

[55] S. Mischler and A. I. Munoz. "Tribocorrosion". en. In: *Encyclopedia of Interfacial Chemistry*. Ed. by Klaus Wandelt. Oxford: Elsevier, Jan. 2018, pp. 504–514. ISBN: 978-0-12-809894-3. DOI: 10.1016/B978-0-12-409547-2.13424-9. URL: https://www.sciencedirect.com/science/article/pii/B9780124095472134249 (visited on 09/01/2022).

[56] E. D. Verink. "Simplified procedure for constructing Pourbaix diagrams". In: *Uhlig's corrosion handbook* 7 (2011). Publisher: John Wiley & Sons Inc. Hoboken, New Jersey, pp. 111–124.

[57] Sreejith Kaniyankandy et al. "Electrodeposition of silver nanodendrites". en. In: *Nanotechnology* 18.12 (Feb. 2007). Publisher: IOP Publishing, p. 125610. ISSN: 0957-4484. DOI: 10.1088/0957-4484/18/12/125610. URL: https://doi.org/10.1088/0957-4484/18/12/125610 (visited on 06/17/2022).

[58] Jack W. Dini and Dexter D. Snyder. "Electrodeposition of Copper". In: *Modern Electroplating*. John Wiley & Sons, Inc. : Hoboken, NJ, USA, 2011, pp. 33–78. ISBN: 978-0-470-60263-8 978-0-470-16778-6.

[59] Ian Gibson et al. *Additive Manufacturing Technologies*. en. Cham: Springer International Publishing, 2021. ISBN: 978-3-030-56126-0 978-3-030-56127-7. DOI: 10.1007/978-3-030-56127-7. URL: https://link.springer.com/10.1007/978-3-030-56127-7 (visited on 09/12/2022).

[60] Ismo Rauha et al. "Chemical Compatibility of Fused Filament Fabrication-based 3-D Printed Components with Solutions Commonly Used in Semiconductor Wet Processing". In: *Additive Manufacturing* 23 (July 2018), pp. 99–107. DOI: 10.1016/j.addma.2018.07.015.

[61] Brian J. Polk et al. "Ag/AgCl microelectrodes with improved stability for microfluidics". en. In: *Sensors and Actuators B: Chemical* 114.1 (2006), pp. 239–247. ISSN: 0925-4005. DOI: 10.1016/j.snb.200

5.03.121. URL: https://www.sciencedirect.com/science/article/pii/S0925400505004612 (visited on 02/09/2022).

[62] Niels Burghoorn. *EVA*. original-date: 2022-06-23T12:13:07Z. Aug. 2022. URL: https://github.com/SwaggerNiels/EVA (visited on 09/29/2022).

[63] Jean-Baptiste Jorcin et al. "CPE analysis by local electrochemical impedance spectroscopy". en. In: *Electrochimica Acta*. Electrochemical Impedance Spectroscopy 51.8 (Jan. 2006), pp. 1473–1479. ISSN: 0013-4686. DOI: 10.1016/j.electacta.2005.02.128. URL: https://www.sciencedirect.com/science/article/pii/S0013468605008285 (visited on 10/01/2022).

[64] Christian J. Braun et al. "Pseudo painting/air bubble technique for planar lipid bilayers". en. In: *Journal of Neuroscience Methods* 233 (Aug. 2014), pp. 13–17. ISSN: 0165-0270. DOI: 10.1016/j.jneumeth.2014.05.031. URL: https://www.sciencedirect.com/science/article/pii/S016502701400199X (visited on 09/28/2022).

[65] Yumpu.com. *SU-8 2000 Data Sheet (2000.5-2015) - MicroChem*. en. URL: https://www.yumpu.com/en/document/view/18090977/su-8-2000-data-sheet-20005-2015-microchem (visited on 10/05/2022).

[66] *Resistivity Table / Chart for Common Materials | Electronics Notes*. URL: https://www.electronics-notes.com/articles/basic_concepts/resistance/electrical-resistivity-table-materials.php (visited on 10/05/2022).

[67] Bo Fan, Bernhard Wolfrum, and Jacob T. Robinson. "Impedance scaling for gold and platinum microelectrodes". en. In: *Journal of Neural Engineering* 18.5 (Sept. 2021). Publisher: IOP Publishing, p. 056025. ISSN: 1741-2552. DOI: 10.1088/1741-2552/ac20e5. URL: https://doi.org/10.1088/1741-2552/ac20e5 (visited on 07/22/2022).

[68] XINGHUI MENG and KENNETH N. HAN. "The Principles and Applications of Ammonia Leaching of Metals—A Review". In: *Mineral Processing and Extractive Metallurgy Review* 16.1 (Jan. 1996). Publisher: Taylor & Francis _eprint: https://doi.org/10.1080/08827509608914128, pp. 23–61. ISSN: 0882-7508. DOI: 10.1080/08827509608914128. URL: https://doi.org/10.1080/08827509608914128 (visited on 10/05/2022).

[69] Firouzeh Sabri et al. "In Vivo Ultrasonic Detection of Polyurea Crosslinked Silica Aerogel Implants". In: *PloS one* 8 (June 2013), e66348. DOI: 10.1371/journal.pone.0066348.

[70] Min-Kyoo Song and Kyung-Young Jhang. "Crack Detection in Single-Crystalline Silicon Wafer Using Laser Generated Lamb Wave". In: *Advances in Materials Science and Engineering* 2013 (Jan. 2013), pp. 1–6. DOI: 10.1155/2013/950791.

[71] Anton Fomenko et al. "Low-intensity ultrasound neuromodulation: An overview of mechanisms and emerging human applications". en. In: *Brain Stimulation* 11.6 (Nov. 2018), pp. 1209–1217. ISSN: 1935-861X. DOI: 10.1016/j.brs.2018.08.013. URL: https://www.sciencedirect.com/science/article/pii/S1935861X18302961 (visited on 05/19/2021).

[72] Sangjin Yoo et al. "Focused ultrasound excites neurons via mechanosensitive calcium accumulation and ion channel amplification". en. In: *bioRxiv* (May 2020). Publisher: Cold Spring Harbor Laboratory Section: New Results, p. 2020.05.19.101196. DOI: 10.1101/2020.05.19.101196. URL: https://www.biorxiv.org/content/10.1101/2020.05.19.101196v1 (visited on 05/19/2021).

[73] Michael D. Martin et al. "MEMS Stabilized Lipid Membranes and Their Parylene Encapsulation". In: *Journal of Microelectromechanical Systems* 26.3 (June 2017). Conference Name: Journal of Microelectromechanical Systems, pp. 662–670. ISSN: 1941-0158. DOI: 10.1109/JMEMS.2017.2688705.

[74] Michele Zagnoni. "Miniaturised technologies for the development of artificial lipid bilayer systems". en. In: *Lab on a Chip* 12.6 (Feb. 2012). Publisher: The Royal Society of Chemistry, pp. 1026–1039. ISSN: 1473-0189. DOI: 10.1039/C2LC20991H. URL: http://pubs.rsc.org/en/content/articlelanding/2012/lc/c2lc20991h (visited on 09/13/2021).

A

Fabrication

A.1. 3D printing parameters

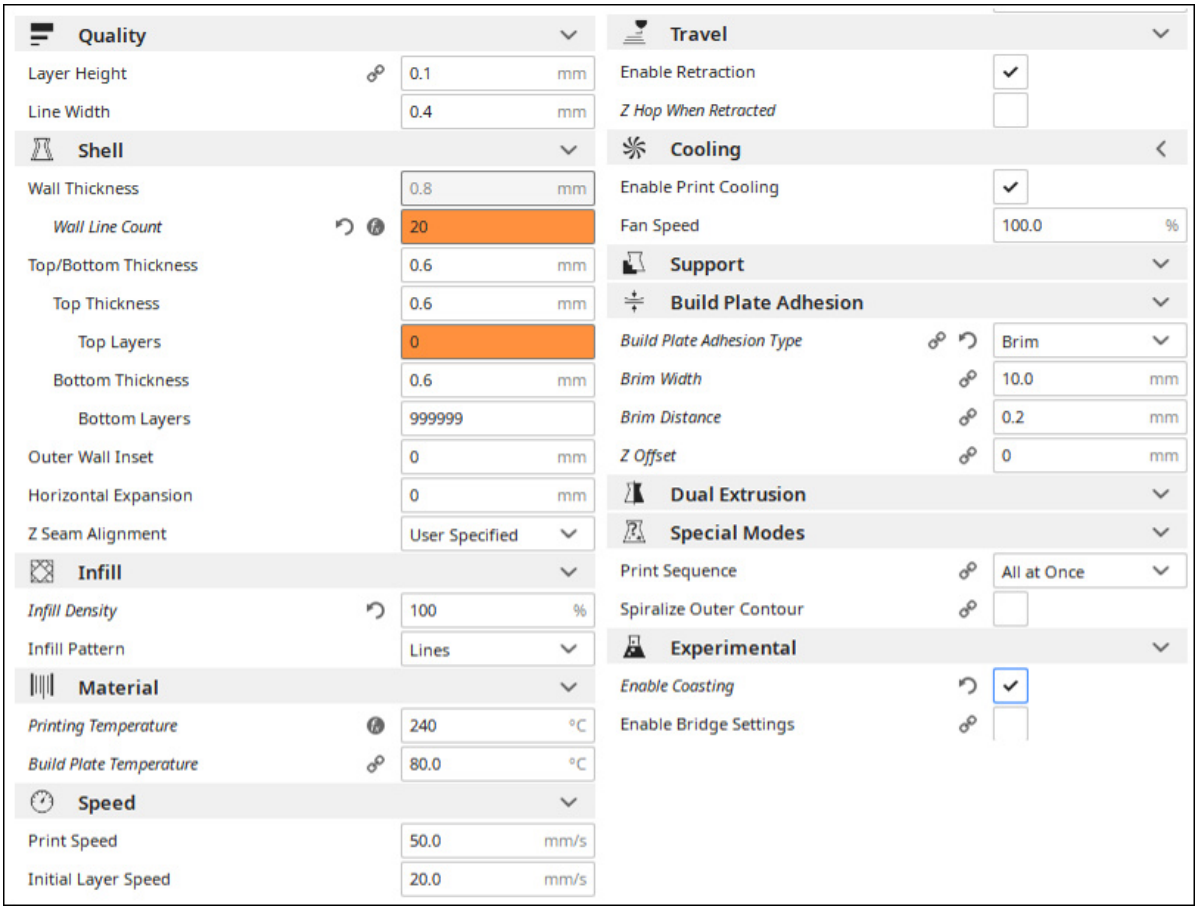

Figure A.1: The settings of the 3D slicing software CURA. These were used for printing the polypropylene scaffolds. These parameters are optimised for the Ender-3 PRO for small 100% filled detailed parts.

A.2. Chemical exposure tests

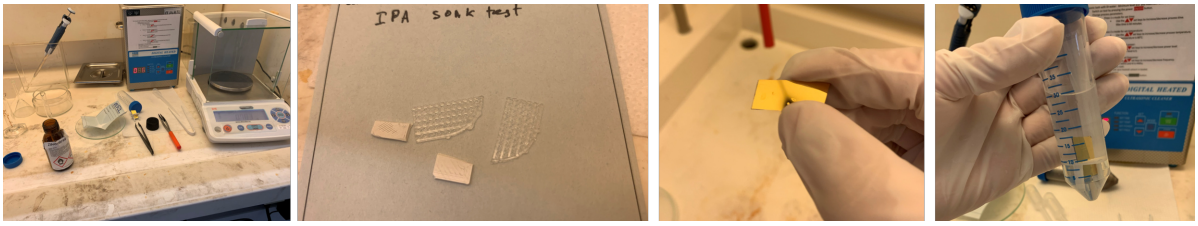

Figure A.2: Chemical exposure tests of 1M NH_3(aq), 1M HCl(aq), IPA were performed on PLA and polypropylene printed parts.

A.3. SEM

The parameters used during image acquisition of the SEM system.

Table A.1: SEM system parameters

Setting	Value
DataSize	1280x960
PixelSize	66.14584
SignalName	SE(U)
DisplaySignalName	SE(U)
AcceleratingVoltage	10000 Volt
DecelerationVoltage	0 Volt
Magnification	1500
WorkingDistance	12604.88 um
EmissionCurrent	27000 nA
LensMode	High
PhotoSize	1000
MicronMarker	30000
SpecimenBias	0 V
ScanSpeed	Capture CSS(20)
CalibrationScanSpeed	25
Condition	Vacc
Mag	x1.50k
WD	12.6mm
DataDisplayCombine	0
StageType	5
StagePositionX	28277000
StagePositionY	54139000
StagePositionR	180
StagePositionZ	8000000
StagePositionT	0
FocusDepth	1

A.4. Electrodeposits

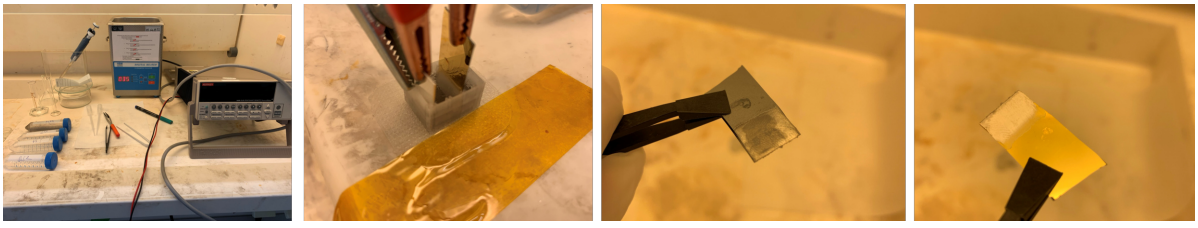

Figure A.3: Electrodeposition tests were performed on gold seed layer.

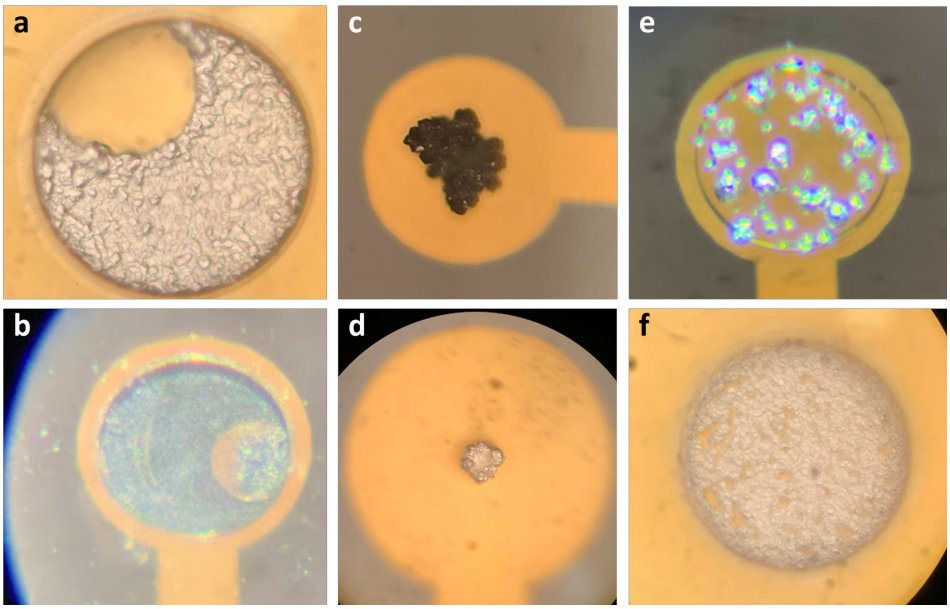

Figure A.4: Failed electrodeposition of batch two chips. *(a,b)* The electrodeposition profile when air bubbles were not properly removed. *(c,d)* The electrodeposition growth was seen when a high current was provided. The deposits surpass the microwell edges and form crystal-shaped structures. *(e,f)* Pillars or holes in the electrodeposition.

Table A.2: Total charge in mC transferred to chips of wafer 2 through 4 for microwell diameters 30μm through 100μm. during electrodeposition. This value is calculated by integrating the measured current traces obtained during the separate electrodepositions.

	microwell diameter		
wafer	30μ m	50μ m	100μ m
2	0.996	0.999	1.797
3	0.996	0.996	2.196
4	4.191	4.256	4.191

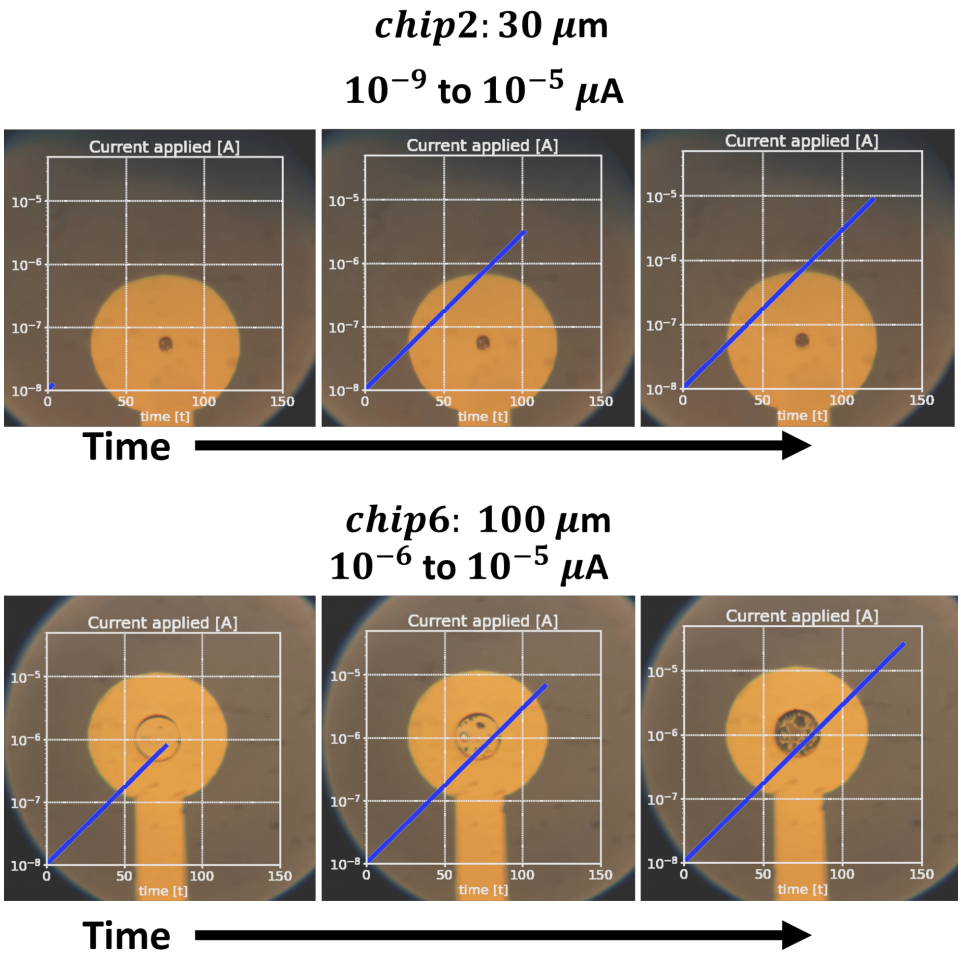

Figure A.5: Electrodeposition of batch two chip 2 with 30μm microwell diameter with preemptive deposition and little to no change in visual deposition profile. Electrodeposition of batch two chip 5 with 100μm microwell diameter with pillar deposition.

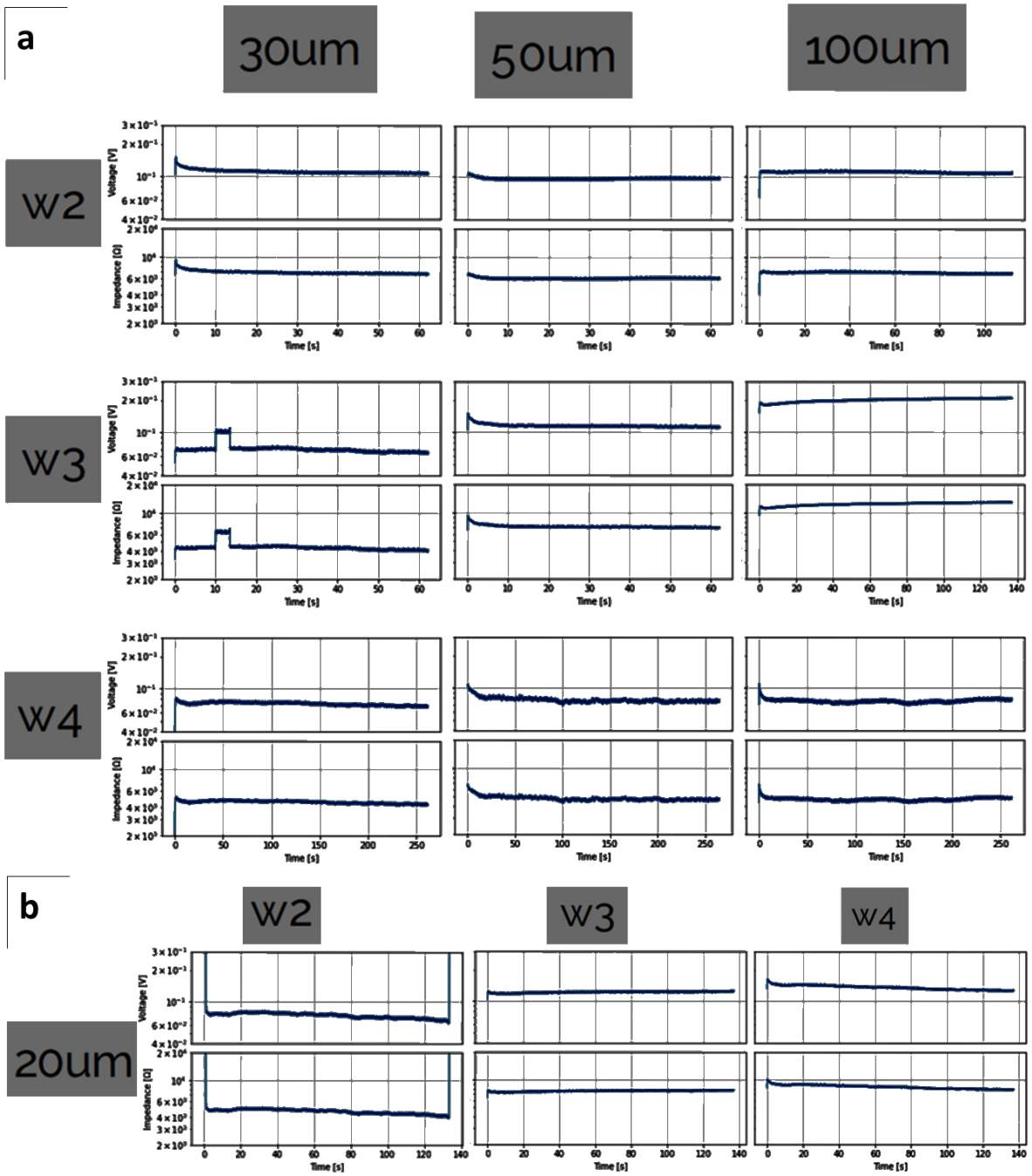

Figure A.6: The voltage and impedance traces of all electrodepositions of the chips of wafer 2 through 4 for microwell diameters 20μm through 100μm. The accompanying line height profiles for microwell diameters > 30μm are shown in Figure 4.6. The traces were recorded with a Keithley 6430 Sub-Femtoamp Remote SourceMeter.

B

Ultrasound

B.1. Ultrasound profile of early measurements

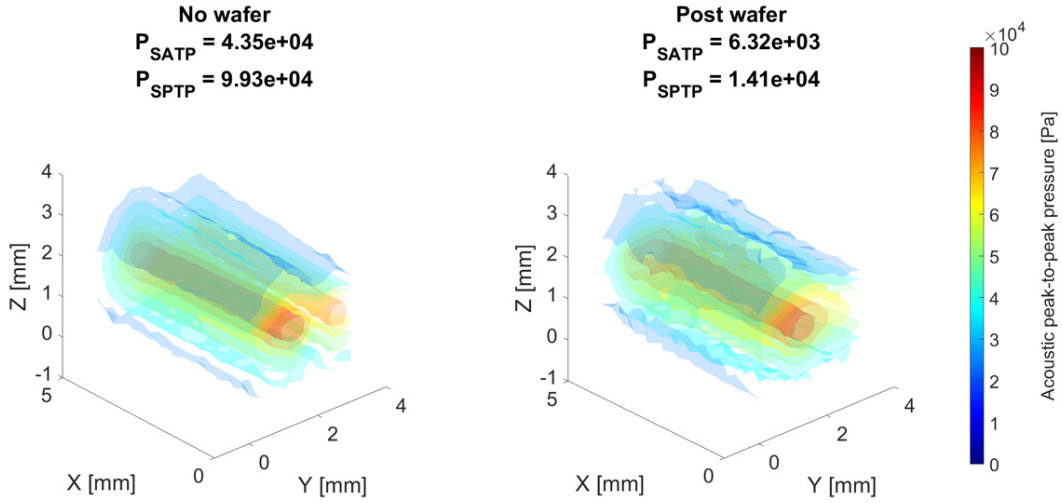

Figure B.1: The unobstructed US profile of the PZT transducer used in measurements before the design of the platform.

B.2. Ultrasound profiles of unobstructed transducer

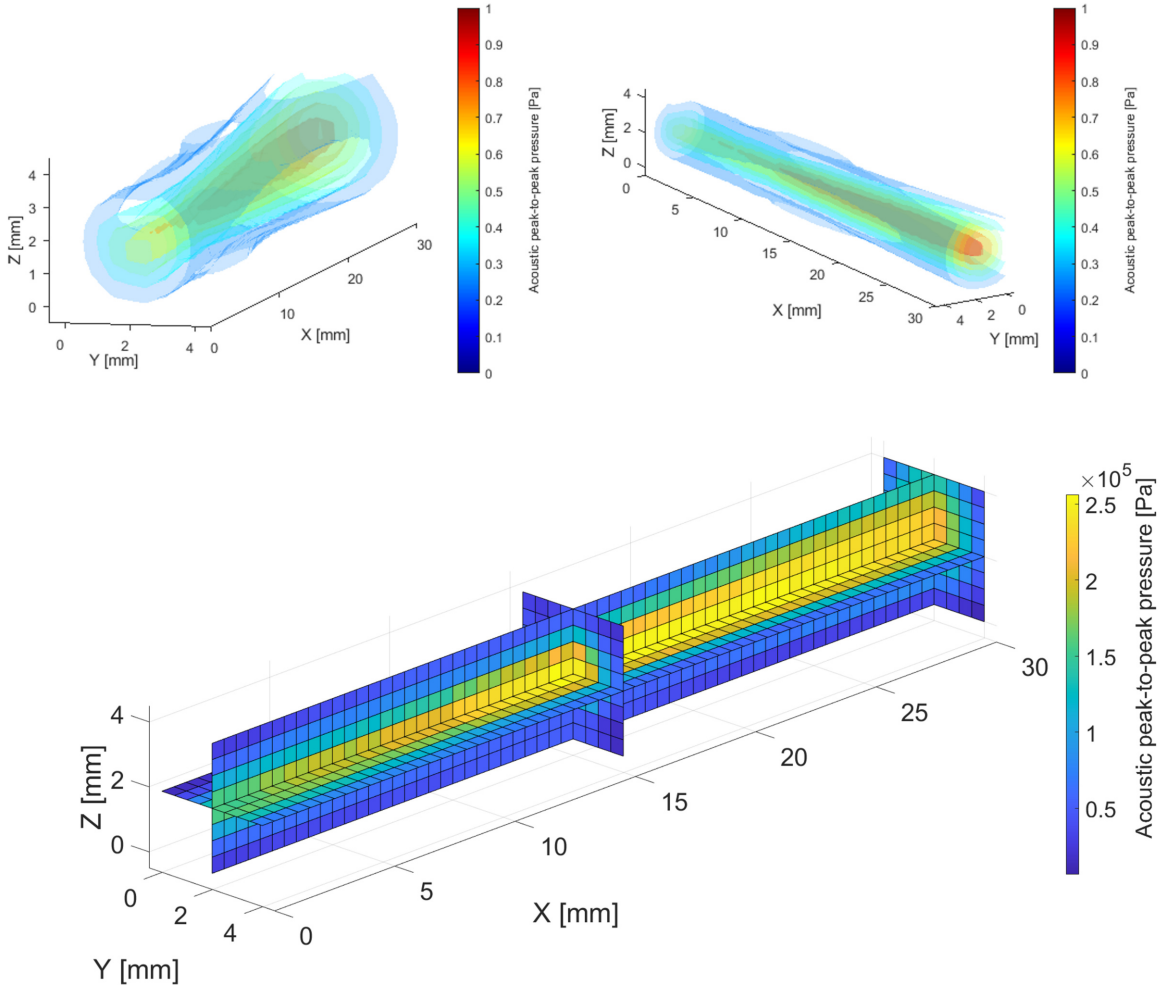

Figure B.2: The unobstructed US profile of the PZT transducer used for US stimulation. The same information is shown in 3 different settings in order to appreciate the 3D intensity profile.

B.3. Ultrasound signal form

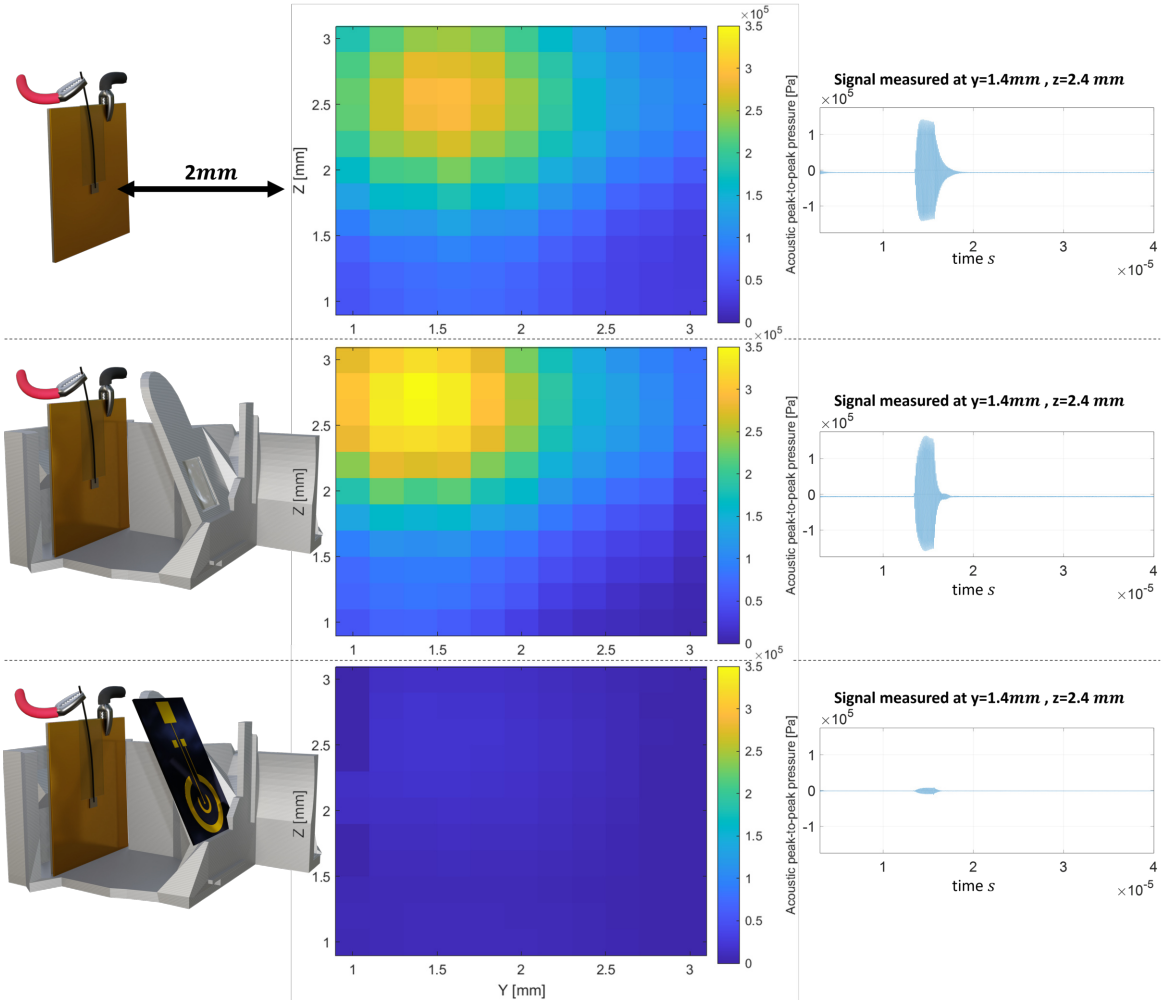

Figure B.3: The true-to-scale comparison of the acoustic signals presented in Figure 4.11.

C

Electrophysiology

C.1. Gold electrodes time dependency

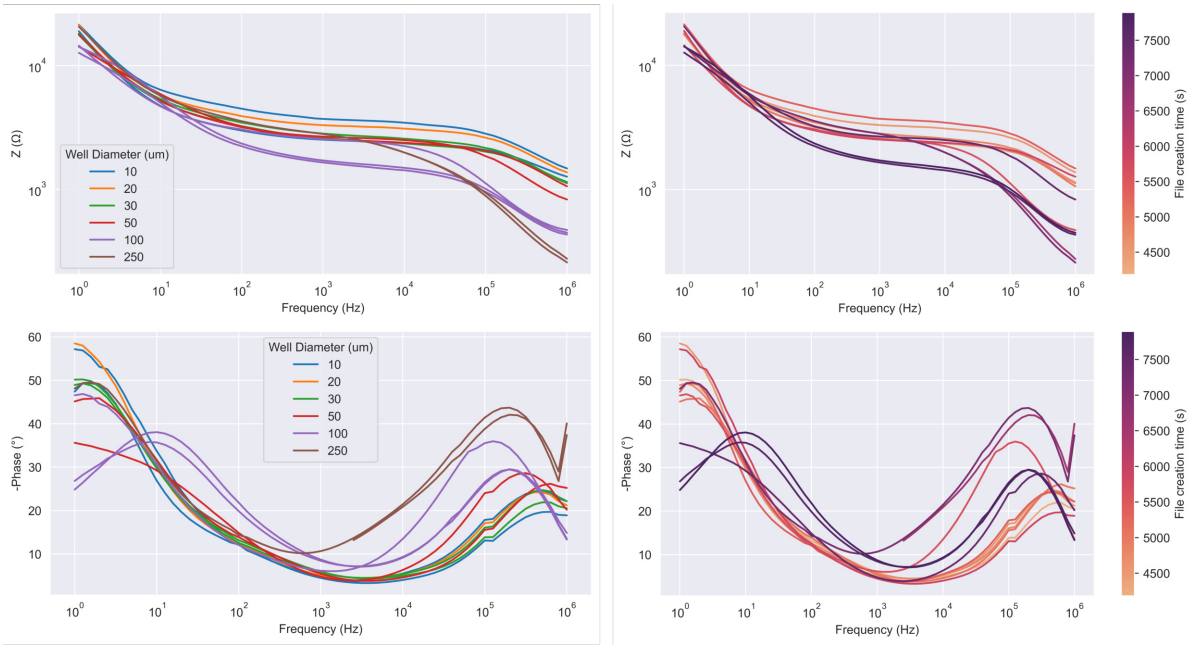

Figure C.1: The EIS bode plot results of the various microwell sizes. A 10mV sinusoidal signal relative to the REF was applied. The signal frequency was swept from 1MHz to 1Hz with 10 measured points per decade. The colours as indicated in the legend show relate to the microwell diameter dimension. The lines present the impedance data, while the points indicate the negative phase delay for each measured frequency.

C.2. Membrane optical confirmation

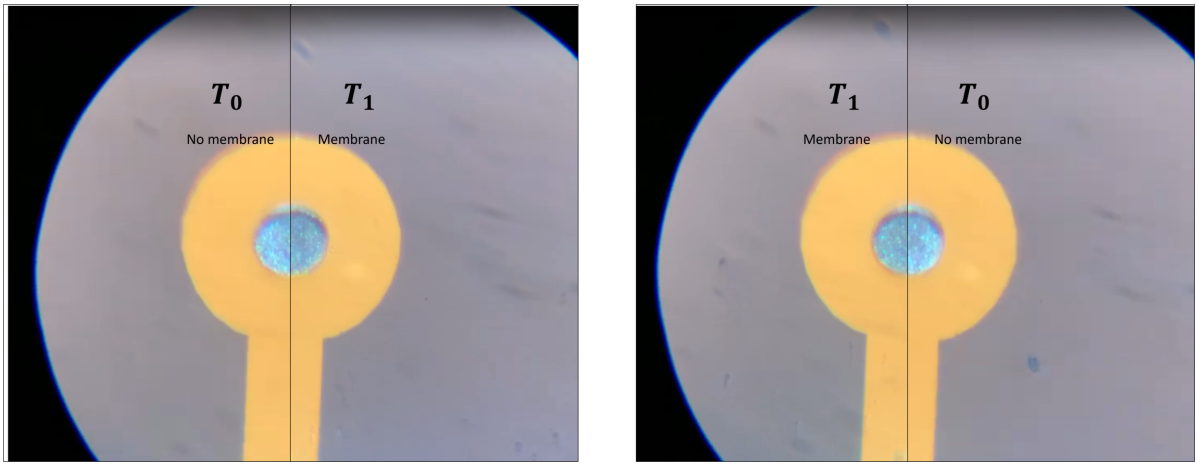

Figure C.2: *(Left)* Clipped images acquired with the microscopy setup were taken before (T_0, left) and after (T_1, right) a membrane was established. The images show the discolouration seen at 100μm diameter microwell after a seal was electrically registered. *(Right)* The same images with swapped snapshot sides.

D

Code

D.1. Ultrasound simulation code

The following code was used to simulate the acoustic pressures in 2D. This was done using MATLAB k-wave.

```
clear all
close all
PLOTMAT = false;
PLOTSRC = false;

materials_file = 'materials/mat_fSi';
mat_file_postfix = '_halfway';
source_file = 'sources/src_fSi';

%% Media
% Initialize all materials from image to a material mask (mm)
materials = table2cell(readtable(strcat(materials_file,'.xlsx')));
matObj = MaterialMask(strcat(materials_file,mat_file_postfix,'.png'), ...
    materials,PLOTMAT);

%% Kgrid
dd = 50e-6;
Nt = 2e4;
dt  = 5e-10;

[kgrid, medium, sensor] = MakeMaterialGrid(matObj.mm, dd, Nt, dt);

%% Source
source = SourceMask(strcat(source_file,'.png'),PLOTSRC);
source_freq = 9e6;       % [Hz]
source_mag = 5e5*.72;         % [Pa]
source.p = source_mag * sin(2 * pi * source_freq * kgrid.t_array);

% filter the source to remove any high frequencies not supported by the grid
source.p = filterTimeSeries(kgrid, medium, source.p);

%% Run the simulation
try
    sensor_data = kspaceFirstOrder2DG(kgrid, medium, source, sensor, 'PMLInside', false);
end

%% Plotting
close all

x_lb = 1.35e-3;
t_lb = 0%.3e-6;

% PlotMaterialField(kgrid, matObj, sensor_data.p, 200, 'animation.gif', x_lb, t_lb);
% PlotMaterialField(kgrid, matObj, sensor_data.ux, 500, '');
```

```
PlotMaterialFieldProperty(kgrid, matObj, sensor_data.p_max, 'P max', x_lb, 1);
% PlotMaterialFieldProperty(kgrid, matObj, sensor_data.p_final, 'P final');
```

D.2. Electrochemistry data class code

The following code was used in conjunction with 3 other custom Python scripts although this is too lengthy for appending. The main data processing and visualisation are done with this class. It also allows for the visualisation of electrochemical equivalent circuits by using interactive plots with user-specified circuit components.

```
import warnings
warnings.simplefilter(action='ignore', category=FutureWarning)
warnings.simplefilter(action='ignore', category=UserWarning)
import pandas as pd
import seaborn as sns
import matplotlib.pyplot as plt
from IPython.display import display
from ipywidgets import interact,widgets
import numpy as np
import regex as re
from math import log10,pow
from impedance.models.circuits import CustomCircuit,plot_nyquist
sns.set_style('darkgrid', {'legend.frameon':False})
import matplotlib as mpl
mpl.rcParams['figure.dpi']= 100
# plt.rcParams["figure.figsize"] = (10,10)

fn = 'Filename' #default hue
ft = 'File creation time (s)' #default hue
DEBUG = 0
PADDING = .1
XPADDING = PADDING
YPADDING = PADDING

class data():
    def __init__(self, df : pd.DataFrame, columns,  parameter_names):
        self.df = df
        self.columns = columns
        self.short_code = {}
        for k, v in columns.items():
            setattr(self, k, v)
            self.short_code[v] = str(k)

        self.parameter_names = parameter_names
        self.parameters = [tuple(sorted(df[name].unique())) for name in parameter_names]
        self.N = len(self.parameters)

        self.palette = 'tab10'

        parameters_string = '\n\t'.join([f'{pn:>20} : {str(pv):<10}' for pn,pv in
                                         zip(parameter_names,self.parameters)])
        print(f'___Parameters options___\n\t{parameters_string}')

    def __getitem__(self, item):
        df = self.df
        print(f'Initial files: {len(df[self.fn].unique())}')
        for selection,parameter,parameter_name in zip(item,self.parameters,self.
            parameter_names):

            if isinstance(selection, slice):
                a = selection.start
                b = selection.stop
                c = selection.step

                assert(a in parameter or a==None)
                assert(b in parameter or b==None)
                if a!=None and b!=None:
                    assert(a < b)
                if c!=None:
```

```
                    assert(c//self.N-1 == selection.step/self.N-1)

                if a==None and b==None:
                    slicing = slice(None,None,c)
                elif a==None:
                    slicing = slice(None,parameter.index(b),c)
                elif b==None:
                    slicing = slice(parameter.index(a),None,c)
                else:
                    slicing = slice(parameter.index(a),parameter.index(b),c)

                start = slicing.start if slicing.start!=None else ':'
                stop = slicing.stop if slicing.stop!=None else ':'
                step = slicing.step if slicing.step!=None else ':'
                slice_string = f'[{start},{stop},{step}]'

                slicing = parameter[slicing]

            elif isinstance(selection, int):
                assert(selection in parameter)
                slicing = [selection]
                slice_string = f'{slicing}'

            elif isinstance(selection, bool):
                slicing = [selection]
                slice_string = f'{slicing}'

            elif isinstance(selection, str):
                slicing = [selection]
                slice_string = f'{slicing}'
            else:
                print(f'Incorrect format: {type(selection)}, please specify accoding to the parameters:\n{self.parameters}')
                return(None)

            df = df[df[parameter_name].isin(slicing)]
            print(f'{parameter_name:>20}{slice_string:>10} --> {len(df[self.fn].unique())}')

        return(data(df,self.columns, self.parameter_names))

    def _set_scale(self, plot_obj : plt.Axes, axis='x', extends=None, kind='lin'):
        if DEBUG: print(f'_set_scale called: ({axis},{extends},{kind})')

        if kind == 'lin':
            linpad_lims = lambda a,x : (a[0]-x*(a[1]-a[0]),a[1]+x*(a[1]-a[0]))
            lims = lambda padding : linpad_lims(extends,padding)
            kind = 'linear'
        elif kind == 'log':
            logpad_lims = lambda a,x : (pow(10,log10(a[0])-x),pow(10,log10(a[1])+x))
            lims = lambda padding : logpad_lims(extends,padding)
            kind = 'log'

        if axis == 'x':
            plot_obj.set_xscale(kind)
            if extends != None :
                plot_obj.set_xlim(lims(XPADDING))
                if len(extends) == 3 :
                    if kind=='log' : plot_obj.xaxis.set_ticks(np.logspace(log10(extends[0]),
                        log10(extends[1]), extends[2]))
                    if kind=='linear' : plot_obj.xaxis.set_ticks(np.linspace(extends[0],
                        extends[1], extends[2]))
        elif axis == 'y':
            plot_obj.set_yscale(kind)
            if extends != None :
                plot_obj.set_ylim(lims(YPADDING))
                if len(extends) == 3 :
                    if kind=='log' : plot_obj.yaxis.set_ticks(np.logspace(log10(extends[0]),
                        log10(extends[1]), extends[2]))
                    if kind=='linear' : plot_obj.yaxis.set_ticks(np.linspace(extends[0],
                        extends[1], extends[2]))

```

```
125     def trace(self, hue=fn, style=None):
126         p = sns.lineplot(data=self.df,x=self.freq,y=self.zmag,
127                          hue=hue, style=style,
128                          palette=self.palette,
129                          estimator=None, units=self.fn)
130 
131     def plot(self,kind='bode',hue=fn,style=None,xlim=None,ylim=None):
132         args = {
133             hue : hue,
134             style : style,
135             }
136 
137         if hue==ft:
138             self.palette = 'flare'
139             norm = plt.Normalize(self.df[ft].min(), self.df[ft].max())
140             sm = plt.cm.ScalarMappable(cmap=self.palette, norm=norm)
141             sm.set_array([])
142 
143         # plt.ioff()
144         if kind=='bode':
145             p = self._plot_bode(*args)
146             scaling = None
147 
148             ax1,ax2 = p.axes
149             if ylim == None: ylim = (None,None)
150             for scale,axis,extends in (('log','x',xlim),('log','y',ylim[0])):
151                 self._set_scale(plot_obj=ax1,axis=axis,extends=extends,kind=scale)
152             for scale,axis,extends in (('log','x',xlim),('lin','y',ylim[1])):
153                 self._set_scale(plot_obj=ax2,axis=axis,extends=extends,kind=scale)
154 
155             # ax1.legend(frameon=False)
156             # ax2.legend(frameon=False)
157         else:
158             if kind=='zmag':
159                 p,scaling = self._plot_zmag(*args)
160             elif kind=='phase' :
161                 p,scaling = self._plot_phase(*args)
162             elif kind=='nyquist':
163                 p,scaling = self._plot_nyquist(*args)
164 
165             for scale,axis,extends in ((scaling[:3],'x',xlim),(scaling[3:],'y',ylim)):
166                 self._set_scale(plot_obj=p,axis=axis,extends=extends,kind=scale)
167 
168             # p.legend(framealpha=0.4)
169 
170         if hue==ft:
171             if style != None:
172                 handles,labels = p.get_legend_handles_labels()
173                 labels_numeric = [self.is_float(label)==False for label in labels[1:]]
174                 style_index = np.where(labels_numeric)[0][0]+1
175 
176             p.get_legend().remove()
177 
178             if style != None:
179                 plt.legend(handles[style_index:],labels[style_index:])
180 
181             p.figure.colorbar(sm, label=ft)
182 
183         self.print_name(kind)
184         # plt.ion()
185         # p.show()
186 
187         return(p)
188 
189     def _plot_zmag(self, hue=None, style=None):
190         # p = sns.scatterplot(data=self.df, x=self.freq, y=self.zmag,
191         #                 hue=hue, style=style, palette=self.palette)
192         p = sns.lineplot(data=self.df,x=self.freq,y=self.zmag,
193                          hue=hue, style=style,
194                          palette=self.palette,
195                          estimator=None, units=self.fn)
```

```
196         return(p,'loglog')
197 
198     def _plot_phase(self, hue=None, style=None,):
199         p = sns.scatterplot(data=self.df, x=self.freq, y=self.phase,
200                         hue=hue, style=style, palette=self.palette)
201         return(p,'loglin')
202 
203     def _plot_nyquist(self, hue=None, style=None,):
204         p = sns.scatterplot(data=self.df, x=self.zre, y=self.zim,
205                         hue=hue, style=style, palette=self.palette)
206         return(p,'linlin')
207 
208     def _plot_bode(self, hue=None, style=None,):
209         fig, ax1 = plt.subplots()
210         sns.lineplot(data=self.df,x=self.freq,y=self.zmag,
211                         hue=hue, style=style, ax=ax1,
212                         palette=self.palette, legend=False,
213                         estimator=None, units=self.fn)
214         ax2 = plt.twinx()
215         sns.scatterplot(data=self.df,x=self.freq,y=self.phase,
216                         hue=hue, style=style, ax=ax2,
217                         palette=self.palette)
218         fig.legend(['lines: ' + self.zmag,'scatter: ' + self.phase],
219                    handletextpad=0.0, handlelength=0, bbox_to_anchor=(1,1.1))
220         return(fig)
221 
222     def fit(self, circuit, guess, constants=None):
223 
224         #for each file do a fit with the provided circuit and guess
225         circuit_objs = []
226         for file_group in self.df.groupby(fn):
227             file_name,file_data = file_group
228             f = np.asarray(file_data[self.freq]).flatten()
229             z = np.asarray(file_data[self.zre ] - 1j*file_data[self.zim ]).flatten().T
230 
231             trace = (f,z)
232             circuit_obj = self._fit_trace(trace,circuit,guess,constants)
233 
234             circuit_obj.f = f
235             circuit_obj.z = z
236             #residual calculated as: (measured-predicted)/abs(measured)
237             circuit_obj.res_real = (z - circuit_obj.predict(f)).real/np.abs(z)
238             circuit_obj.res_imag = (z - circuit_obj.predict(f)).imag/np.abs(z)
239 
240             circuit_obj.elements = circuit_obj.get_param_names()[0]
241 
242             element_names = circuit_obj.get_param_names()[0]
243             for element_name,fit_value in zip(element_names,circuit_obj.parameters_):
244                 setattr(circuit_obj, element_name, fit_value)
245 
246             #add plot function
247             plot_function = lambda f=f,z=z : circuit_obj.plot(f_data=f,Z_data=z)
248             circuit_obj.show = plot_function
249 
250             circuit_objs.append(circuit_obj)
251 
252         #unpack all the circuit elements and their values per file
253         #and label the file parameters and file name for each fit
254         #dataframe will have columns with:
255         #filename, *parameters, *circuit element fitted values
256         fit_df = self.df[[fn, *self.parameter_names]].groupby(fn).first()
257         fit_df = fit_df.reset_index(level=0)
258 
259         element_names = circuit_objs[0].elements
260         for element_name in element_names:
261             fit_df[element_name] = [getattr(obj,element_name) for obj in circuit_objs]
262 
263         # circuit_df = pd.DataFrame(circuit_objs)
264         fit_df['c'] = circuit_objs
265 
266         return(fit_df)
```

```
267
268     def _fit_trace(self, trace, circuit, guess, constants):
269         circuit_obj = CustomCircuit(circuit,
270                                     initial_guess=guess,
271                                     constants=constants,)
272         f,z = trace
273         circuit_obj.fit(frequencies=f, impedance=z)
274         return(circuit_obj)
275
276     def print_name(self, plot_string):
277         short_name = '_'.join([f'{self.short_code[pn]}{pv}' for pn,pv in
278                                zip(self.parameter_names,self.parameters)])
279         print(plot_string + '_' + short_name)
280
281     def circuit_make(self,circuit_string,parameters):
282         circuit = CustomCircuit(circuit_string, initial_guess=parameters)
283         p = self.circuit_show(circuit)
284
285         return(p)
286
287     def circuit_interact(self,circuit_string,initial_values,logrange=[-1,6],extends=None):
288         circuit_obj = CustomCircuit(circuit_string, initial_guess=initial_values)
289         elements = circuit_obj.get_param_names()[0]
290
291         sliders = {
292             widgets.FloatLogSlider(
293                 value=10,
294                 base=10,
295                 min=-9, # max exponent of base
296                 max=9, # min exponent of base
297                 step=0.2, # exponent step
298                 description=element
299             ) for element in elements}
300         ui = widgets.GridBox([*sliders],
301                              layout=widgets.Layout(
302                                  grid_template_columns="repeat(1,␣300px)"
303                                  ))
304         argcouple = dict(zip(elements,sliders))
305
306         def update(**element_values):
307             circuit = CustomCircuit(circuit_string,
308                                     initial_guess=list(element_values.values()))
309             fs = np.logspace(*logrange)
310             Z=circuit.predict(fs)
311             plt.scatter(np.real(Z), -np.imag(Z),c=fs,
312                         norm=mpl.colors.LogNorm())
313             bar = plt.colorbar()
314             bar.set_label('Frequency', rotation=270)
315             plt.xlabel("Z'")
316             plt.ylabel("-Z''")
317             if extends != None:
318                 plt.xlim(extends[0])
319                 plt.ylim(extends[1])
320
321         out = widgets.interactive_output(update, argcouple)
322         display(ui,out)
323
324     def circuit_show(self,circuit,logrange=[-1,6]):
325         fs = np.logspace(*logrange)
326         p = plt.plot(fs,circuit.predict(fs))
327         # p = circuit.plot(f_data=fs,Z_data=circuit.predict(fs))
328
329         if hasattr(circuit,'res_real'):
330             res_re = sum(abs(circuit.res_real))
331             res_im = sum(abs(circuit.res_imag))
332             print(f'Absolute␣residual:␣Re={res_re:1.3e},Im={res_im:1.3e}')
333
334         return(p)
335
336     def circuits_show(self,circuits,logrange=[-1,6]):
337         ps = []
```

```
        for i,circuit in enumerate(circuits):
            print(f'index {i}: ',end='')
            p = self.circuit_show(circuit,logrange)
            ps.append(p)

        return(ps)

    #fit plot function
    def fshow(self,fit_df,x,hue=fn,style=None,N=0,regex_str=None,scale=None):
        element_string = ''.join(fit_df.c[0].elements)
        if 'R_' in element_string:
            fig = self.fplot(fit_df,x,hue=hue,regex_str='(R_[0-9])',scale='linlog')
            plt.show()

        if 'C_' in element_string:
            fig = self.fplot(fit_df,x,hue=hue,regex_str='(C_[0-9])',scale='linlog')
            plt.show()

        if 'CPE_' in element_string:
            fig = self.fplot(fit_df,x,hue=hue,regex_str='(CPE_[0-9]_0)',scale='linlin')
            plt.show()
            fig = self.fplot(fit_df,x,hue=hue,regex_str='(CPE_[0-9]_1)',scale='linlin')
            plt.show()

        if 'W_' in element_string:
            fig = self.fplot(fit_df,x,hue=hue,regex_str='(W(?:[a-z]){0,1}_[0-9]_0)',scale='
                linlog')
            plt.show()

        if 'Wo_' in element_string:
            fig = self.fplot(fit_df,x,hue=hue,regex_str='(W(?:[a-z]){0,1}_[0-9]_1)',scale='
                linlog')
            plt.show()

    def fplot(self,fit_df,x,hue=fn,style=None,N=0,regex_str=None,scale=None):
        y_values = fit_df.c[0].elements
        if regex_str != None:
            y_values = re.findall(regex_str,','.join(y_values))

        if N==0: N = len(y_values)
        if DEBUG: print(f'{N} plots will be shown')
        N = np.sqrt(N)

        # SEABORN catplot
        dfm = pd.melt(fit_df, id_vars=[x,hue], value_vars=y_values)
        if DEBUG: print(dfm)
        fig = sns.catplot(data=dfm, x=x, y='value', col='variable',hue=hue)

        if scale != None:
            for _, ax in fig.axes_dict.items():
                for kind,axis,extends in ((scale[:3],'x',None),
                                          (scale[3:],'y',None)):
                    self._set_scale(plot_obj=ax,axis=axis,extends=extends,kind=kind)

        return(fig)

    def is_float(self, element) -> bool:
        try:
            float(element)
            return True
        except ValueError:
            return False
```

D.3. Electrodeposition control code

```
import pyvisa
import time
import numpy as np

'''
```

```
Using one of the following commands in live console:
    set_sweep('100E-6','100.1E-6')
    set_sweep('16E-6','16.01E-6')
    set_sweep('8E-6','8.001E-6')
    set_sweep('5.12E-6','5.121E-6')

Delay is calibrated as:
    .02=64
    .04=112s
    .05=138s
    .1=262s

The get_read function gathers the data
    and returns the values in a list.

The save_data function saves the gathered data
    to a file with a timestamp.
'''

output_path = './data/'

rm = pyvisa.ResourceManager()
keithley = rm.open_resource("GPIB::11::INSTR")
qq = lambda s : keithley.query(s)
ww = lambda s : keithley.write(s)

qq("*IDN?")
qq("*OPC?")

def set_sweep(start,end,kind='LIN',delay='0.04'):
    cmds = f''':SOUR:FUNC CURR
    :SENS:FUNC:ALL
    :SENS:VOLT:PROT 10
    :SOUR:DEL {delay}
    :SOUR:CURR:LEV 0
    :SOUR:CURR:START {start}
    :SOUR:CURR:STOP {end}
    :SOUR:CURR:MODE SWE
    :SOUR:SWE:RANG AUTO
    :SOUR:SWE:SPAC {kind}
    :SOUR:SWE:POIN 2500
    '''
    cmds = cmds.split('\n')
    for cmd in cmds:
        ww(cmd)

    ww(':SYST:LOCAL')

def get_read():
    try:
        ww(':TRIG:COUN 10')
        time.sleep(6)
        ww(':OUTP ON')
        data = qq(":READ?")
        time.sleep(10)
    finally:
        ww(':OUTP OFF')
        data = data.split(',')
    return(data)

def save_data(filename, data):
    timestamp = time.ctime().replace(':','').replace(' ','')
    np.save(output_path + filename + '_' + timestamp, data)
```

D.4. Electrodeposition volume code

```
import numpy as np
import pandas as pd
import glob
from scipy.integrate import simpson
```

```

Ag_mol = 107.8682 #u = g/mol
Ag_rho = 10.49*1e-12 #g/um^3
NA = 6.022e23 #atoms/mol
e_mol = 6.24e18 #atoms/C
F = NA/e_mol #C/mol

output_path = r'C:\Users\niels\OneDrive\OneDriveDocs\BME\Thesis\Software\Scripts\keithley/
    data/'

def get_theoretical(well_diameter,plated_time,
                    supplied_current=16e-6, echo=False):
    '''Args:
    well_diameter in um
    plated_time in s
    supplied_current in A
    '''

    well_area = ((well_diameter/2)**2)*np.pi #um2

    #available in solution
    Ag_solution_molar = .3 # mol/L
    Ag_solution_volume = 200e-6 #uL
    Ag_moles_available = Ag_solution_molar*Ag_solution_volume # mol

    #used during electrodeposition
    Ag_charge_depos = supplied_current*plated_time # C (moles of e = moles of Ag)
    Ag_moles_depos = Ag_charge_depos/F # C (moles of e = moles of Ag)
    Ag_grams_depos = Ag_moles_depos*Ag_mol #g

    #resulting volume and
    Ag_volume_depos = Ag_grams_depos/Ag_rho #um3
    Ag_height_depos = Ag_volume_depos/well_area #um

    if echo:
        print(f'Ag charge: {Ag_charge_depos:1.3e}')
        print(f'Ag mol (used): {Ag_moles_depos:1.3e} of (available) {Ag_moles_available:1.3e}
            ')
        print(f'Ag grams: {Ag_grams_depos:1.3e}g')
        print(f'Ag volume: {Ag_volume_depos:1.3e}um3')
        print(f'Ag height: {Ag_height_depos:1.3e}um')

    return(Ag_charge_depos,Ag_height_depos,
           Ag_volume_depos,Ag_moles_depos,Ag_moles_available,Ag_grams_depos)

def get_charge(chip_name):
    filename = glob.glob(output_path + chip_name + '*.npy')[0]
    V,I,R,t,S = ['Voltage [V]','Current [A]','Impedance [  ]','Time [s]','keithly-state']
    df=pd.DataFrame(np.load(filename), columns=[V,I,R,t,S])
    charge = simpson(y=df[I], x=df[t])

    return(charge)

if False:
    for wafer in range(2,5):
        for diameter in [30,50,100]:
            chip_name = f'w{wafer}_{diameter}um'
            charge = get_charge(chip_name)
            print(f'{charge*1000:1.3f}\t',end='')#{chip_name}:
        print('')

if False:
    print('\t\t',end='')
    for diameter in [30,50,100]:
        print(f'{diameter:<10}\t',end='')
    print('')
    for delay,duration in [ (.02, 65),
                            (.04,112),
                            (.05,138),
                            (.1 ,262), ]:
        charge,*_ = get_theoretical(1,duration)
```

```
74
75          print(f'{duration:d}\t',end='')
76          print(f'{charge*1000:1.3f}\t',end='')
77          for diameter in [20,30,50,100]:
78              charge,height,*_ = get_theoretical(diameter,duration)
79              print(f'{height:<10.3f}\t',end='')
80          print('')
81
82  if True:
83      wafers = [
84          #wafer with chips: (wafer, diameter, duration, deposit height)
85              [2,
86              (2,30,65,6538.01),
87              (2,50,65,1756.67),
88              (2,100,112,2225.39),
89              ],
90
91              [3,
92              (3,30,65,8679.65),
93              (3,50,65,3374.48),
94              (3,100,138,1952.06),
95              ],
96
97              [4,
98              (4,30,262,8670.04),
99              (4,50,262,10795.46),
100             (4,100,262,4625.22),
101             ],
102         ]
103
104     print('\t')
105     for diameter in [30,50,100]:
106         print(f"{diameter:<40}",end='')
107     print('')
108     for diameter in [30,50,100]:
109         print(f"{'height':<8}{'time':<8}{'th./ms.␣charge':<16}{'depos':<8}",end='')
110     print('')
111     for wafer,*chips in wafers:
112         for (wafer, diameter, duration, measured_height) in chips:
113             chip_name = f'w{wafer}_{diameter}um'
114
115             theoretical_charge,theoretical_height,*_ = get_theoretical(diameter,duration)
116
117             measured_height *= .001 #in um
118             measured_charge = get_charge(chip_name)
119
120             print(f'{measured_height:<8.3f}',end='')
121             print(f'{duration:<8d}',end='')
122             print(f'{theoretical_charge*1000:>8.3f}/{measured_charge*1000:<8.3f}',end='')
123             print(f'{measured_height/theoretical_height:<8.3f}',end='')
124         print('')
```

D.5. Electrodeposition profile plotting code

```
1  import os, re
2  import numpy as np
3  import pandas as pd
4  import matplotlib.pyplot as plt
5  import matplotlib as mpl
6  mpl.rcParams['figure.dpi']= 400
7  mpl.rcParams["figure.figsize"] = (6,4)
8
9  THRESHOLD = -1000
10 MIDDLE_POINT = 300
11 STD_SU8_HEIGHT = 11630 #nm
12
13 datafolder=r'C:\Users\niels\OneDrive\OneDriveDocs\BME\Thesis\Data\Dektak\Niels_dektak_FBatch\
       Fbatch\\'
14
15 def load_dektak(re_pattern, thicknesses=False, lateral=None, customLegend=None, colors=None,
```

```
    threshold=THRESHOLD):
    files = os.listdir(datafolder)
    checker = re.compile(re_pattern)
    filenames = [f for f in files if checker.match(f)]
    print(filenames)

    print(f'With␣"{re_pattern}"\nfound:␣{filenames}')

    ax = plt.axes()

    min_heights = []
    for filename in filenames:
        data = pd.read_csv(datafolder + filename, skiprows=19, encoding="ISO-8859-1", names =
            ['Lateral␣um','Raw␣Nanometer','-1','-2'])
        data = data[['Lateral␣um', 'Raw␣Nanometer']]

        if thicknesses:
            total_lateral = np.max(data['Lateral␣um'])-np.min(data['Lateral␣um'])
            total_indices = len(data)
            ind_per_lat = total_indices/total_lateral

            #shift first datapoint below threshold to middlepoint
            istart = np.where(np.array(data['Raw␣Nanometer'])<threshold)[0][0]
            ifinal = np.where(np.array(data['Raw␣Nanometer'])<threshold)[0][-1]
            min_height = data['Raw␣Nanometer'].iloc[istart:ifinal].min()
            min_heights.append(min_height)

            data['Lateral␣um'] = data['Lateral␣um'] - data['Lateral␣um'].iloc[istart]-
                MIDDLE_POINT
            if lateral != None:
                imiddle = istart+ifinal/2
                ilower = round(imiddle-lateral*ind_per_lat)
                iupper = round(imiddle+lateral*ind_per_lat)
                data = data.iloc[ilower:iupper]

            print(f'Minimum␣silver␣height␣=␣{STD_SU8_HEIGHT+min_height}')

        profile(data,ax)

    if thicknesses:
        print(f'Minimum␣height␣=␣{np.min(min_heights)}')

    if colors != None:
        for ii,color in enumerate(colors):
            ax.get_lines()[ii].set_color(color)

    if customLegend != None:
        ax.legend(customLegend)
    else:
        ax.legend(filenames)

    plt.show()

def profile(data, ax):
    data.plot(x='Lateral␣um', y='Raw␣Nanometer', ax = ax, linestyle='--')
    ax.set_ylabel('Profile␣nm')

if True:
    # w2_30um_16uA-262s
    load_dektak('w2_30.*', thicknesses=True, lateral=400, customLegend=[
        # 'Au',
        'Electroplated␣Ag',
    ],colors=['C1'])

    # w3_30um_16uA-65s
    load_dektak('w3_30.*', thicknesses=True, lateral=400, customLegend=[
        'Au',
        'Electroplated␣Ag',
    ])

    # w4_30um_EP (16uA-262s)
```

```
    load_dektak('w4_30.*', thicknesses=True, lateral=400, customLegend=[
        # 'Au',
        # 'Cleaned',
        'Chlorinated␣Ag/AgCl',
        'Electroplated␣Ag',
    ],colors=['C3','C1'],threshold=-500)

    # w2_50um_16uA-65s
    load_dektak('w2_50.*', thicknesses=True, lateral=400, customLegend=[
        'Au',
        'Electroplated␣Ag',
    ])

    # w3_50um_16uA-65s
    load_dektak('w3_50.*', thicknesses=True, lateral=400, customLegend=[
        'Au',
        'Electroplated␣Ag',
    ])

    # w4_50um_16uA-262s
    load_dektak('w4_50.*', thicknesses=True, lateral=400, customLegend=[
        'Au',
        'Electroplated␣Ag',
        'Chlorinated␣Ag/AgCl',
    ],colors=['C0','C1','C3'],threshold=-500)

    # w2_100um_16uA-112s
    load_dektak('w2_100.*', thicknesses=True, lateral=400, customLegend=[
        'Electroplated␣Ag',
        'Au',
        'Au␣again',
    ],colors=['C1','C0','C2'])

    # w3_100um_16uA-138s
    load_dektak('w3_100.*', thicknesses=True, lateral=400, customLegend=[
        'Au',
        # 'Cleaned',
        'Electroplated␣Ag',
        # 'Chlorinated Ag/AgCl',
    ])

    # w4_100um_16uA-262s
    load_dektak('w4_100.*', thicknesses=True, lateral=400, customLegend=[
        'Au',
        'Electroplated␣Ag',
        'Cleaned',
        'Chlorinated␣Ag/AgCl',
    ])
```

D.6. Track resistance distances

```
import numpy as np
import seaborn as sns
import matplotlib.pyplot as plt
sns.set_style('darkgrid', {'legend.frameon':False})
import matplotlib as mpl
mpl.rcParams['figure.dpi']= 500
plt.rcParams["figure.figsize"] = (3,2.4)

thickness = 200e-9
width = 100e-6
A = thickness*width

pauw_and_line_resistance = np.array([8.6,29.3])
resistances = np.array(
    [
        [0, 4.3, 7.0, 1.8, 3.6, 5.6, 8.8],
        [0, 0  , 4.3, 4.3, 2.3, 3.0, 6.2],
        [0, 0  , 0  , 6.9, 5.0, 3.0, 3.6],
        [0, 0  , 0  , 0  , 3.7, 5.6, 8.8],
```

```
        [0, 0  , 0  , 0  , 0  , 3.6, 6.9],
        [0, 0  , 0  , 0  , 0  , 0  , 5.0],
        [0, 0  , 0  , 0  , 0  , 0  , 0  ],
    ]
)

pauw_and_line_distance = np.array([6,21])*1e-3 #mm -> m
distances = np.array(
    [
        [0, 3.0, 5.0, 1.0, 2.5, 4.0, 6.5],
        [0, 0  , 3.0, 3.0, 1.5, 2.0, 4.5],
        [0, 0  , 0  , 5.0, 3.5, 2.0, 2.5],
        [0, 0  , 0  , 0  , 2.5, 4.0, 6.5],
        [0, 0  , 0  , 0  , 0  , 2.5, 5.0],
        [0, 0  , 0  , 0  , 0  , 0  , 3.5],
        [0, 0  , 0  , 0  , 0  , 0  , 0  ],
    ]
)*1e-3 #mm -> m

pauw_and_line_spec_resistances = np.divide(
    pauw_and_line_resistance*A,pauw_and_line_distance)
spec_resistances = np.divide(resistances*A,distances)

print(pauw_and_line_spec_resistances*1e9)
print(np.nansum(spec_resistances)/21*1e9)
sns.heatmap(spec_resistances*1e9, annot=True, fmt=".0f",
                xticklabels='1234567',
                yticklabels='1234567',)
plt.yticks(rotation=0)
plt.show()
```

E

Flowchart Microfabrication

Zero layer

1. COATING **Front side**

Use the coater station of the EVG120 system to coat the wafers with photoresist. The process consists of:

- a treatment with HMDS (hexamethyldisilazane) vapor, with nitrogen as a carrier gas
- spin coating of Shipley SPR3012 positive resist, dispensed by a pump
- a soft bake at 95 °C for 90 seconds
- an automatic edge bead removal with a solvent

Always check the relative humidity (48 ± 2 %) in the room before coating, and follow the instructions for this equipment.

Use program "1 - **Co - 3012 – noEBR**". There will be no edge bead removal.

2. ALIGNMENT AND EXPOSURE **Front side**

Processing will be performed on the ASML PAS5500/80 automatic wafer stepper.
Follow the operating instructions from the manual when using this machine.

Expose mask **COMURK**, with job **"litho /FWAM"**, layer ID=1 and E=150 mJ/cm^2.
This results in alignment markers for the stepper.

3. DEVELOPING **Front side**

Use the developer station of the EVG120 system to develop the wafers. The process consists of:

- a post-exposure bake at 115 °C for 90 seconds
- developing with Shipley MF322 with a single puddle process
- a hard bake at 100 °C for 90 seconds

Always follow the instructions for this equipment.

Use program "1-**Dev - SP**".

4. INSPECTION **Front side**

Visually inspect the wafers through a microscope, and check the development. No resist residues are allowed.

5. PLASMA ETCHING OF ALIGNMENT MARKS **Front side**

Use the Trikon Ωmega 201 plasma etcher.
It is **not** allowed to change the process conditions and etch times from the etch recipe!

Use sequence **URK_NPD** (with a platen temperature of **20 °C**) to etch the structures 120 nm deep into the Si.

Process conditions from chamber recipe URK_ETCH:						
Step	Gasses & flows	Pressure	Platen RF	ICP RF	Platen temp.	Etch time
1. breakthrough	CF_4/O_2 = 40/20 sccm	5 mTorr	60 W	500 W	20 °C	0'10"
2. bulk etch	Cl_2/HBr = 80/40 sccm	60 mTorr	20 W	500 W	20 °C	0'40"

6. LAYER STRIPPING: Photoresist **Front side**

Strip resist Use the Tepla Plasma 300 system to remove the photoresist in an oxygen plasma.
Use **program 1**: 1000 watts power and automatic endpoint detection + 2 min. overetching.

7. CLEANING: HNO_3 99% and 69.5% **Both sides**

Clean	10 minutes in fuming nitric acid at ambient temperature. This will dissolve organic materials. Use wet bench "HNO_3 99% (Si)" and the carrier with the red dot.
Rinse	Rinse in the Quick Dump Rinser with the standard program until the resistivity is 5 MΩ.
Clean	10 minutes in concentrated nitric acid at 110 °C. This will dissolve metal particles. Use wet bench "HNO_3 69,5% 110C (Si)" and the carrier with the red dot.
Rinse	Rinse in the Quick Dump Rinser with the standard program until the resistivity is 5 MΩ.
Dry	Use the Semitool "rinser/dryer" with the standard program, and the white carrier with a red dot.

Gold layer

8. COATING **Front side**

Use the coater station of the EVG120 system to coat the wafers with photoresist. The process consists of:
- a treatment with HMDS (hexamethyldisilazane) vapor, with nitrogen as a carrier gas
- spin coating of AZ Nlof2000 negative resist, dispensed by a pump
- a soft bake at 95 °C for 90 seconds

Always check the relative humidity (48 ± 2 %) in the room before coating, and follow the instructions for this equipment.

Use program "1 - **Co – Nlof – 3,5um**".

9. ALIGNMENT AND EXPOSURE **Front side**

Use the EVG420 Contact aligner
Using the contaminated chuck:

Expose:	**IC**
Expose mask**:**	**<Mask number (mask A)>** (box <Mask box>)
Energy:	E=55mJ

10. X-LINK BAKE **Front side**

Use the developer station of the EVG120 system to cross link the exposed AZ Nlof 2000 resist. The process consists of:
- a cross link bake 115 °C for 90 seconds

Always follow the instructions for this equipment.

Use program "**Only – X-link bake**".

11. DEVELOPING **Front side**

Use the developer station of the EVG120 system to develop the wafers. The process consists of:
- developing with Shipley MF322 with a single puddle process
- a hard bake at 100 °C for 90 seconds

Always follow the instructions for this equipment.

Use program "**1 - Dev – lift-off**".

12. Measurement resist thickness DEKTAK **Front side**

Target thickness 3.0 – 3.5 micron on bondpads.

13. INSPECTION **Front side**

Visually inspect the wafers through a microscope. No resist residues are allowed on bond pads.

14. STRIPPING: Photoresist residues. WARNING: USE COLD TEPLA, T< 25C. **Front side**

Strip resist Use the Tepla Plasma 300 system for an oxygen plasma flash.
Follow the instructions specified for the Tepla stripper, and use the quartz carrier.
Tepla needs to be at room temp before starting the program.

Use progam **no 2**: 1 minute at 600 watts. This will not remove a photoresist masking layer.

15. METALLIZATION: Evaporate 20nm chromium and 200nm gold **Front side**

Use the CHA Solution Std. metal evaporation system in the CR10000 to deposit a 20 nm chromium and 200 nm gold layer.

Use **program nr. 26: Cr, Au** and follow the instructions in the CHA manual.
Important: Use the Au dome and shutters for this process, they are found in the grey cupboard behind the CHA system.
Visual inspection: the metal layer must look shiny.

16. ADHESION TEST **Front side**

Use standard scotch tape to test the adhesion of the gold layer on the wafers.
Visual inspection: the gold layer is not allowed to peel off of the wafers and stick to the scotch tape.

17. LIFT OFF: 20nm chromium and 200nm gold **Front side**

Follow the procedure as described in the litho instructions manual:
- heat up a beaker with DI – water to 80 °C
  put the heated DI-water in the ultra sonic bath and set the temperature to 80 °C
- heat up a beaker with NMP to 70 °C
  pour the heated NMP in a rectangular beaker that fits in the top lid opening
- put the process wafer in the heated NMP using a single wafer holder or carrier
- switch on the ultra sonic bath with a time of 15 min
- use cotton bud to facilitate the lift-off
- rinse the wafer with DI-water in a beaker for 5 minutes
- dry the wafer on the single wafer dryer

REMARK: For safety reasons 70 °C is the max. working temp. of the NMP solvent. The flashpoint is ± 85°C!

18. INSPECTION **Front side**

Visually inspect the wafers through a microscope, and check the lift-off. No Cr/Au residues are allowed.

19. POST LIFT OFF CLEANING **Front side**

Use the following procedure:
- Heat up a beaker with DI water to 80 °C.
- Pour the heated-up DI water in the ultrasonic bath and set the temperature to 80 °C.
- Heat up a rectangular beaker with DI water to 70 °C in a "**au bain Marie**".
- Place the heated-up rectangular beaker with DI water in the ultrasonic bath.
- Place a process wafer in the heated-up DI water, using a single wafer holder or carrier.
- Set the time on the ultrasonic bath to 5 minutes, and switch it on.
- When done, rinse the wafer with fresh DI water for 5 minutes.
- Dry the wafer on the single wafer dryer using **the chuck for Cu contaminated wafers.**

20. CLEANING: HNO_3 99% in SAL **Both sides**

Do an additional cleaning step inside the SAL:
- Prepare a beaker of DI water for rinsing at room temperature
- Prepare a bath of HNO_3 99% at room temperature
- Use a plastic wafer carrier to transport the wafers
- Put the wafers for 10 min in the HNO_3 99% and for a 5 min rinse in the DI beaker.
- Dry the wafer on the single wafer dryer using **the chuck for Cu contaminated wafers.**

21. INSPECTION **Front side**

Visually inspect the wafers through a microscope, and check if the wafers are clean. No particles are allowed.

SU8 layer

22. MANUAL COATING PREPARATION — Front side

Put on an extra pair of gloves and change whenever SU8 contact.

Prepare the SU8-2015 for use by:
- Pouring a small amount into a small canister and closing the lid
- Let it reach room temperature

Prepare the hotplate for use:
- Place dummy wafer
- Set temperature to 100°C
- Let it reach this temperature before spinning
- Set a timer for 5 min in preparation for soft-bake

Prepare the spinning chamber
- **Contaminated chuck and aligner** onto chamber rod
- Aluminum sheet into plastic holder into chamber

Prepare cleaning materials:
- Acetone spray bottle (! Be carefull to not put the Acetone next to the hotplate !)
- IPA spray bottle
- Some absorbing wipes
- 4-6 Q-tips

Input the desired spinning program (note: this may change depending on the required thickness)

Select “niels_SU8_10um”:

Spreading spin settings:	500 rpm	(with 100 rpm/s)	for 5 s
Thickness sping settings:	5000 rpm	(with 300 rpm/s)	for 30 s

23. POURING AND SPINNING SU8 — Front side

First check spinner functioning:
- Transfer the wafer onto the chuck with contaminated tweezer and the chuck aligner.
- Turn on the vacuum line
- Check wafer-chuck fixation
- Close lid and check wafer rotation
- Wait till finished and open the lid

Spinning SU8-2015
- Turn on the vacuum line again
- Check wafer-chuck fixation
- Open the SU8 cannister
- Pour the SU8 onto the middle of the wafer from a low height until half of the wafer diameter is covered
- Close the lid and check wafer rotation
- Use a wipe to clean the edge of the cannister (if necessary) and close the lid.
- Wait till spinning is finished

24. BACKSIDE CLEANING — Back side

In order to make sure the backside of the wafer does not contain traces of SU8:
- Pick the wafer from the chuck with one hand and flip backside up
- Spray a Q-tip with Acetone on a tissue
- Carefully use the Q-tip to wipe SU8 off the backside of the wafer
- Repeat this using multiple Q-tips until SU8 is visually absent

25. PRE-EXPOSURE SOFT BAKING — Front side

Baking step before exposure is done at:

100°C for 5 min

After backside cleaning with the process wafer in one hand:
- Grab contaminated tweezer in other hand
- Flip process wafer with the frontside up
- Slowly place the process wafer onto the dummy wafer on the hotplate (! Don’t touch the very hot hotplate !)
- Controll the skidding of the wafer with the backside of the contaminated tweezer
- Once the wafer lays still, start the timer for 5 min.
- When timer is done, inspect SU8 layer: it should not be sticky, else wait longer.

- Put it to the side and let it cool down
- Then place wafer back in wafer box

26. CLEANING OF MANUAL COATER

When spinning is done and the wafers are coated, clean the manual coater chamber and components thoroughly:

- Remove the chuck with a tissue and rub it with Acetone till clean
- Remove the plastic holder, fold the Aluminum foil and dispose in the designated bin
- Spray the chamber with Acetone, do not spray into the vacuum lines
- Wipe the chamber and spray acetone till clean
- Clean the metal part of the lid with Acetone covered wipes
- Clean the glass part of the lid with IPA covered wipes
- Remove 2nd pair of gloves

27. ALIGNMENT AND EXPOSURE **Front side**

Use the EVG420 Contact aligner

Expose: **IC**
Expose mask**:** **<Mask number (mask B)>** (box <Mask box>)
Energy: E=140mJ

Note: Check the calibrated dosage before exposure time calculation
Note: Make sure to book a reservation for the system

Use box: **XXX** and mask: **XXX** for microwell and contact-pad openings
Expose the SU8-soft-baked wafer:

- Use the Soft-Contact setting
- Put mask into the mask holder (chrome side down), clamp mechanically and turn on its vacuum
- Place mask holder in machine, activate mask holder clamping and forcefully test rigidity
- Align the Mask's alignment markers
- Use the contaminated contact aligner chuck
- Place wafer onto wafer slide, turn on vacuum and test wafer attachment
- Align the wafer's alignment markers to the mask's alignment markers
- Set exposure time: (! Check relative dose, since exposed pattern is on gold !)

  Exposure_time =
  Required_dose(thickness dependent) / Dose_per_second(calibrated value next to machine) * Relative_dose

  10um SU8 → 140 mJ/cm2
  Relative dose on Au: 1.5x – 2x
  Example: "Exposure_time = 140[mJ/cm2]/14[mJ/cm2-s]*1.5 = 15 sec exposure."

- Alignment check.
- Expose
- Open wafer slide and then turn off vacuum
- Remove the wafer, place back in box
- Open mask holder clamp, remove mask holder, turn off mask holder vacuum and open mechanical clamp
- Remove mask and place back in box

28. POST-EXPOSURE BAKING **Front side**

Baking step after exposure is also done at:
100°C for 5 min

Do another bake step before development:

- Grab the process wafer with the contaminated tweezer
- Transfer the process wafer to hand
- Slowly place the process wafer onto the dummy wafer on the hotplate (! Don't touch the very hot hotplate !)
- Controll the skidding of the wafer with the backside of the contaminated tweezer
- Once the wafer lays still, start the timer for 5 min.
- When timer is done, put it to the side and let it cool down
- Then place wafer back in wafer box or move it directly to the development area

29. DEVELOPING PREPARATION **Front side**

Gather following materials

- Q-tips
- SU8 developer (PGMEA)
- IPA spray bottle
- DI-water spray bottle

- Wide low beaker (bigger than wafer)
- Narrow high beaker
- Set a timer for 3 min for development

Make sure to wear an extra pair of gloves at all times and replace these when necessary.
Disposal of the solutions: PGMEA, IPA → organic container

30. DEVELOPING **Front side**

For development of the non-exposed SU8 we can use the puddle method:

- Place the narrow high beaker upside down inside the wide low beaker
- Place the process wafer on the bottom of the narrow beaker
- Now the PGMEA developer can be applied on top
- Cover the wafer, and start the timer for 3 min directly
- Tilt the wafer and replenish the PGMEA every minute
- After 3 minutes tilt the wafer and rinse with IPA and then with DI water
- Visually inspect the wafer to determine the pattern quality
- Spin dry the wafer or hold it vertically on a wipe use the N2-gun to remove remaining droplets
- Place the wafer back in the box or move back to the hotplate for hard bake
- Make sure the organics are correctly disposed

31. HARD BAKING **Front side**

The hard bake should be conducted at and even high temperature:
150°C for 10 min

Curing the wafer with this hard bake is done as before:

- Grab the process wafer with the contaminated tweezer
- Transfer the process wafer to hand
- Slowly place the process wafer onto the dummy wafer on the hotplate (! Don't touch the very hot hotplate !)
- Controll the skidding of the wafer with the backside of the contaminated tweezer
- Once the wafer lays still, start the timer for 10 min.
- When timer is done, put it to the side and let it cool down
- Then place wafer back in wafer box

Final inspection

32. MEASUREMENT **Front side**

Inspect the wafer surface using the KEYENCE microscope with the **contaminated chuck** and determine the profile on multiple areas on the wafer.